UNIVERSITAT DE BARCELONA

Highly active and efficient metal-decorated silicon-based nanostructured photoelectrodes for water splitting solar cells

Tingting Han

PhD thesis dissertation

Highly active and efficient metal-decorated silicon-based nanostructured photoelectrodes for water splitting solar cells

Author: Ms. Tingting Han

Director: Dr. Mario Lanza

UNIVERSITAT DE BARCELONA

Highly active and efficient metal-decorated silicon-based nanostructured photoelectrodes for water splitting solar cells

Memoria presentada para optar al grado de doctor por la

Universidad de Barcelona

Programa de doctorado en Nanociencias

Tingting Han 韩婷婷

Author: Ms. Tingting Han

Director: Dr. Mario Lanza

Tutor: Dr. Albert Cirera

UNIVERSITAT DE BARCELONA

To my family,

Acknowledgements

First of all, I would like to thank my PhD director Prof. Mario Lanza for working with me in the lab, supervising my work and helping me improve myself. He taught me lots of knowledge and shared his research experience to me, including lots of useful information that could not be obtained from books. And he spent time with me in the lab doing experiments and gave me suggestions when I have doubts about the research. Also in the life, when I was lack of confidence and felt confused about the life, he also provided his abundant views to guide me. With the great help of Prof. Lanza, I feel that I have obtained big progress on both research and communication skills during my PhD study.

I also would like to appreciate all the group members in Prof. Lanza's group (lanzalab.com) for their kind help on research and life, especially Yuanyuan Shi, Fei Hui and Yanfeng Ji. Since they joined our research group earlier than me, they shared their research experience to help me adjust the graduate life. Importantly, they helped me understand and use different machines in the lab, thus I can continue to perform my research projects. Because Yuanyuan is the only student in our group working on water splitting project, I sincerely thank for her guidance on my research. I love Prof. Mario Lanza research group, which provide us an enjoyable working environment to work together happily. All the technicians from the Institute of Functional Nano and Soft Materials (FUNSOM) of Soochow University deserve my acknowledgment for their technical advice and help on using the equipment in the institute, as well as the administration staff for all their help.

Besides, I also send special thanks to Dr. Salvatore Lombardo from Institute of Microelectronics and Microsystems, National Research Council (CNR-IMM) of Italy, who gave me the opportunity to study one year in his group, and also to Dr. Stefania Privitera, who worked with me in the lab and gave me suggestions when I felt confused. They helped me learn more about photoelectrochemical (PEC) water splitting project. I also would like to thank Prof. Antoni Llobet and Dr. Carolina Gimbert-Suriñach from Institute of Chemical Research of Catalonia (ICIQ) in Spain, who made me have a deep understand on PEC water oxidation. I also send special thanks to Mª José Gutiérrez Prior as the secretary in Prof. Llobet group for her great help during my stay in ICIQ. All the group members and technicians from CNR-IMM and ICIQ deserve my acknowledgment for their technical advice and help on using the equipment in the institutes, especially Marta Ventosa whom I work with on water oxidation projects, Andrea Scuto and Luca Valenti who gave me great help in my Italian life. During my visiting time, we worked together and had abundant discussions, which benefited me a lot and laid a solid foundation on my future research. I also would like to thank all the coauthors of my publications,

especially Dr. Yuanyuan Shi, who helped me initially with water splitting devices and gave me many suggestions on the research, and those from CNR-IMM and ICIQ.

I also acknowledge all the institutions that, with their funding support, made this research project possible, especially to the fellowship of Programme for Training and Research in Italian Laboratories from International Centre for Theoretical Physics (ICTP), the Postgraduate International Exchange Scholarship from Soochow University, the Young 1000 Program, and the National Science Foundation of China. I specially appreciate the support received from FUNSOM at Soochow University, for allowing me using the clean room and all the characterization techniques as much as I needed for free.

At this point, I also send my special appreciates to all the professors who are my tutors and coordinators of the PhD program in nanosciences at University of Barcelona, especially to my tutor (Prof. Albert Cirera) and to the coordinator of the PhD program in nanosciences (Prof. Juan Marcos Fernandez), as well as all the professional staff from academic affairs, who helped me to compete all the administrative processes.

Finally, I also would like to show my endless gratitude to my family and friends, thank you all very much for your concern, encouragement and support all the time.

To all of you, thank you.

Index

Abstract ..... p. 1

Abstract in official language ..... p. 3

Chapter 1: General introduction ..... p. 5

1.1. Global environmental issues ..... p. 5
1.2. Photoelectrochemical water splitting solar cells ..... p. 8
1.3. Selection of seiconductors as photoelectrodes ..... p. 11
1.4. Metal or metal oxide films based coatings as catalysts for PEC water splitting ..... p. 14
1.5. Metal nanoparticles based coatings as catalysts for PEC water splitting ..... p. 20
1.6. Effect of electrolytes ..... p. 25
1.7. Materials characterization techniques ..... p. 28
1.7.1. Scanning electron microscopy ..... p. 28
1.7.2. Atomic force microscopy ..... p. 32
1.7.3. Transmission electron microscopy ..... p. 35
1.7.4. X-ray photoelectron spectroscopy ..... p. 40
1.8. Main contribution of this thesis ..... p. 42
1.8.1. Objectives of the thesis ..... p. 42
1.8.2. Key findings ..... p. 43
1.8.3. Thesis outline ..... p. 44
1.8.4. List of publications ..... p. 44

Chapter 2: Ageing mechanisms of Ni-based n-type Si photoanodes for photoelectrochemical water splitting ..... p. 47

2.1. Introduction ..... p. 47
2.2. Experimental section ..... p. 48
2.2.1. Fabrication of electrodes..... p. 48
2.2.2. Electrochemical characterization ..... p. 49
2.2.3. Characterization of materials ..... p. 51
2.3. Results and discussion ..... p. 52
2.3.1. PEC performance of Ni/SiO_X/n-Si/Ti photoanodes ..... p. 52
2.3.2. Ageing mechanisms of 5 nm and 10 nm Ni/SiO_X/n-Si/Ti photoanodes .. p. 55
2.3.3. Ageing mechanisms of 2 nm Ni/SiO_X/n-Si/Ti photoanodes ..... p. 60
2.4. Conclusions ..... p. 66

Chapter 3: Effect of different alkaline electrolytes on photoelectrochemical performance ..... p. 69

3.1. Introduction..... p. 69
3.2. Experimental section ..... p. 71
3.2.1. Fabrication of electrodes..... p. 71
3.2.2. Electrochemical characterization ..... p. 72
3.2.3. Characterization of materials ..... p. 73
3.3. Results and discussion ..... p. 73
3.4. Conclusions ..... p. 80

Chapter 4: Metal nanoparticles coated SiC/Si photocathodes for photoelectrochmical water splitting..... p. 81

4.1. Introduction ..... p. 81
4.2. Experimental section ..... p. 83
4.2.1. Fabrication of electrodes..... p. 83
4.2.2. Electrochemical characterization ..... p. 85
4.2.3. Characterization of materials ..... p. 86
4.3. Results and discussion ..... p. 86
4.4. Conclusions ..... p. 96

Chapter 5: Conclusions and perspectives ..... p. 97

References ..... p. 101

Appendix ..... p. 121

A: Scientific curriculum vitae ..... p. 121

B: Summary in official language ..... p. 127

C: List of acronyms ..... p. 131

Abstract

With the burning of large amounts of traditional fossil fuels, global environmental pollution is getting worse and worse, and energy crisis is becoming more serious for meeting human's life demand. In order to solve these problems, it's imperative to find renewable and clean energy sources. Although sunlight is one of the most abundant renewable energy on earth, it's difficult to collect and store.

As a non-polluting energy, hydrogen is a highly promising candidate to replace fossil fuels. Sunlight can be used to split water into hydrogen and oxygen, producing chemical energy stored in hydrogen bonds. This easy way of producing clean fuels (hydrogen) has attracted the attention of both industry and academy. Photoelectrochemical (PEC) water splitting is one of the most promising methods to produce hydrogen by utilizing solar energy, due to the simple structure, low fabrication cost and good performance of the prepared cells. In these cells, a semiconductor photoelectrode is immersed in an electrolyte, and when illuminated, hydrogen and/or oxygen can be generated on its surface by electrolysis.

To obtain better performance for PEC water splitting devices, it's extremely significant to select proper semiconductors for absorbing light, catalysts for enhancing the PEC performance and electrolytes containing various ions. Silicon has garnered very much interest as semiconductor photoelectrodes due to its low cost and proper band gap (1.1 eV). However, the electrolyte can oxidize and/or corrode the surface of the photoelectrodes, resulting in a reduction of its performance. Metal catalysts are often used to avoid the degradation of silicon photoelectrodes, and to enhance their activity in the electrolyte. However, the degree of protection can be reduced after some periods of time, and consequently the lifetime of the semiconductor photoelectrodes is still the main bottleneck of this PEC water splitting technology. Besides, tuning the pH of the electrolytes or the chemical composition of the electrolytes including special species could improve the activity and stability of the cells.

In this PhD thesis I present a deep study about the ageing mechanisms of Ni layers with different thicknesses as protective and catalytic coatings on n-type Si photoanodes for PEC water splitting in strong alkaline condition. We also developed an advanced electrolyte (a mixture of potassium hydroxide (KOH) and lithium hydroxide (LiOH),

pH 12.5) that shows good activity and stability for metal-based silicon photoelectrodes. Furthermore, we also designed, fabricated and tested n-3C-SiC/p-Si photocathodes covered with noble metal nanoparticles for PEC water splitting in a strong alkaline electrolyte, and observed an enhancement of PEC performance thanks to the catalytic and plasmonic resonance effects of the nanoparticles introduced.

Abstract in official language

Con la quema de grandes cantidades de combustibles fósiles tradicionales para satisfacer la demanda energética humana, la contaminación ambiental global está empeorando cada vez más, y la crisis energética se está volviendo más grave. Para resolver estos problemas, es imperativo encontrar fuentes de energía renovables y limpias.

La luz solar es una de las energías renovables más abundantes en la tierra, y puede convertirse en energía química almacenada en enlaces de hidrógeno. La división de agua mediante fotoelectroquímica (PEC, por sus siglas en inglés) utilizando luz solar es uno de los métodos más prometedores para producir combustible hidrógeno de forma limpia, debido a la estructura simple, el bajo costo de fabricación y el buen rendimiento. En las células fotoelectroquímicas, un fotoelectrodo semiconductor se sumerge en un electrolito y, cuando se ilumina, se puede generar hidrógeno y/u oxígeno en su superficie mediante electrólisis.

Para obtener un mejor rendimiento, es extremadamente importante seleccionar semiconductores adecuados para absorber la luz, catalizadores para mejorar el rendimiento, y electrolitos que contienen varios iones. El silicio ha suscitado mucho interés debido a su bajo costo y a sus propiedades eléctricas (banda prohibida de 1.1 eV). Sin embargo, debido a su inestabilidad en el electrolito, los catalizadores metálicos a menudo se usan para evitar la degradación de los fotoelectrodos de silicio y para mejorar su actividad en el electrolito. Dado que el grado de protección se puede reducir después de algunos períodos de tiempo, la vida útil de los fotoelectrodos de semiconductores sigue siendo el principal cuello de botella de esta tecnología de división de agua PEC. Además, ajustar el pH o la composición química de los electrolitos, incluidas las especies especiales, podría mejorar la actividad y la estabilidad de las células.

En esta tesis, he estudiado el uso de niquel como capa protectora y catalizadora sobre fotoelectrodos de silicio, y hemos analizados su envejecimiento bajo condiciones de funcionamiento reales. También he desarrollado un electrolito avanzado (una mezcla de hidróxido de potasio [KOH] e hidróxido de litio (LiOH), pH 12.5) que muestra una buena actividad y estabilidad para los fotoelectrodos de silicio a base de metal. Además,

también diseñamos, fabricamos y testeamos fotocatodos n-3C-SiC/p-Si cubiertos con nanopartículas de metales nobles para la división de agua PEC en KOH, y observamos una mejora en el rendimiento de PEC debido a los efectos de resonancia catalítica y plasmónica de las nanopartículas introducidas.

Chapter 1:
General introduction

1.1. Global environmental issues

With the rapid development of economy and the exponential growth of population, global environmental problems have become the most troubling issues that human are facing and concerning nowadays. Specially, natural resource depletion, air pollution and global warming have been attracting most attention. According to the statistics from International Energy Agency (IEA), in 2018, the global energy consumption increased by 2.3% compared to the usage in 2017, almost twice the average growth rate since 2010 (Figure 1.1).[1] Although renewables experienced an increase with double-digit pace, they still can't meet the growth in demand for global electricity, thus fossil fuels have fulfilled nearly 70% of the growth for the second consecutive year. As a result, the abundant consumption of fossil fuels and their limited quantities on the world are gradually leading to the depletion of natural resources. Based on the Statistical Review of World Energy 2019 elaborated by British Petroleum (BP) company, humanity will run out of coal in ~132 years, and both of the oil and natural gas will run out in ~50 years.[2]

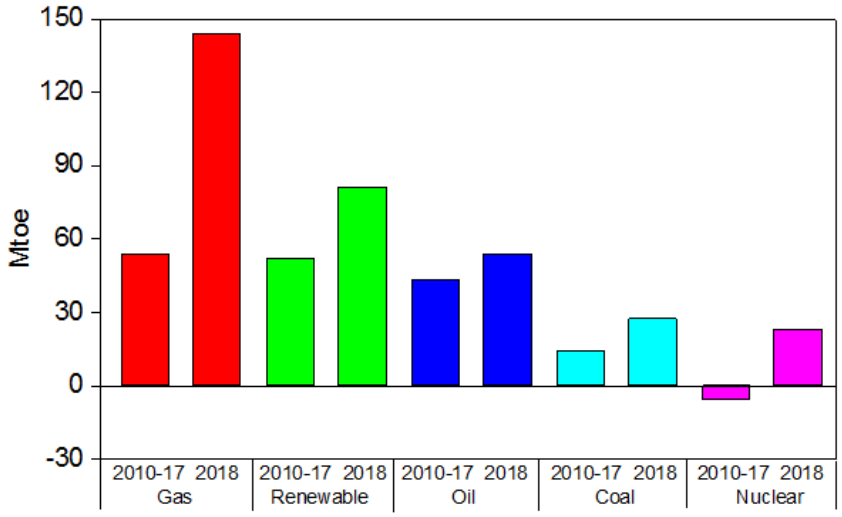

Figure 1.1 Average annual global primary energy demand growth by fuel from 2010 to 2018.[1]

At the same time, the burning of oil, coal and natural gas emits a large amount of carbon dioxide (CO_2) and other harmful gases (e.g. SO_2, NO, NO_2), which severely affect our living environment.[1,3] As one of the most important greenhouse gases, the concentration of CO_2 in the atmosphere has increased by more than a third since the Industrial Revolution (Figure 1.2a),[4] and the global surface temperature has risen about 1°C due to the human activities (Figure 1.2b).[5] Therefore, global warming has been an indisputable fact of our current livelihoods, which could induce sea-level rise, regional changes in precipitation and desert expansion, among others.

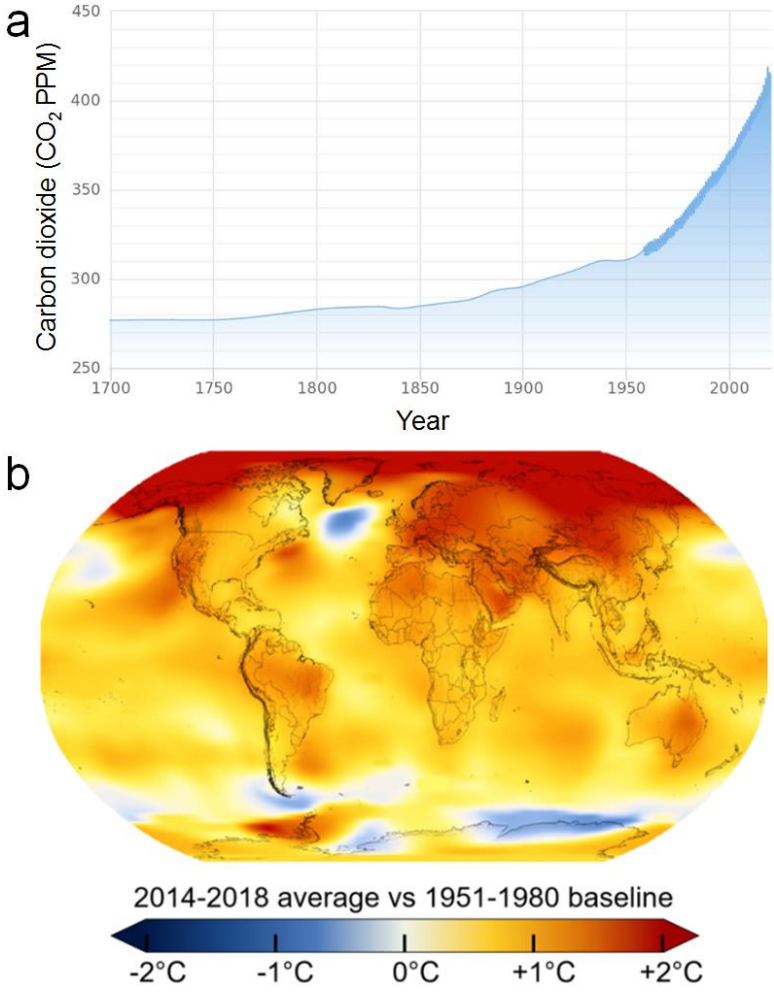

Figure 1.2 (a) Atmospheric CO_2 levels from 1700 to 2019 recorded by the 2° institute.[4] (b) Temperature change in the last 50 years. Average global temperatures from 2014 to 2018 compared to a baseline average from 1951 to 1980.[5]

Moreover, the harmful emission of gases from the combustion of fossil fuels has a significant impact on air pollution, which can cause great harm to the health of human.

According to World Health Organization (WHO), it is estimated that 9 out of 10 people are breathing air containing high level of pollutants, and every year there are about 4.2 million deaths worldwide due to exposing to ambient air pollution.[6-7]

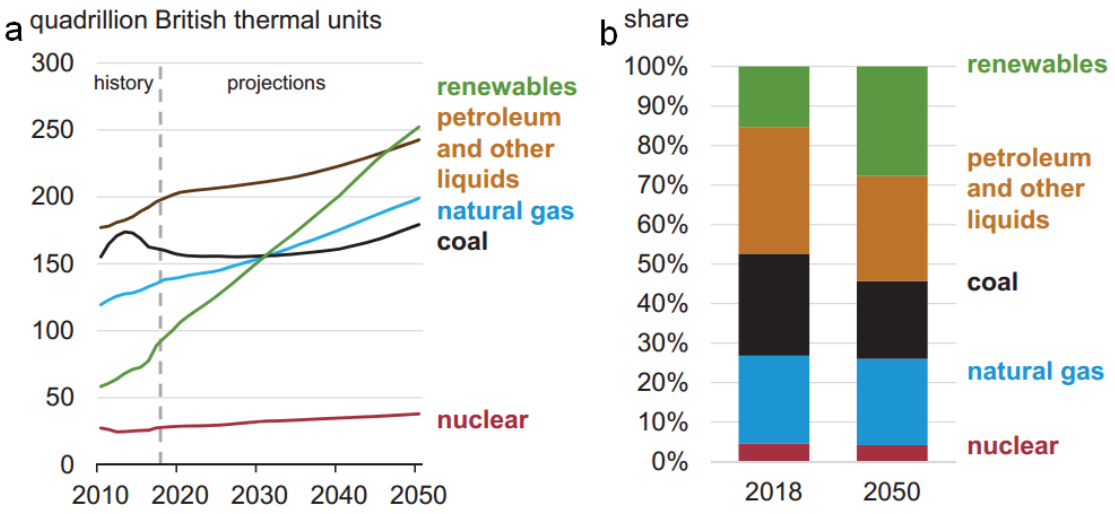

Figure 1.3 Global primary energy consumption history versus projection by energy source calculated by (a) quantity and (b) share. 1 quadrillion British thermal units = 10^{15} Btu = 1.055×10^{15} kJ.[8]

To reduce environmental pollution and global warming, it's essential to exploit and use clean and renewable resources to sustain human life. The U.S. Energy Information Administration (Figure 1.3) predicted that renewable energy will become the leading source of primary energy consumption to meet people's demand by 2050.[8] Solar energy, radiation from the sun, could be a promising candidate to replace fossil fuels as primary energy resource due to its inexhaustible supply and non-polluting property. Although the Earth can receive abundant solar energy, approximately 1.2×10^{17} J/s,[9] some shortcomings, such as the dispersion, location dependence and storage difficulty, are seriously hindering its utilization. Therefore, in order to fulfill the global energy demand by utilizing solar energy, the collection, storage and transportation problems have to be overcome. Probably the most attractive and desirable approach is to use solar energy to produce chemical fuels, as they can be stored and transported.[10-11] Among them, hydrogen (H_2) is one of the most promising candidates because it can be produced easily by splitting molecules of water, and its combustion in oxygen (O_2) atmosphere produces no pollution.

1.2. Photoelectrochemical water splitting solar cells

Since Fujishima and Honda for the first time built solar-driven electrolysis with a n-type TiO_2 electrode in 1972 (Figure 1.4),[12] PEC water splitting process has played (and will play) a key role in generating clean H_2 fuel by absorbing inexhaustible solar energy, which has attracted great interest among numerous scientists. A basic PEC water splitting solar cell consists of electrodes (at least one photoelectrode as sunlight absorbers capturing solar energy to facilitate water splitting), aqueous electrolyte and conductive wires for electron movement. The overall water splitting process (Equation 1.1) includes two half reactions, namely, oxygen evolution reaction (OER, Equation 1.2) and hydrogen evolution reaction (HER, Equation 1.3). Semiconductors, as the main photoactive materials, are used to construct photoelectrodes, including n-type semiconductor photoanode and p-type semiconductor photocathode. When the PEC water splitting system is illuminated under sunlight, the semiconductor photoelectrode can be able to absorb the photons whose energy is equal to or higher than its band gap energy. Then the electrons are excited from the valence band (VB) to the unoccupied conduction band (CB), resulting in excited electrons and holes produced in the CB and VB, respectively (Equation 1.4). For OER, the VB potential of the illuminated photoanode is required to be more positive than the thermodynamic water oxidation potential, which is 1.23 V versus reversible hydrogen electrode (RHE). Whereas the CB potential of the illuminated photocathode is required to be more negative than the thermodynamic water reduction potential (0 V vs. RHE) to permit water reduction reaction (HER). It is worth mentioning that extra overpotential should be provided in order to overcome the energy losses related to the resistance of the electrodes and electrical connections, voltage losses at the contacts and electron-hole recombination.[14]

Overall water splitting: $2\ H_2O \rightarrow 2\ H_2\uparrow + O_2\uparrow$ ($\Delta E = 1.23$ V) Equation 1.1

OER: $2\ H_2O + 4\ h^+ \rightarrow O_2\uparrow + 4\ H^+$ ($E_{ox} = -1.23$ V vs. RHE) Equation 1.2

HER: $4\ H^+ + 4\ e^- \rightarrow 2\ H_2\uparrow$ ($E_{red} = 0$ V vs. RHE) Equation 1.3

Semiconductor + $h\upsilon \rightarrow e^- + h^+$ Equation 1.4

where h, υ, e^- and h^+ are the Planck's constant, light frequency, photogenerated-electrons and photogenerated-holes, respectively.

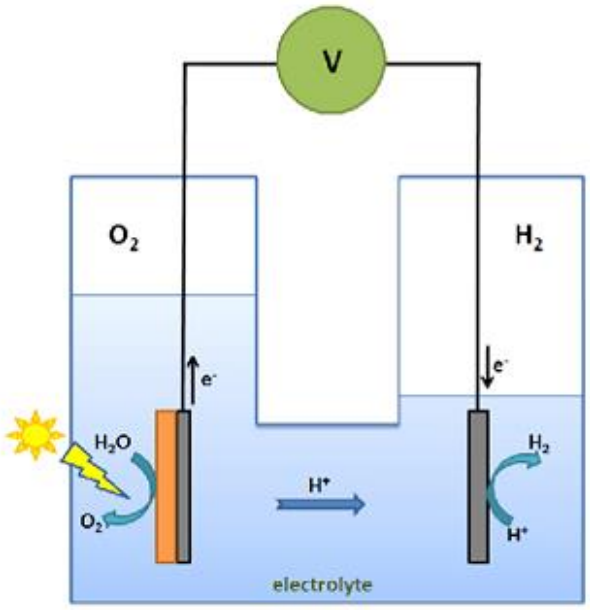

Figure 1.4 Schematic of a PEC solar cell for water splitting.[12-13]

So far, four types of PEC water splitting device configurations (Figure 1.5) have been mainly reported. The first type (Figure 1.5a), which is the simplest configuration possible for PEC water splitting, contains one single semiconductor photoanode or photocathode as light absorber to carry out water oxidation or reduction. However, the drawback is that generation of water oxidation or reduction requires the application of a large external bias (between the photoelectrode and a counter electrode immersed in the electrolyte) to induce the separation of electrons and holes. The second type (Figure 1.5b) consists of a heterojunction photoelectrode formed by combining two or more semiconductors for PEC water splitting, which enables to harvest more light and obtain better charge carrier separation.[15] The third and fourth types (Figure 1.5c and 1.5d) introduce a PEC tandem configuration by coupling an n-type semiconductor photoanode and a p-type semiconductor photocathode. By absorbing light, water oxidation and water reduction can be driven at the surface of photoanode and photocathode, respectively, without the aid of external bias. The difference between these two configurations is the connection method. For the wired configuration (third type, Figure 1.5c), two photoelectrodes are connected by one conductive metal wire, while a transparent conductive substrate as the electron-hole recombination layer is used for the wireless configuration (fourth type, Figure 1.5d). However, in both cases, to make sure that the tandem cells work by light absorption, one essential requirement is that the minimum CB of the photoanode should be more negative than the maximum

VB of the photocathode.[16] In addition, although the PEC tandem cells present obvious superiorities on agile materials selection, increased photovoltage and needless external voltage, the photoanodes and photocathodes have to generate similar current densities under the condition of light illumination.[16] Nevertheless, the PEC tandem cell shown in Figure 1.5c is the most promising approach to produce clean and renewable H_2 energy only with sunlight consumption and obtain the separation of H_2 and O_2 with one membrane. Usually, in a lab test situation, apart from the two electrodes where OER and HER happen, a reference electrode is also used to form the three-electrode system for PEC water splitting measurements.

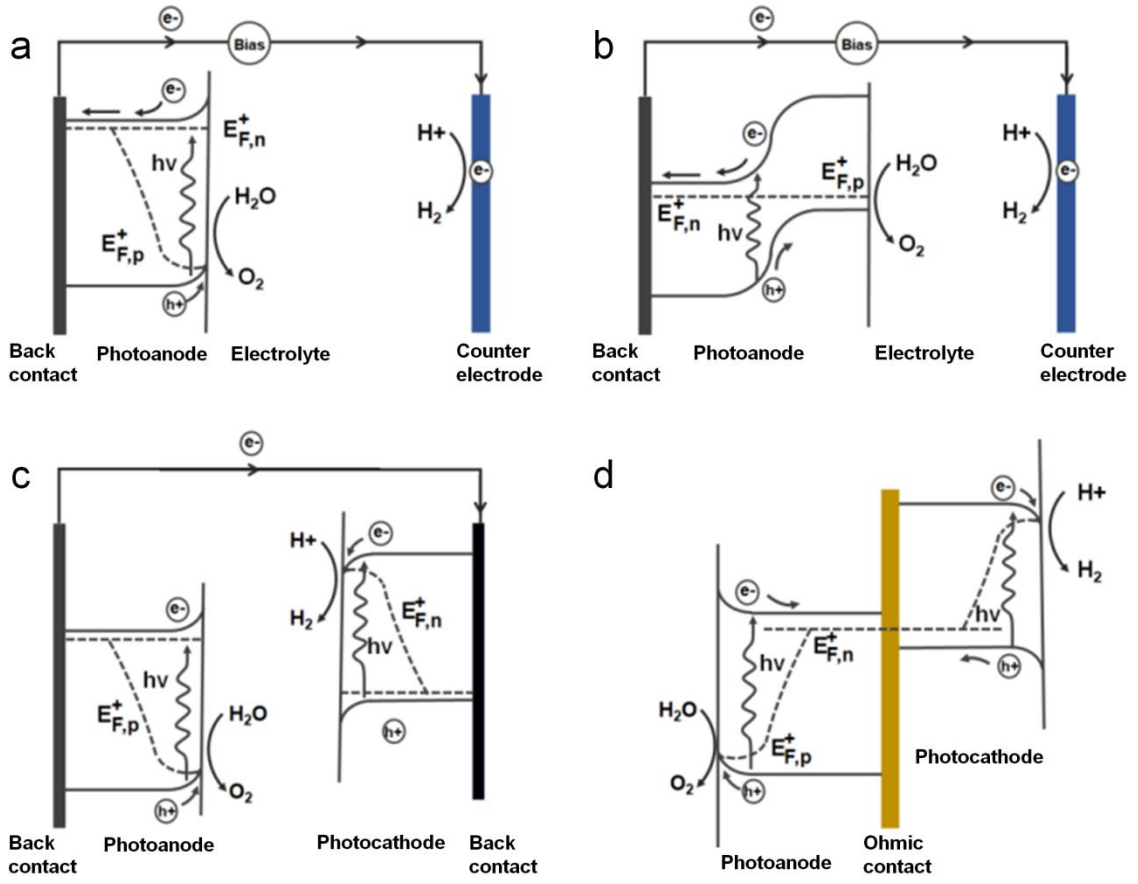

Figure 1.5 Four types of configurations for PEC water splitting solar cells. (a) A single semiconductor as the photoanode or photocathode for PEC water splitting under external bias. (b) A heterojunction semiconductor as the photoanode or photocathode for PEC water splitting under external bias. (c) A wired PEC tandem cell by connecting a photoanode and a photocathode. (d) A wireless PEC tandem cell based on ohmic contact or p-n junction.[16-17]

1.3. Selection of semiconductors for photoelectrodes

For PEC water splitting, photoelectrodes have great impact on the light harvesting process, especially in the separation and transfer of photogenerated charges and interfacial charge transfer. Generally, three main characteristics are required for an ideal water splitting photoelectrode: 1) suitable band gap energy and band position, 2) efficient charge carrier separation and transportation in the photoelectrode, and 3) powerful catalytic activity and stability.[16] Therefore, it is very important to choose suitable semiconductors as photoelectrodes that absorb the light contributing to the produced photocurrent. As shown in Figure 1.6, in terms of natural sunlight, the visible light accounts for ~43% of the solar energy spectrum, and ~7% is ultraviolet (UV) light.[18] To obtain high activity, the semiconductor in a solar cell should have a suitable band gap, which can be able to absorb visible light. Considering the thermodynamic energy losses and the overpotential for acceptable surface reaction kinetics, a required minimum band gap is ~1.8 eV in line with the light absorption at ~700 nm.[16] In recent years, scientists developed and exploited efficient and stable semiconductors, including Si, oxides, chalcogenides, (oxy)nitrides, and III-V compounds, among others. As shown in Figure 1.7, several semiconducting materials have been used as photoelectrodes for light energy harvesting.[19]

In previous reports, TiO_2,[20-21] WO_3,[22-24] a-Fe_2O_3,[25-26] ZnO,[27-28] $BiVO_4$,[29-30] Ta_3N_5[31-32] and TaON[33-34] have been used as photoanodes, whereas Cu_2O,[35-36] $CuFeO_2$[37] and $CuInS_2$[38] have been exploited as photocathodes. Usually, these photoelectrodes are polycrystalline semiconductor materials, whose carrier mobility and carrier diffusion length are pretty limited.[39] The charge separation can be determined by the band bending at the semiconductor-electrolyte junction, which shows an extreme sensitivity to the chemical and physical features of the semiconductor-electrolyte interface.[40-41] Also, the existence of large amount of grain boundaries, defects, trap states or lattice mismatches in polycrystalline semiconducting materials can easily induce the occurrence of charge recombination. On the other side, some single crystalline semiconductors, including Si and III-V compounds (e.g. InP, GaAs, GaP and GaN), have been widely used as photoelectrodes, and many of them show excellent charge transport performance due to their high carrier mobility.[16,41-42] Their good crystal structure has few defects and lattice mismatches, resulting in low bulk-recombination. PEC water splitting solar cells

consisting of single crystalline semiconductors enable to separate photo-generated charges by introducing a solid-state buried junction, which is conducive to obtaining a high device efficiency.[43]. In addition, the stability and corrosion of the semiconductors immersed in the electrolyte also need to be considered.

However, usually the semiconductors used as photoelectrodes for PEC water splitting process still have their drawbacks.[42,44-46] For example, TiO_2 is highly stable in a wide range of pH in aqueous electrolytes and has good catalytic properties, but it shows low conductivity and only can absorb the UV light due to its large band gap (3.2 eV). WO_3 with a band gap of 2.7 eV is also only active in the UV region of the solar spectrum, but it is less stable in acidic conditions and unstable in alkaline conditions. Fe_2O_3 and $BiVO_4$ have a smaller band gap and absorb a part of visible light, but Fe_2O_3 has poor conductivity and low absorption coefficient, presenting very poor photocurrent stability. Cu_2O, as one of the most attractive p-type semiconductors, is a superior solar absorber due to its small band gap (1.9-2.2 eV), but the photocorrosion issue limits its application. Compounds like CdTe or InP also have smaller band gaps that are better matched to the spectral distribution of solar reaching the earth, but they either become inert or corrode when engaged as photoelectrodes in aqueous electrolyte.

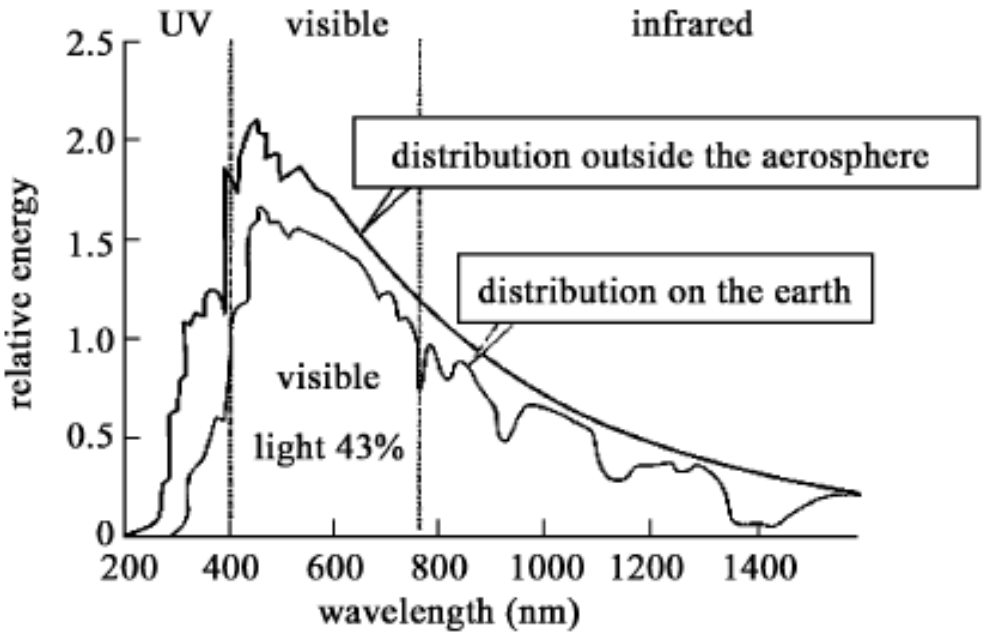

Figure 1.6 The solar energy spectrum.[18]

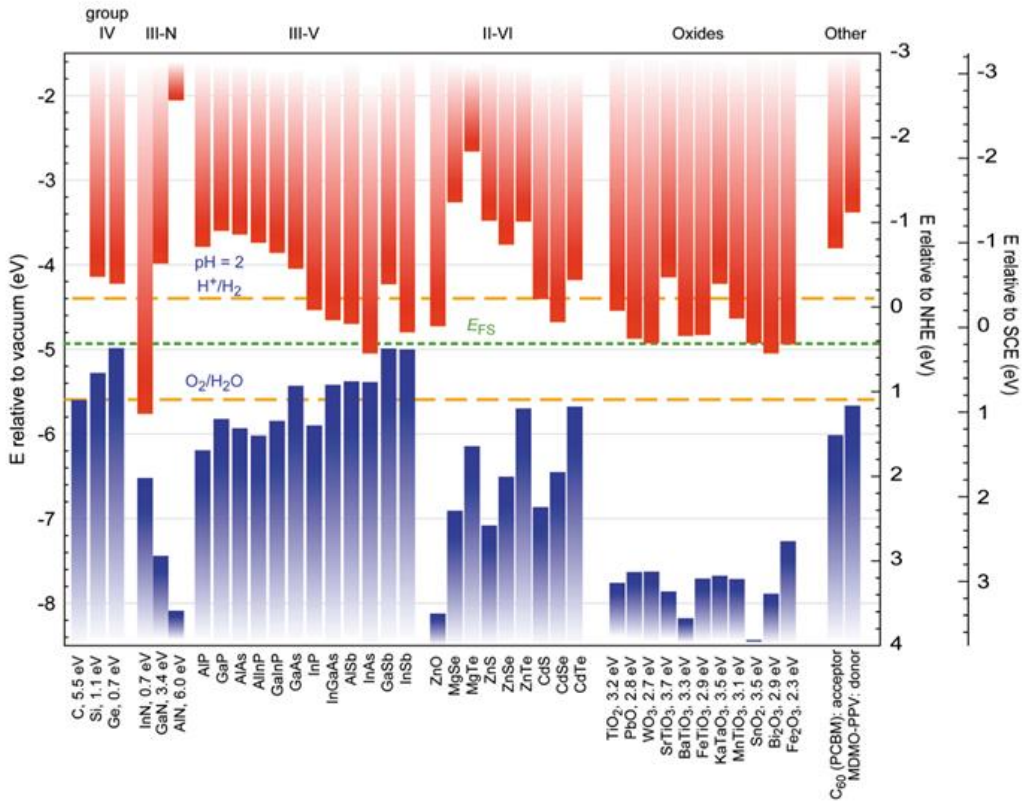

Figure 1.7 Energy band diagrams of common semiconductor materials.[19]

Apart from having a suitable band gap that results in a high efficiency, low cost of fabrication, durability and low cost and ease of maintenance also has a very significant impact on the solar cells. Interestingly, although Si semiconductor material is unstable in acid or alkaline aqueous solution, it shows a suitable band gap (~1.1 eV) which matches with the solar energy spectrum and enables to absorb a large amount of visible light. In theory, under air mass (AM) 1.5G one sun (100 mW/cm^2) illumination, Si material could generate a maximum photocurrent of ~44 mA/cm^2.[41] Moreover, as the second most abundant element in the Earth's crust (about 28% by mass) after oxygen, Si is cheap and readily used in multiple industrial products. Therefore, these advantages make Si become one of the most attractive semiconductors for constructing PEC water splitting devices.

In the past few decades, although Si has been widely employed for water oxidation and water reduction due to the previously described advantages, there are three main issues limiting the utilization of Si as photoelectrodes in PEC water splitting solar cells.[41] First, a planar Si/water interface can reflect a large part of the incident visible

light.[47] Second, when immersed in an aqueous electrolyte, Si electrodes undergo photoanodic corrosion due to its susceptibility to oxidation. Then the electrically insulating SiO_2 layer is able to cause the failure of the device.[48-49] The third major limiting factor is from the slow water splitting kinetics on Si surfaces. In order to conquer these issues, significant progress has been achieved on the basic principles, devices design, and the fabrication and screening of cost-effective catalysts.[50] In general, different strategies have been exploited to protect Si-based photoanodes, including: 1) depositing metal films (e.g. Ni) on the surface of SiO_X/Si, 2) coating catalytic transition-metal oxide layers (e.g. NiO_X, CuO_X) and 3) depositing a thin layer of Al_2O_3 or amorphous TiO_2 in-between Si photoelectrode and cocatalysts by atomic layer deposition (ALD), among others.[51-53] Similar to Si-based photocathodes, an anticorrosion protection layer also can be coated on the surface of Si. For example, Ji et al. demonstrated that Si photocathode covered with an epitaxial $SrTiO_3$ protection layer and then decorated with mesh-like Ti/Pt nanostructure for water reduction achieved a high photocurrent density of 35 mA/cm^2 and a long stability of 35 h in 0.5 M H_2SO_4 electrolyte.[54]

1.4. Metal and metal oxide films based coatings as catalysts for PEC water splitting

Due to the instability of Si materials towards corrosion, the deposition of metal or metal oxides layers is an effective method to protect the surface of the semiconducting photoelectrodes in contact with aqueous electrolytes. Furthermore, the metal or metal oxide layers can also play the role of catalyst, boosting the chemical reactions (Equations 1.1-1.4). Usually, the films covering the semiconductors can be deposited by different methods, being electron beam evaporation, magnetron sputtering and ALD the most common.

Compared to HER, the OER has more sluggish kinetics and is more complicated, since it needs to transfer four electrons and remove four protons from water to produce one O_2 molecular. In contrast to Si photocathode, although n-Si or p^+n-Si with a small band gap have widely employed as photoanodes, the oxidation of Si occurs much easier on the Si photoanode/electrolyte interface. At the interface, the holes excited by high-energy incident photons will encounter and react with Si surface atoms, resulting in a thick insulting SiO_X layer able to impede the charge transport. That is to say, this effect plays a substantial role in inhibiting the PEC water splitting process.

During past years, numerous efforts have been dedicated to develop sustainable and efficient Si-based photoanodes replacing the photocathode for PEC water splitting process. In terms of OER, ruthenium oxide (RuO_2) and iridium oxide (IrO_2) are recognized as the best catalysts due to their high catalytic activity and endurance in acid and basic electrolytes, which have been utilized in some published work.[55-62] Take Ir as an example, Chen et al. constructed a metal-insulator-semiconductor (MIS) junction based n-Si photoanode with IrO_2 layer as catalyst (shown in Figure 1.8) for PEC water oxidation.[59] Interestingly, the photoanode achieved longer stability due to the thin protecting TiO_2 layer deposited by ALD. Furthermore, more works also have been reported by introducing Ti or TiO_2 as the protective interlayer to enhance the durability for OER.[52,63-69] However, the widespread application using Ru and Ir based materials as catalysts has been severely limited by the excessive cost of these noble metals.

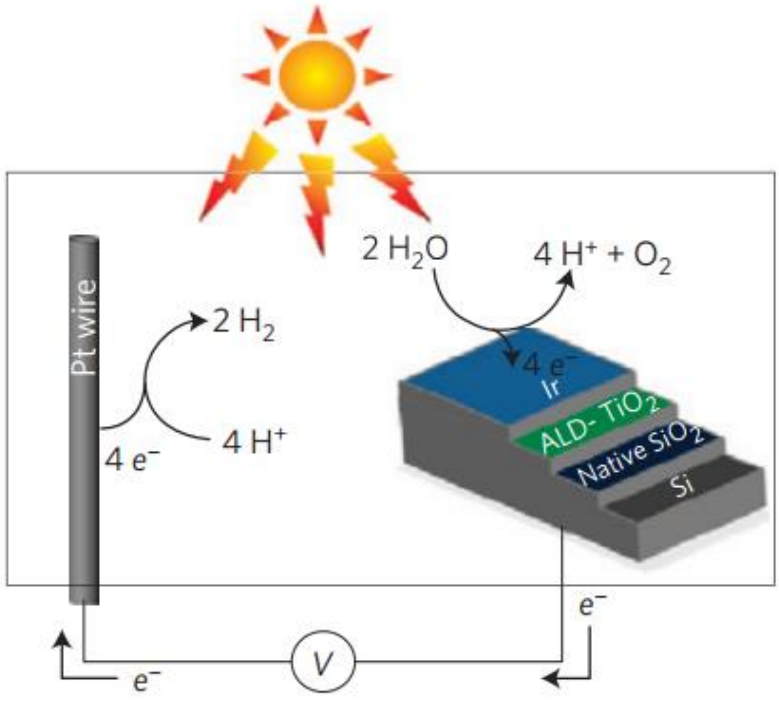

Figure 1.8 Ir/TiO_2/Si based photoanodes for PEC water oxidation reaction.[59]

Considering the cost for fabrication of the photoanodes, various cheap non-precious metals, metal oxides, and sulfides (among other) are being intensively investigated for PEC water splitting. Nickel, which is earth-abundant and has a high work function of ~5.15 eV, has attracted a lot of attention for photocatalysis due to its corrosion

resistance and reasonable stability. So far, Ni based catalysts have been widely used to protect the surface of Si and serve as an active material for water oxidation.[49,52,63-66,70-73] Especially, Sun et al. reported NiOx/Si photanode achieving a very long stability of over 1200 h in strong alkaline electrolyte.[71] During PEC water splitting, Ni thin films act as a multifunctional layer that 1) forms a Schottky junction with n-Si to generate a high photovoltage, 2) provides good protection for the underlying n-Si substrate, and 3) serves as catalyst (when oxidized in the electrolyte) for OER. Some efforts related to Ni based coatings as catalysts for PEC water splitting are shown in Table 1.[66] In addition, other transition metal oxides,[74-78] metal-based alloy[67,79-82] and mixed metal oxides[68-69] have been used as catalysts to enhance the PEC performance of Si-based photoanodes.

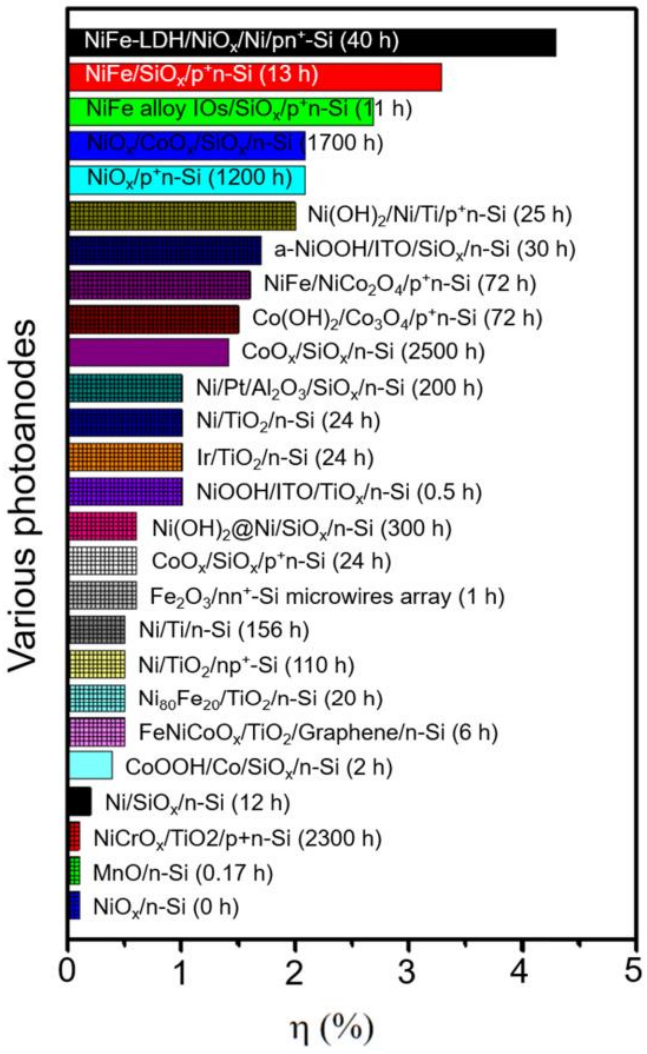

Figure 1.9 Chart visualizing data on reported energy conversation efficiency (η) and stability tests of various Si-based photoanodes for OER. The η of the photoanodes with

pure color are directly presented in the literatures, while others with small grids are calculated from current density-voltage (J–V) curves in the corresponding literatures.[41]

Moreover, to enhance the photovoltage, many scientists introduced a buried p-n homojunction (i.e. same semiconducting material with p and n regions) on the photoelectrodes by use of a doping/diffusion process, as reported in refs. [52,65,69,71,75-76,79-83]. Although this straightforward way can achieve a significant enhancement in photovoltage, high temperatures and complex operation to form a functional photoelectrode are necessary during the doping/diffusion process. To overcome these issues, Digdaya et al. developed an MIS based Ni/Pt/Al_2O_3/SiOx/n-Si photoanode, exhibiting a long-term durability of over 200 h and a sufficiently high photocurrent and photovoltage after activating the metal layer at the surface in strong alkaline electrolyte.[51] The high photovoltage results from i) the dual-oxide layer (Al_2O_3/SiOx) separately designs the semiconductor/insulator and insulator/metal interfaces, which is beneficial to unpin the Si Fermi level at the Si/insulator interface; ii) Pt/Ni metal layer can decouple the functionalities to obtain a higher effective barrier height and a high-efficiency catalyst for the composite photoelectrode; iii) dual metal overlayers can thoroughly protect the underlying Si photoanode to obain a very long stability.[41] Figure 1.9 summarized the progress for the Si-based photoanodes in the past years.

Table 1: Ni based coatings as catalysts for PEC water oxidation.[66]

Photoelectrode	Onset potential (V vs. SCE)	Conditions
Sol–gel 37 nm NiO_X/SiO_X/n-Si	0.45	pH 7.2, 1 sun
2 nm Ni/SiO_X/n-Si	0	1 M KOH, 2 suns
100 nm Ni islands/4–143 nm TiO_2/np^+ Si or n-Si	0.05	1 M KOH, 1.25 suns
50 nm Fe-treated NiO/5 nm Ni/np^+-Si	0.02 (300 h)	1 M KOH, 1 sun
50–112 nm NiO_X/np^+-Si	0.08 to 0 (1200 h)	1 M KOH, 1 sun
5–8 nm Ni/TiO_2/n-Si	0.13	1 M KOH, 1 sun
NiO_X/2 nm CoO_X/SiO_X/n-Si	0.08 (1500 h)	1 M KOH, 1 sun
2 nm Ni/2 nm Ti/n-Si	0.05 to 0.03	1 M KOH, 1 sun

In terms of HER, as the most well-known and preferred catalyst, Pt has been widely deposited on Si-based photocathodes as protective catalyst, presenting good activity and

different operation stability.[48,54,84-89] Also some previous reports obtained the enhancement of PEC performance by introducing few Pt materials as the way of nanoparticles.[90-92] However, the application of Pt in large-scale is still restricted to a certain extent due to its prohibitive scarcity and high cost. Therefore, different efforts have been made to improve the performance of HER.

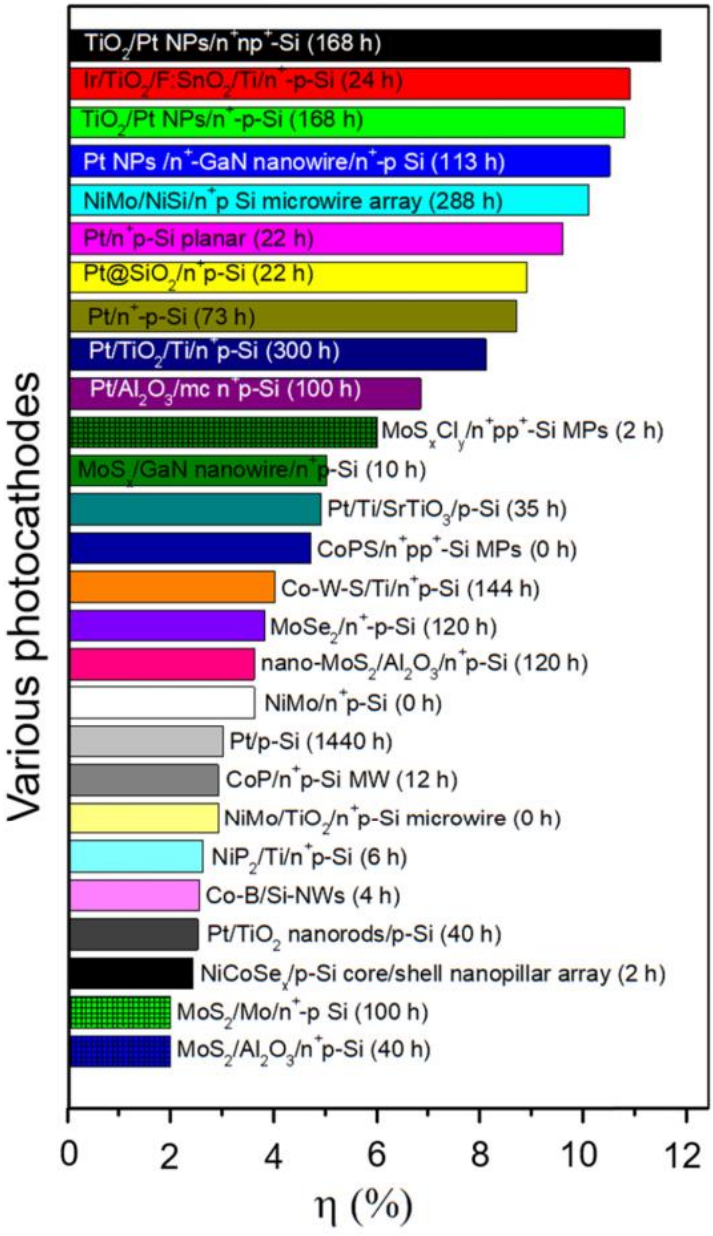

Figure 1.10 Chart visualizing data on reported η and stability tests of various Si photocathodes for HER. The η of the photocathodes with pure color are directly presented in the literatures, while others with small grids are calculated from J–V curves in the corresponding literatures.[41]

First, similar to the photoanodes, p-n junction also plays an important role on the formation of the photocathodes. Usually, p-type Si is used as the substrate, and then a n^+ thin layer can be fabricated on the surface to fulfill a photocathode, as presented in Table 2.[93] Under this circumstance, the front electrode surface mainly determines the PEC performance of the photoelectrodes. Interestingly, Shen et al. developed a different Si photocathode with an np^+ junction by alloying Al with n-Si at the back side of the photocathode.[41,85] Compared with the normal n^+p-type electrodes, np^+-Si with/without Al_2O_3 layer can show much better PEC performance. But due to the loss of Pt, the electrode only kept stable for less than 73 h.

Table 2: n^+p-Si based photocathodes prepared by different diffusion methods and dopants for PEC water reduction.[93] ADP and SOD stand for adenosine diphosphate and superoxide dismutase, respectively.

Phosphorous source	Morphology	Photoelectrode structure	Eonset (V vs. RHE)	ABPE (%)	Stability (h)	Electrolyte
ADP aqueous solution	pyramid	$Pt/TiO_2/n^+p$-Si	0.58	10.6	250	1.0 M $HClO_4$
SOD polymer solution	microwire	Pt/n^+p-Si	0.51	5	-	0.5 M H_2SO_4
SOD polymer solution	microwire	$NiMo/NiSi/n^+p$-Si	0.55	10.1	288	1.0 M KOH
CeP_5O_{14}	planar	Pt/n^+p-Si	0.56	9.6	-	0.5 M H_2SO_4
$PClO_3$	pyramid	$Pt/Al_2O_3/n^+p$-Si	0.52	6.8	100	0.5 M K_2SO_4 + 0.5 M H_2SO_4
$PClO_3$	microwire	$Pt@SiO_2/n^+p$-Si	0.44	2.9	-	0.5 M H_2SO_4
$PClO_3$	microwire	Pt/n^+p-Si	0.49	8.9	22	0.5 M K_2SO_4 + 0.5 M H_2SO_4
$PClO_3$	microwire	$Pt_2/TiO_2/n^+p$-Si	0.56	10.5	168	1.0 M $HClO_4$

Second, in past decades, lots of new classes of HER catalysts consisting of only cheap earth-abundant elements have been investigated. Transition metal dichalcogenides (TMDs) nanomaterials can be a very promising candidate to obtain excellent catalytic activity in strong acid electrolytes. For example, Seger et al. constructed a $MoSx/Ti/n^+p$-Si photocathode, in which amorphous MoS_X as a catalyst was electrodeposited on the surface and a thin Ti interlayer as a conductive protective layer. The prepared electrode showed a onset potential of 0.33 V vs. RHE and saturated current density of −16 mA/cm^2 at 0 V vs. RHE, but very short stability (1 h) under red light with AM 1.5 cut-off (< 635 nm).[94] $MoS_2/Mo/n^+p$-Si photocathode achieved a

PEC stability of 100 h with a negligible loss using a thin MoS_2 as catalytic and protective layer, while the parasitic light absorption of Mo and the lack of surface textures induced a low saturation photocurrent and a low η (less than 2%). However, Benck et al. demonstrated a higher η up to ~3.1% for $Mo_3S_{13}/MoS_2/n^+p$-Si because of the substantial improvement of the catalytic activity from Mo_3S_{13} catalyst clusters, indicating the significance of TMDs catalysts on PEC performance.[95]

In addition, various engineering approaches also have been studied to increase the edge sites and thus enhance the HER activity: 1) doping foreign atoms into TMDs to form ternary structures,[96-97] 2) inserting a buffer layer (Al_2O_3 or Ti) or a linker between Si and catalyst.[98] Also, different metallic alloys (e.g. NiMo) as catalysts also have attracted attentions to enhance the PEC performance for HER.[99-100] Figure 1.10 summarized the progress for the Si-based photocathodes in the past years.

1.5. Metal nanoparticles based coatings as catalysts for PEC water splitting

Apart from using metal and metal oxide films to enhance the performance of semiconducting photoelectrodes for PEC water splitting (HER and OER reactions), metal nanoparticles deposited on the surface of the semiconductor can also be a promising approach to enhance the water splitting performance. That is to say, plasmonic effects from metal nanoparticles contribute to the water splitting process, which can be mainly explained by the following reasons.[101] First, plasmonic metal nanoparticles can confine the absorbed light to the near-surface region of the semiconductor, which decreases the moving distance of the charge carriers, and thus minimizes the recombination of electrons and holes. Second, plasmonic metal nanoparticles are beneficial to achieve better light absorption for the semiconductor. So, the amount of the used semiconductor as a photoelectrode can be reduced, resulting in low production costs. Third, the semiconductor with large band gap only can absorb a small proportion of solar photons, leading to a low solar-to-hydrogen conversion efficiency. But plasmonic metal nanoparticles can make the semiconductor sensitize to the light below the band gap, resulting in the excited electron injected into the CB of the semiconductor.[101] Fourth, large plasmonic metal nanoparticles can preferentially scatter the incident light into the semiconductor with high refractive index, obviously reducing the reflection of the semiconductor to an almost negligible level. In addition, the higher surface area of the water splitting devices can improve charge separation, but

the available photovoltage will decrease by 59 mV for each order of magnitude increase in surface area.[10] The reason is that at the near-surface region the concentration of minority charge carriers is diluted, accordingly changing the Fermi level of minority charge carriers and correspondingly altering the open-circuit photovoltage. One possible solution to obtain higher photovoltage in the device is to reduce the semiconductor/electrolyte interfacial area, lower than the projected surface area of the semiconductor.[101]

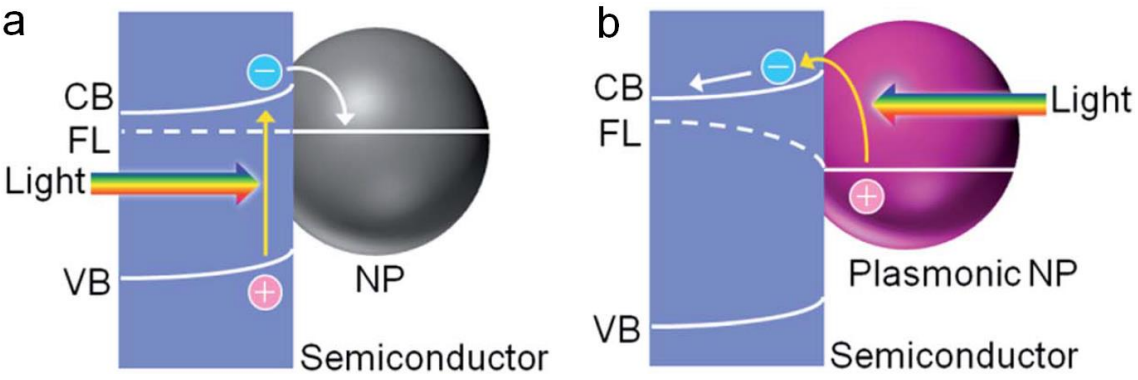

Figure 1.11 Mechanisms of (a) the cocatalysis effect and (b) the LSPR effect of metal nanoparticles.[102]

During last years, different types of metal nanoparticles have been decorated on semiconductors to form metal/semiconductor (M/S) structures for photocatalytic or PEC water splitting. It has been observed that the nanoparticles can enhance the water splitting efficiency by providing active and trapping sites for the photogenerated charges, and facilitating the charge separation, as shown in Figure 1.11a. Moreover, the nanoparticles present local surface plasmon resonance (LSPR) phenomenon (Figure 1.11b) that collects solar energy to mediate the reaction to produce and transfer plasmonic carriers.[103] These two catalytic mechanisms involved in M/S hybrid photocatalysts are the Schottky junction and the LSPR effect, respectively. The distinct directions of interfacial charge transfer provide one way to distinguish them.

In detail, on one hand, a Schottky junction can be formed when a metal and a semiconductor are in close contact. For example, for an n-type semiconductor, the work function of the semiconductor is smaller than that of the metal. In such case, the Fermi level of the semiconductor and the metal will be aligned by the transfer of the free electrons from the semiconductor to the metal. Therefore, one upward band bending

will be formed by the charge diffusion, and this junction is named a Schottky junction.[103-105] As observed in Figure 1.11a, the metal enables to trap the CB electrons of the semiconductor under light illumination, inducing high separation and transportation of the electron-hole pairs.[103] That is to say, the metal enhances the photocatalytic reaction by the catalytic effect. On the other hand, as shown in Figure 1.12a, the LSPR is the strong collective oscillation of surface electrons, which can happen when the frequency of incident light on a metal particle and its free charges match.[103] And the LSPR wavelength is defined as the specific wavelength with the largest oscillation amplitude.[106] In such light illumination, the LSPR effect remarkably enhances the photoreactivity in the following three ways:

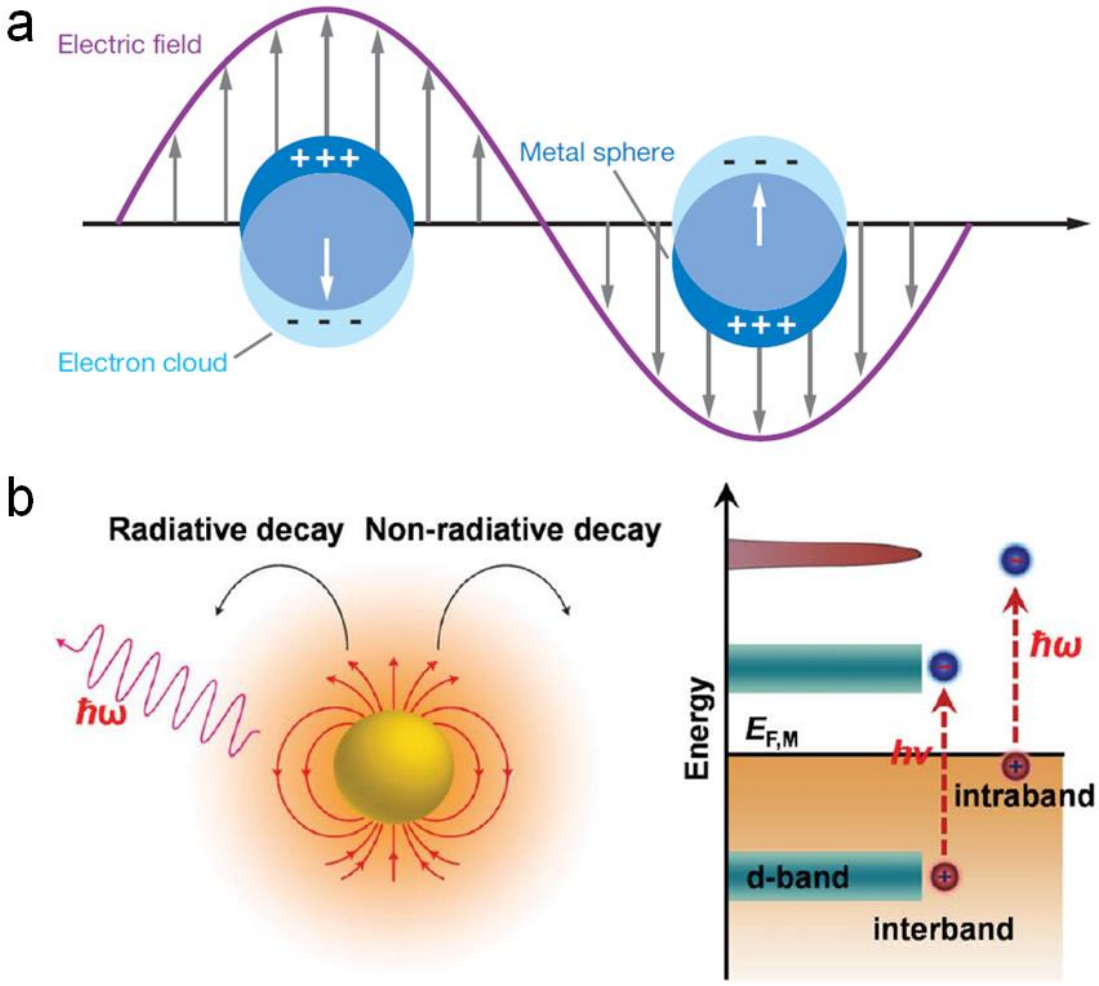

Figure 1.12 (a) A localized surface plasmon for a spherical gold nanoparticle. (b) Plasmons in metal nanostructures can decay via a radiative pathway with re-emitted photons or via a non-radiative pathway that generate hot carriers.[103]

1) Enhanced light harvesting. The ability of a photocatalyst to harvest light determines the amount of generated charge carriers, which plays an important role in the PEC performance. When plasmonic metal nanoparticles are deposited on a semiconductor, light absorption and scattering could increase the light trapping efficiency.[107] It's worthy to note that the morphology and size of a plasmonic metal could extremely influence the plasmonic absorption. Therefore by adjusting the related parameters, it's feasible to achieve the optimized M/S nanostructure. For instance, Li et al. investigated TiO_2 photoanodes decorated by Au with three different shapes (i.e. nanoparticles, nanorods and a mixture of nanoparticles and nanorods) for PEC water oxidation in strong alkaline electrolyte.[108] The experimental data indicated that the two types of TiO_2 electrodes with Au nanoparticles (Au NPs) showed enhanced photoactivity under the entire UV-visible light, suggesting that Au NPs effectively boost TiO_2 to absorb UV light and amplify the LSPR electrical field. More significantly, this nanostructured design could provide us good ideas to build highly effective PEC water splitting devices working both in UV and visible light.

2) Enhanced local electric field. Plasmon resonance energy transfer (PRET) is defined as the transfer of energy from a plasmon to a semiconductor. The effect of PRET usually working in a small and well-defined region of the semiconductor, can increase the power by enhancing the electric field intensity. As shown in Figure 1.12a, near the plasmonic nanoparticles, a strong electric field can be generated along with the LSPR, which is another significant mechanism in M/S photocatalytic reaction.[103] By introducing Ag nanoparticles, Kumar et al. and Kulkarni et al. demonstrated that the local intensity of the electric field has a great effect on the generation and separation of electron–hole pairs in the semiconductors.[109-110] More specifically, the weaker the intensity, the lower the efficiency. Furthermore, with the distance from the the M/S interface increasing, the intensity of enhance electric field will sharply decay,[109] These information reveals that the direct coupling of the metal and the semiconductor could obviously reduce the distance and thus promote the photocatalytic activity.[111] In addition, the curvature of the metal nanocrystals also has an intense influence on the improvement of the electric field intensity, that the sharper the metal nanocrystal, the stronger the field enhancement.[112] In a word, the scientists shold take the size and shape of the metal nanocrystal into account when designing M/S nanostructures with strong electric field intensity.

3) Hot electron injection. As observed in Figure 1.12, under the LSPR excitation, energetic charge carriers (hot electrons and hot holes) at the metal surface could take place during the non-radiative or radiative decay of the LSPR on a femtosecond (fs) timescale.[103] The non-radiative decay carrys on via the intraband excitation (between the Fermi level and CB) or interband excitation (between d band and CB). As shown in Figure 1.11b, when combining plasmonic metal nanoparticles with a semiconductor, the generated hot electrons will be transported near the M/S interface and finally injected into the semiconductor, distinctly enhancing the photocatalytic property.[103] Note that the the injection of hot electrons is influenced by the size, shape and intrinsic characteristics of plasmonic metal nanoparticles, as well as the adjacent semiconductor photocatalysts. Figure 1.13 clearly shows the functions of metal nanoparticles/n-type semiconductor nanostructure for PEC water oxidation.[101]

To date, numerous efforts have been devoted to develop inhomogeneous M/S Schottky junctions based photoelectrodes without protection layer. Although many reported works have demonstrated the effective enhancement of non-noble M/S nanostructure for water splitting,[113-117] noble metal nanoparticles (i.g. Au, Pt and Ag) on the surface of semiconductors still play an essential role for solar-driven water splitting. In photochemical water splitting, in terms of Pt noble metal, it has many advantages including good stability, ultrahigh conductivity, and even largest work function and lowest overpotential among all the metals for HER.[118] Thus compared to other metals, Pt can be considered as the best cocatalyst. Also, based on the Schottky junction nanostructure, Pt can cleverly trap the electrons generated by light-harvesting semiconductor, reducing the recombination of electron-hole pairs. Atabaev and co-workers clearly demonstrated the PEC enhancement for water splitting by depositing Pt NPs on the surface of TiO_2 nanorods.[119] Considering the PEC water splitting with the LSPR effect, Au can be the most promising metal due to its plamonic property induced by visible-to-near-infrared region.[120] More interestingly, by tuning the shape, size and morphology of Au nanocrystals, the photelectrodes can achieve high catalytic activity due to the optimized plamonic property.[108,121] All this information gives the researchers good ideas to design the solar-induce water splitting devices with high performance. Moreover, even if an additional insulator (i.g. TiO_2 or Al_2O_3) is used as the interlayer between the semiconductor and the metal, the entire photoanode can still benefit from the LSPR effect of the nanoparticles.

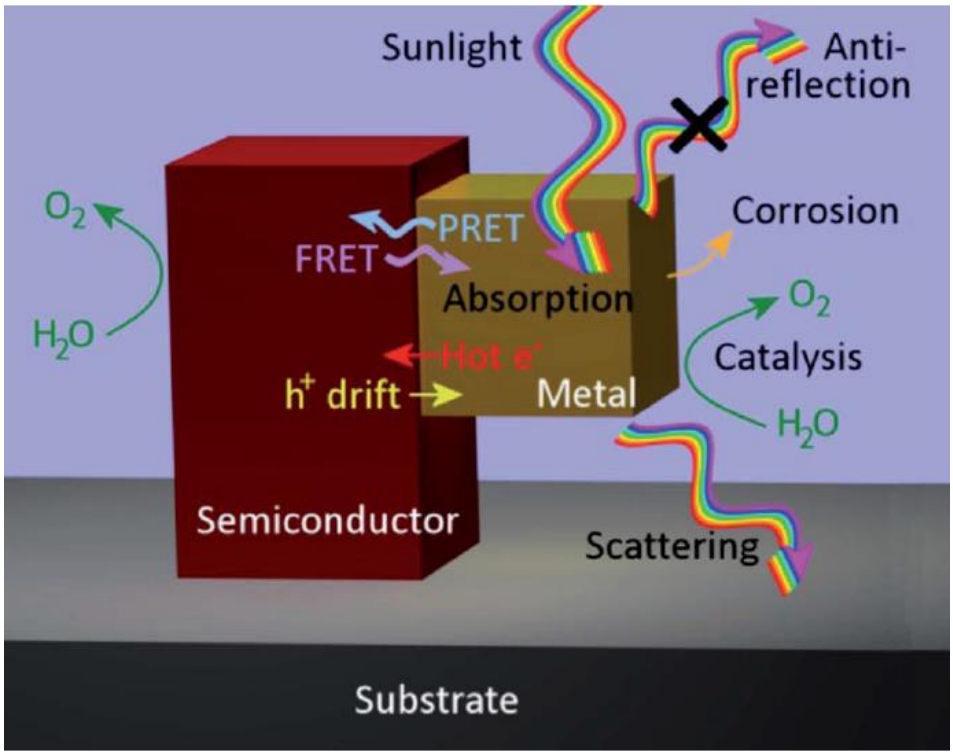

Figure 1.13 n-type semiconductor nanostructure located on a metallic substrate in contact with aqueous electrolyte and a metal nanoparticle. The relevant optical, electronic and catalytic effects of the metal nanoparticle are illustrated.[101]

1.6. Effect of electrolytes

In a PEC water splitting system, an electrolyte (acidic, neutral or basic) is also a necessary part, since it contributes to the ionic migration in the internal circuit. First, an important principle to select electrolytes is good conductivity for smoothing charge transfer in the circuit. Exploiting active cations like Na^+, K^+, and anions like OH^-, SO_4^{2-} with suitable concentration (~0.1 M or above) contributes to minimize solution resistance and promotes band bending.[122] Therefore, using highly conductive electrolytes is critical for the PEC water splitting process. Many common electrolytes have been used, such as H_2SO_4, Na_2SO_4, K_2SO_4, NaOH, KOH, phosphate buffer solution, among others.

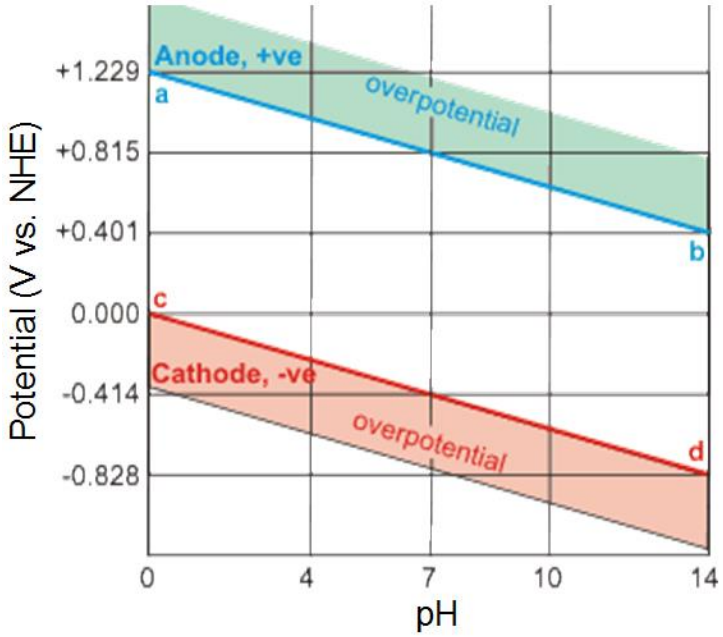

Figure 1.14 Electrode potentials versus pH for water electrolysis.[123]

Generally, in aqueous acid electrolyte, water reduction or HER can occur easily; on the contrary, water oxidation or OER is prone to happen in aqueous alkaline electrolyte. As observed in Figure 1.14, it shows the electrode potentials as the function of pH for water electrolysis.[123] Moreover, the pH values also can affect the redox potential of the stability of the photoelectrodes and the rate for water splitting reaction.[124] As for OER, high concentration of H^+ ions will inhibit the proceed of the half reaction to generate O_2. From the point, low pH is not conducive to water oxidation, which is confirmed by table 3. Simultaneously, the change of pH value also can lead to a shift of the band level of semiconductor materials.[125] Moreover, the electrolytes should be compatible with the used phototelectrodes, meaning that the electrolytes can't have the same light absorption range and chemical interactions with the photoelectrodes.[126] For instance, Hill et al. investigated n-type WO_3 photoelectrodes for water oxidation in various electrolyte types and pH values, as shown in Table 3, indicating that the oxidation efficiency is influenced by the electrolyte types and pH values.[24] When immersed in CH_3COOH, CH_3COONa, and NaCl electrolytes, WO_3 are unable to produce O_2 due to the incompatibility of these electrolytes and the photoanode. In terms of different anions, the regularity of the pH effects differs. For example, with the pH increasing, the conversion efficiency displays an upward trend in NaH_2PO_4, but declines in $NaClO_4$, which probably is attributed to the intrinsic properties of the electrolytes.

Table 3. Summary of the conversion efficiencies of photocurrent to oxygen acquired in some electrolytes with varied pH conditions and anions.[24]

Electrolytes	pH	Photocurrent to oxygen conversion efficiency [%]
CH_3COOH	3	0
CH_3COONa	5	0
NaCl	1	0
NaCl	3	0
NaCl	5	0
NaH_2PO_4	1	0
NaH_2PO_4	3	33
NaH_2PO_4	5	58
$NaClO_4$	1	79
$NaClO_4$	3	32
$NaClO_4$	5	29
Na_2SO_4	1	9
Na_2SO_4	3	63
Na_2SO_4	5	88

Besides, a minor change in the electrolyte conditions possibly induces a major change in the interface catalysis. As observed in Figure 1.15a, the initial photocurrent density of Co_3O_4/TiO_2 photoelectrodes displayed a tiny difference in NaOH, LiOH and KOH electrolytes, but after 11h continuous PEC tests the currents illustrated a ratio of 1:1.5:1.3.[126-127] Similar results were obtained from the experiments of TiO_2, MnO_X/TiO_2, $BiVO_4$ and others, which demonstrated an unexpected trend of $Li^+ > K^+ > Na^+$ on the PEC water oxidation activity and stability (Figure 1.15b) in alkaline electrolytes with different cations.[126] This phenomenon is resulting from a balance of the following two factors: 1) the apparent extents of the weakening of O−H bonds on the sample surface after interaction with the hydrated cations, and 2) the different rates of the backward reaction (oxygen reduction) in various electrolytes (Figure 1.15c and d). And Li^+ ions not only provides the most important extent of O−H activation but also is most effective in avoiding the reverse reaction.[127] In general, further understanding the roles of electrolyte ions is critical for PEC water splitting, which may provide a new approach to facilitating surface catalysis by tuning the electrolyte conditions, such as pH, ion species and the concentrations.

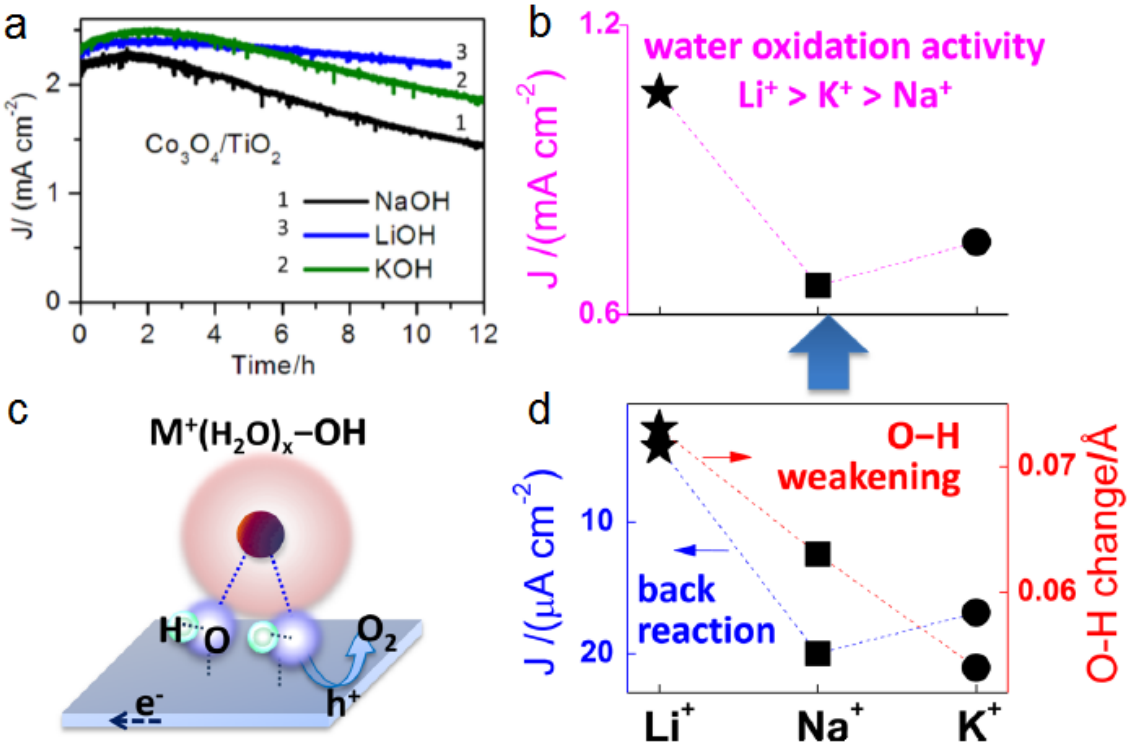

Figure 1.15 (a) Chronoamperometry measurements on Co_3O_4/TiO_2 photoelectrodes at 1.23 V vs. RHE in 1.0 M NaOH, LiOH and KOH electrolytes (Light density of 300 mW/cm^2 provided by a Xe lamp) and (b) the photocurrent of TiO_2 photoelectrodes at 1.23 V vs. RHE after PEC operation for 10 h. (c) Schematic illustration of the interaction between hydrated cations and OH species on the electrodes surface. (d) The backward reaction activity of the TiO_2 photoelectrodes and the weakening extent of O−H bonds after interacting with different cations.[127]

1.7. Materials characterization techniques

1.7.1. Scanning electron microscopy

Since Manfred von Ardenne for the first time invented a true microscope with high magnification in 1937,[128] this technique attracted large amounts of interest among scientists for the improvement, production and application. As a type of electron microscope, a scanning electron microscopy (SEM) can obtain images of the samples by scanning the surface using a focused beam of electrons. When the electrons interact with atoms at various depths in the sample, various signals will be generated including secondary electrons (SE), reflected or back-scattered electrons (BSE), characteristic

X-rays, transmitted electrons, among others. In terms of secondary electron imaging (SEI), SE are excited by the electron beam and then emitted by atoms from very close to the specimen surface, resulting in very high-resolution (better than 1 nm) images for the sample surface. The beam electrons reflected from the specimen by elastic scattering are called BSE, emerging from the deeper positions in the sample. Therefore, the resolution of SE images is higher than BSE images.

SEM has obvious advantages for characterizing the materials: 1) easy samples preparation. The conductive materials are able to be directly put into the specimen chamber for analysis, while the samples with low conductivity or insulated materials need spray a conductive layer; 2) large field of view and high magnification with wide continuous adjustable range from 10 to 3000000 times; 3) large depth of field causing three-dimensional characteristic appearance benefit to observing the fine structure of various samples with uneven surface. So far, SEM has been widely used in the field of different researches (e.g. chemistry, materials, semiconductor manufacturing and biology) and industrial departments.

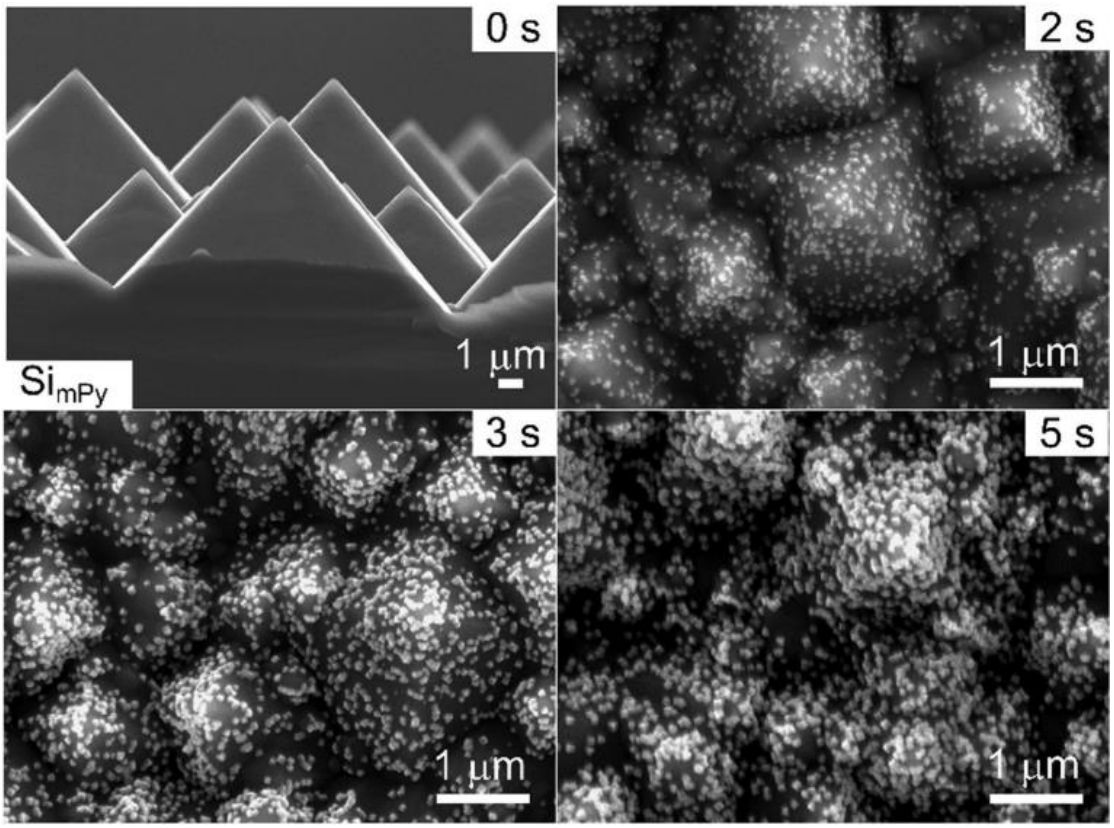

Figure 1.16 Cross section (top left) and top view SEM images showing Fe NPs electrodeposited on micropyramidal n-Si (111), with times varying from 0 to 5 s.[117]

Basically, SEM not only can observe the morphology of the samples, but also enable to provide analytical information about the elements distribution by the characteristic X-rays. For example, using SEM instrument, Oh et al. obviously displayed the texture of micropyramidal n-Si by cross section image with more surface area for absorbing the light, and clearly investigated the effect of the electrodeposition time for Fe nanoparticles on n-Si by top-view images (see Figure 1.16).[117] Chandrasekaran et al. reported the morphological change between the first ALD-deposition TiO_2 layer on p-Si and the second spin-coated TiO_2 layer on ALD-TiO_2/p-Si by top view, and showed the evident layer structure of TiO_2 with approximate thickness by cross-sectional view, as shown in Figure 1.17.[129]

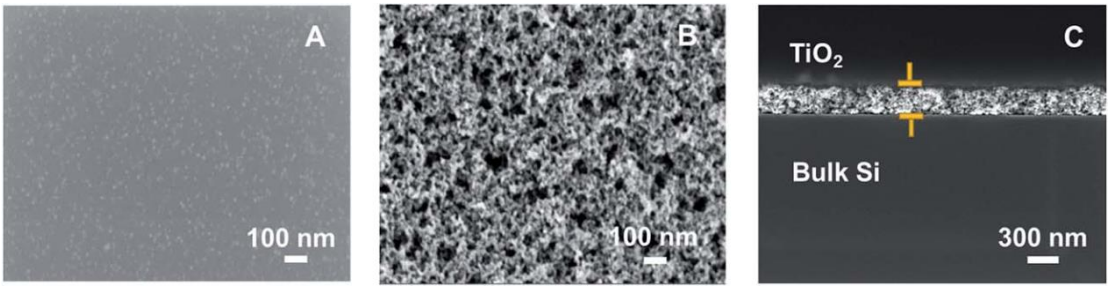

Figure 1.17 SEM images of TiO_2 layers on p-Si. (a) Plan view of ALD deposited TiO_2. (b) Plan view and (c) cross section view of ALD-TiO_2/spin-coated TiO_2 based sample.[129]

However, about the chemical characterization of a sample by SEM, an appendix energy-dispersive X-ray spectroscopy (EDX) is required. This technique can measure the energy of characteristic X-rays released when the incident electron beam ejected an inner shell electron from the sample and a higher-energy electron filled the shell. The main fundamental principle of this spectroscopy is that each element owns a unique atomic structure resulting in a distinctive set of peaks on its electromagnetic emission spectrum.[130] According to these two properties, the elements in the sample can be identified and measured their abundance, as well as mapped their distribution. For instance, by combining SEM and EDX techniques, Pishgar et al. revealed the obvious morphology and chemical composition change of the annealed n-GaP/TiO_2 surface before and after PEC measurement using the EDX distribution maps of Ga and P elements (Figure 1.18);[131] Zhang et al. displayed uniform distribution of TiO_2 nanotubes perpendicularly covered on the Ti substrate and confirmed the chemical

composition of the sample consisting of O, Ti, Au, Zn and Se elements via EDX spectrum (Figure 1.19).[132] All these works indicated that SEM and EDX play a significant impact in the field of solar-driven PEC water splitting. In this thesis, SEM is one main technique to analyze the photoelectrodes for observing the morphological changes before and after PEC water splitting.

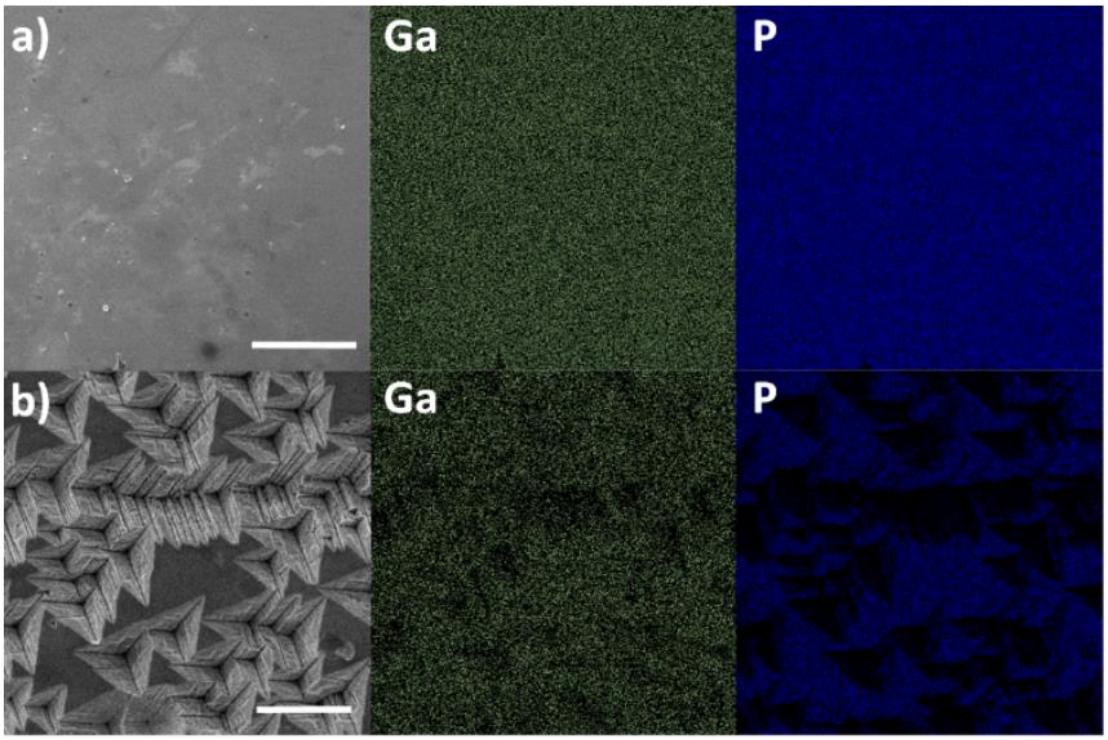

Figure 1.18 SEM images (left) and EDX maps for Ga (center) and P (right) for annealed n-GaP/TiO_2 (a) before and (b) after 4 h PEC tests at 0.2 V vs. RHE under 2 suns illumination. The scale bar is 500 µm in (a) and 100 µm in (b).[131]

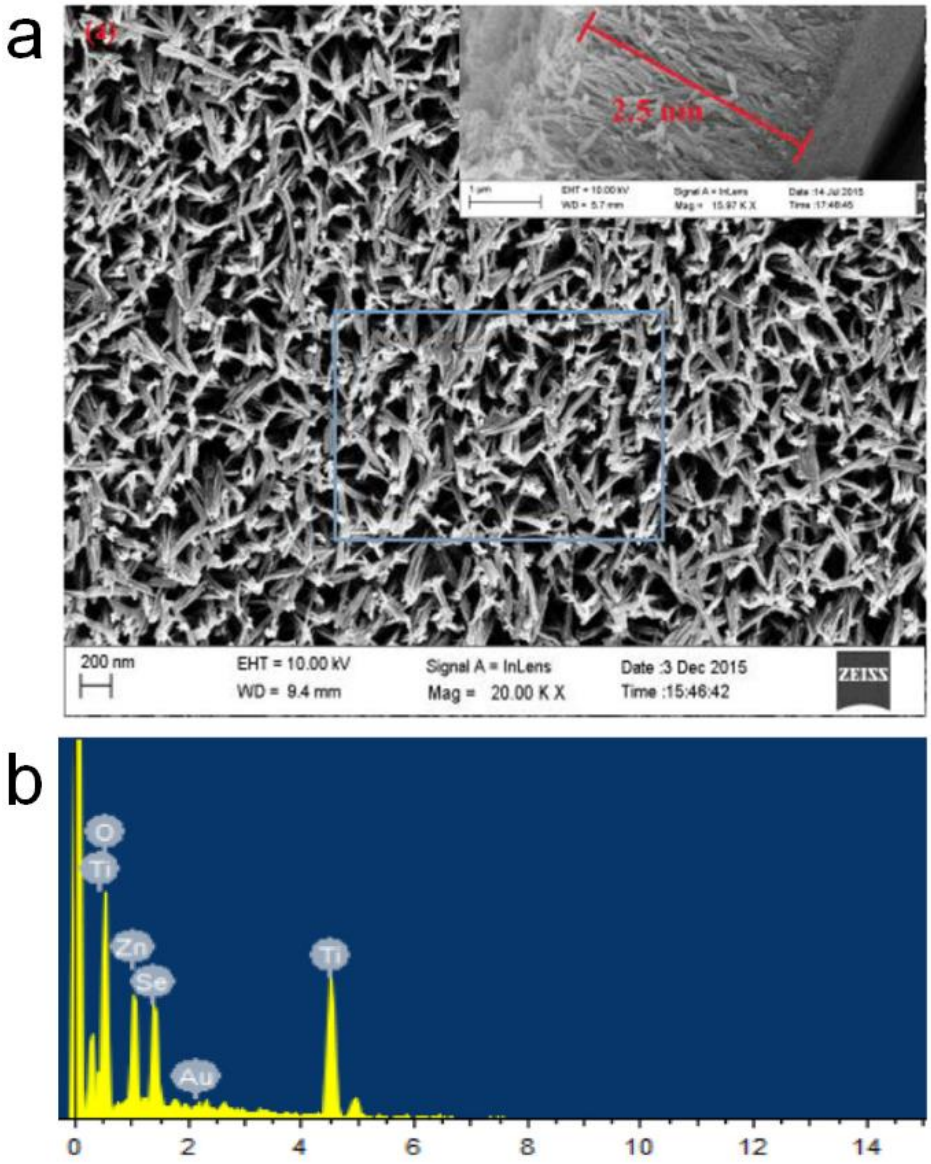

Figure 1.19 (a) SEM microphotograph and (b) SEM-EDX analysis of ZnSe/Au/TiO_2 nanotube film systems (ZATs).[132]

1.7.2. Atomic force microscopy

Atomic force microscopy (AFM) is a type of scanning probe microscopy (SPM) with very high resolution (up to the order of a nanometer). AFM was invented by Binning,[133] and then Binnig, Quate and Gerber performed the first experimental implementation in 1986.[134] Gradually, AFM reveals its wide spread applications in many aspects, including physics, biology, chemistry and medicine.

AFM is composed of a cantilever (made in Si or silicon nitride materials) with a sharp probe tip at its end which is used to scan the sample surface. When a tip is

brought near the sample surface, according to Hooke's law, the interaction between the sample and the tip causes the deflection of the cantilever, resulting in the deflection of the reflected laser beam.[135] Then the photodiode can detect the position changes of the laser, obtaining the signal about the sample topography. Usually, based on the property of the tip motion, AFM imaging modes can be distinguished into three different modes, including tapping mode, non-contact mode (both of them belong to dynamic mode) and contact mode (also called static mode).

Compared to SEM technique, AFM owns many advantages: 1) AFM is able to provide the true three-dimensional surface of the samples, while SEM only can observe two-dimensional images; 2) the AFM samples don't need any treatment, like depositing Au or carbon, which can produce permanent and reversible hurt; 3) AFM can work well in ambient environment, even in liquid environment, while SEM need operate under high vacuum conditions. However, AFM still has some shortcomings to be considered. It takes long time to obtain one image, and the imaging range is very small. Furthermore, it's worthy to note that the consumption of the AFM probes is a key problem in that their price is very expensive. Despite of these drawbacks, AFM still shows its irreplaceable effect in the field of PEC water splitting. Usually, before measuring the prepared photoelectrodes for PEC tests, the morphology and topography of the sample always is collected in nano scale by AFM. Then, different information can be confirmed, such as making sure the deposition or thickness of the catalysts, check the surface roughness and make the contrast before and after some sample treatments, among others. In deep, AFM topography images can give a clear comparison for the surface before and after PEC tests to explain the PEC performance of the photoelectrodes, as reported in Figure 1.20.[135] In the case of observing the surface topography, AFM characterized in tapping mode is the best choice compared to contact or non-contact modes. Under tapping mode, the influence from lateral force can be eliminated, and the force caused by adsorption of the liquid layer can be reduced. Importantly, the image resolution is high, and the sample surface will not be damaged by the tip (the tip also is not easy to be destroyed). Therefore, these reasons make AFM in tapping mode suitable for scanning soft, friable or sticky samples, and the cost is decreased to some extent. In this thesis, the Vecco Multimode V AFM is used to collect the surface topography information, which works without any bias. During the measurement, one iron plate with the diameter of 1.5 cm or 1.0 cm is needed to fix the sample on the sample stage.

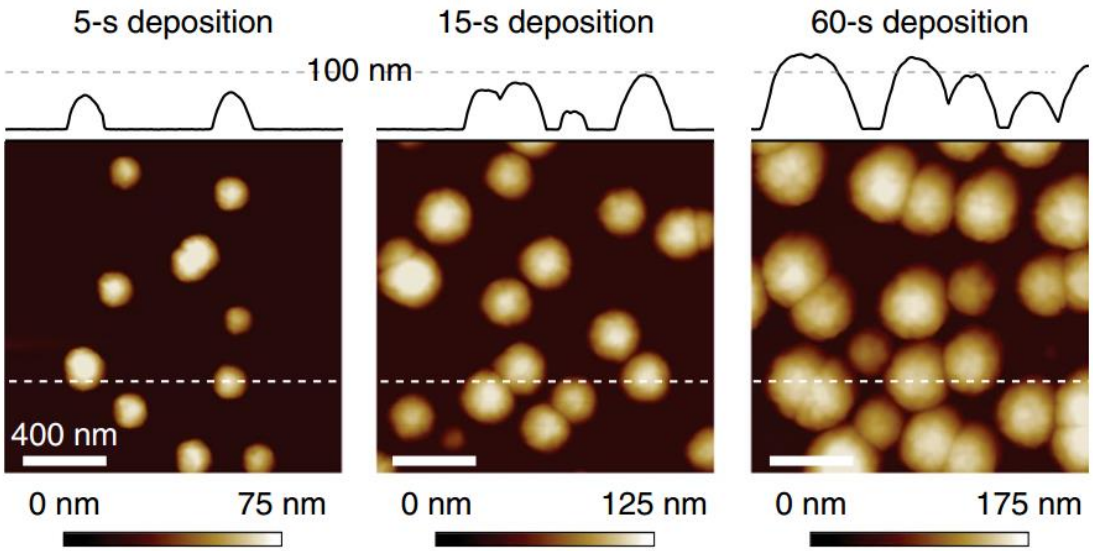

Figure 1.20 AFM topography maps collected immediately after 5 s, 15 s and 60 s deposition processes, with height line scans displayed above each image. The obtained results are characteristic of each specific samples surface, even though regions of larger/smaller islands can be observed at some positions.[135]

In addition, in some experiments, it's necessary to obtain the electrical properties of the photoelectrodes in nano scale. In this case, conductive AFM (CAFM) plays a significant role, which was developed by O'Shea and his co-workers in 1993.[136] Compared to AFM, CAFM has more requirements: 1) the tip should be conductive (usually, the probes can be diamond tip, pure metal (Pt) tip or Si covered by Pt or Ir metal materials,); 2) an additional conductive module is used to provide the voltage ; 3) a current-to-voltage preamplifier should be connected to the computer. Usually, CAFM is operated in contact mode, and there are two ways to present the collected signal. The first one is shown by current-voltage (I-V) curves, which can be collected when the tip is kept at one location under the bias. Actually, this way is very common and powerful used in the field of resistive switching. By the change of the collected current, it's very obvious to check the happen of breakdown, set or reset behavior.[137-138] The other is that the tip scans a specific region on the sample under a constant voltage, and in this case, the current map and topography can be collected at the same time. Some work related to PEC water splitting has been reported. As shown in Figure 1.21, Scherrer et al. proved the positive impact of annealing treatment on the electrical conductivity of the photoanode by topography and current mapping.[139] Also, Kant et al. investigated the conductivity of ZnO nanostructures, confirming that applying voltage or more Al

loading is attributed to the conductivity enhancement.[140] In this thesis, about CAFM measurements, a conductive silver paint is used to fix the sample on an iron plate for forming a conductive path. By combining CAFM with the probe station, the electrical properties were collected before and after PEC water splitting measurements in the nano and device scale. This gave a further evidence for confirming the stability of the photoelectrodes.

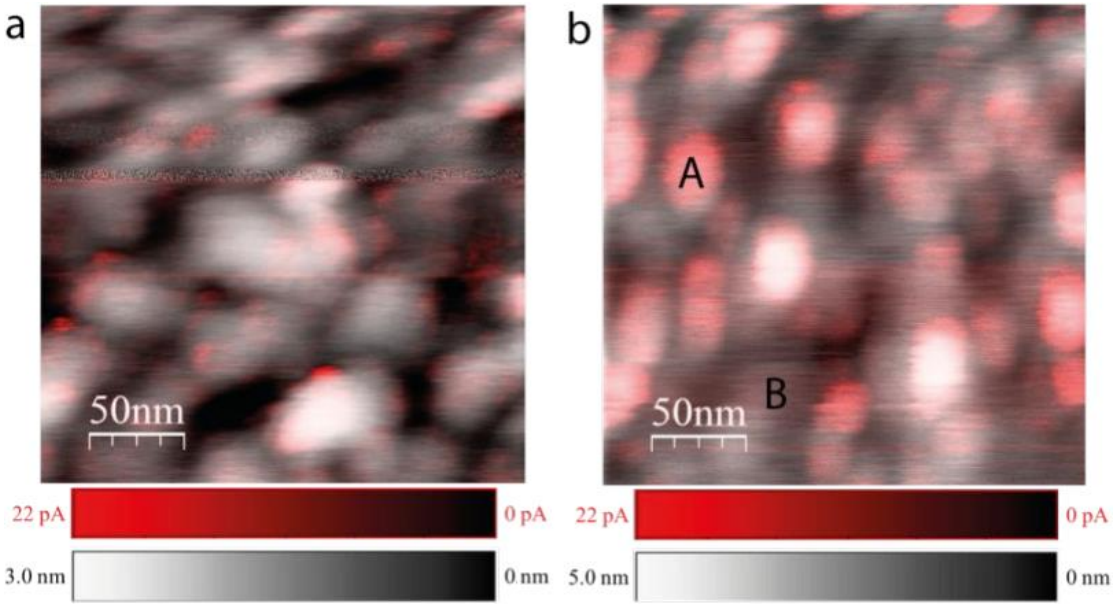

Figure 1.21 CAFM current map (at 2 V, red scale) overlaid with topographical map (grey scale) of a hematite film deposited on Si wafer in (a) the as-deposited state, and (b) after annealing treatment at 500° C for 2 h.[139]

1.7.3. Transmission electron microscopy

Although both SEM and transmission electron microscopy (TEM) are electron microscopy working under high vacuum, compared to SEM, TEM has lots of difference in the aspects of imaging principle, samples preparation, main functions, magnification times, among others.

Firstly, TEM is a technique using a transmitted electrons beam through a sample to finish the image collection. In 1931, Max Knoll and Ernst Ruska invented the first TEM, providing a huge milestone for the development of TEM.[141] When the electrons beam is transmitted through the sample, the interaction between the electrons and

sample can form an image. Then the image is enlarged and focused on an imaging device.

Secondly, sample preparation for TEM can be a much more complex and cumbersome procedure.[142] Based on the imaging principle of TEM, the sample is required to be ultrathin for the tested position (less than 100 nm thick, even less than 30 nm for high resolution TEM). Therefore, some materials with small enough dimensions (i.g. nanotubes, quantum dots, small organisms, powdered substances) are able to be rapidly deposited with the diluted suspensions on support grids. In the field of PEC water splitting, lots of the reported photoelectrodes are layered structure, which have to be cut into very small dimensions for TEM analysis. So far, different methods have been explored for the samples preparation. Mechanical polishing is one method used to prepare samples with the help of many small machines, and even ion milling is required to acquire final stage thinning. In recent years, with the develop of the technology, the samples are usually prepared by focused ion beam (FIB) technique, which need critical operation processes but short time.

Thirdly, TEM usually is operated under large acceleration voltage from 60 kV to 300 kV, and is capable of imaging at a pretty wide magnification range, the maximum even up to 50 million times with the resolution below 50 pm.[143] Relatively, the maximum field of view in TEM will be limited, extremely smaller compared to SEM. That is to say, TEM technique enables to capture more fine details, even as small as a single atom, which determines its pivotal role in the study of materials science, chemistry and biology. Therefore, the requirement for operating the TEM machine to obtain high quality images is much stricter and more complex, meaning that more operation skills and practice are necessary, as well as the cost. For example, as shown in Figure 1.22, in nano scale TEM can provide more details about the material.[144] Under low magnification, the nanobelts structure was shown with a high dispersion and smooth surface. Under very high magnification, the lattice fringe with space and structure can be clearly observed. Moreover, the selected area electron diffraction (SAED) also plays an important role in detecting the single crystalline and crystal facet of TiO_2.

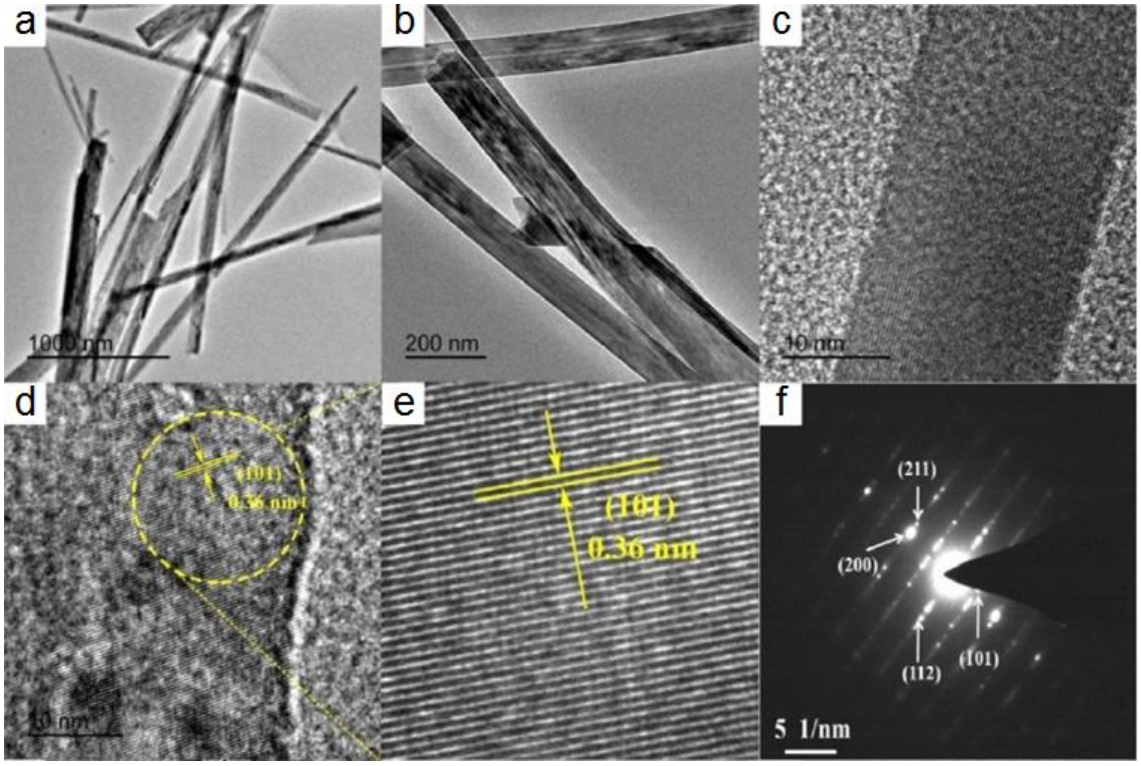

Figure 1.22 (a-c) TEM images of TiO_2 nanobelts with different magnifications, (d-e) high resolution TEM images of TiO_2 nanobelts, and (f) SAED pattern of TiO_2 nanobelts.[144]

In addition, scanning transmission electron microscope (STEM) also has a very significant role in analyzing the materials, which is the combination of SEM and TEM. As the technology advances, when equipped with scanning coils and suitable detectors, TEM can be switched into STEM mode by adding a system that rasters a convergent beam crossing the sample to form an image. Thanks to the rastering of the beam crossing the sample, STEM becomes a proper tool for analytical techniques. Similar to SEM, STEM also can be combined with EDX to obtain the chemical composition and elemental mapping of the samples.[145] For example, by combining cross section STEM and EDX, Alqahtani et al. reported the elements distribution by the elemental mappings, clearly showing the deposited TiO_2 layer with well-defined amorphous structure on GaP surface (Figure 1.23).[146]

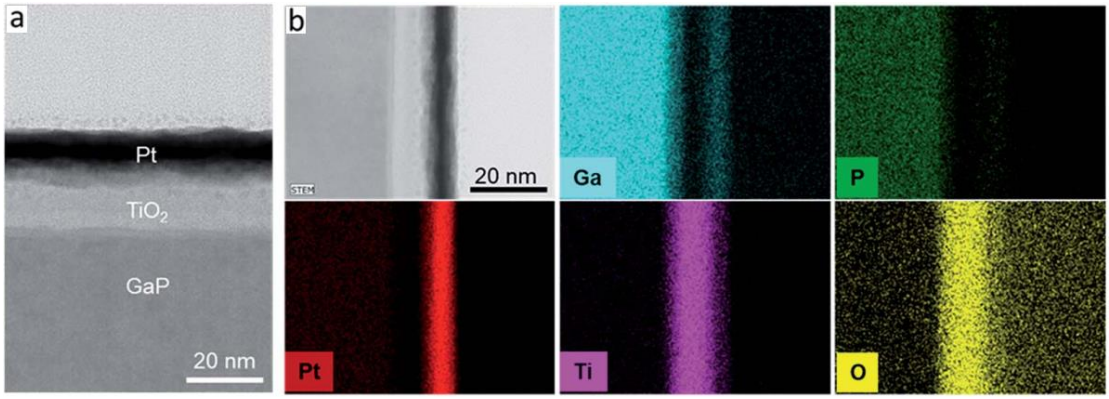

Figure 1.23 Structural and chemical profiling of the Pt/TiO_2/GaP/Si photocathode. (a) Cross-sectional STEM image of Pt/TiO_2/GaP/Si photocathode. (b) EDX mapping shows the individual layer thickness related to the Ti, O, Ga, P and Pt elements.[146]

Moreover, STEM could be able to work combining with Electron Energy Loss Spectroscope (EELS), which is said to be a complement to EDX. EDX is quite easy to perform and is expert in identifying the atomic composition of materials, and it is particularly sensitive to the heavier elements. In terms of EELS, when the electron beam goes through the specimen, some electrons in the beam interact with electrons in the specimen via inelastic scattering to form energy loss. EELS is always a much more difficult technique, while in principle it enables to get more information about the samples, such as chemical bonding, atomic composition, surface properties, conduction and valence band electronic properties, among others.[147] The much higher energy resolution (~1 eV or better) plays sufficient roles compared to the low resolution of EDX (about a few tens of eV). EELS is prone to detecting relatively low atomic numbers, where the excitation edges have the trend to be well-defined, sharp and experimentally achievable energy losses (the signal becoming quite faint exceeding an energy loss of ~3 keV). As illustrated in Figure 1.24, using cross section TEM and EELS techniques, Fan et al. confirmed the size of Ni-Mo catalyst, the uniform distribution of catalyst elements, and one successfully fabricated Ni layer with ~10 nm thickness and uniform distribution.[148] Powerfully, EELS shows its strong functions in investigating the insulator layer change during the resistive switching behaviors happen in metal-insulator-metal memristors.[137-138]

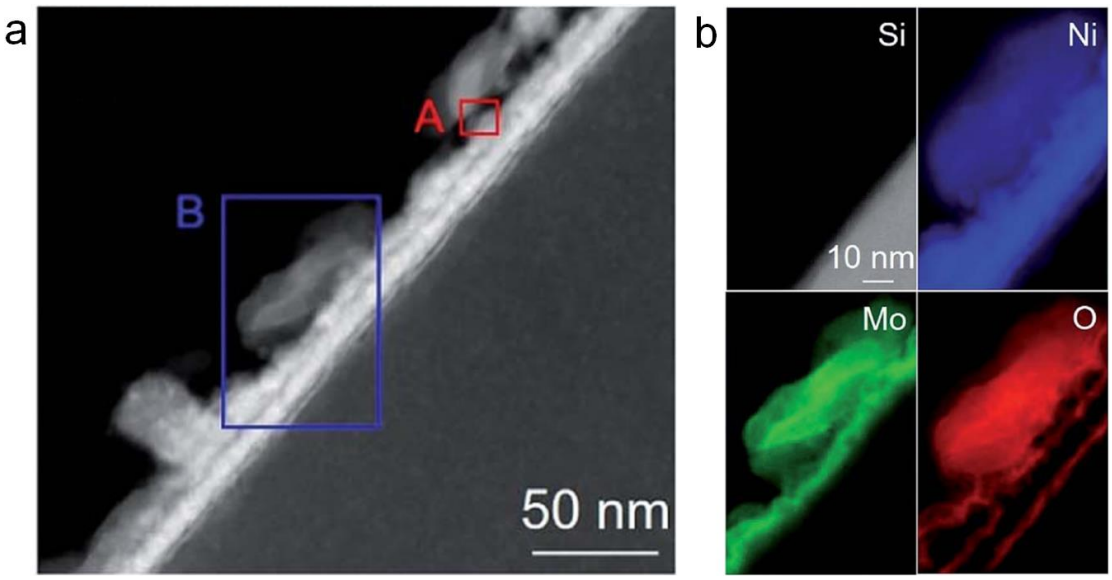

Figure 1.24 Microscopic characterization of the as-prepared Ni-Mo/Ni/n^{++}-Si photoanode. (a) Cross-sectional high-angle annular dark-field imaging (HAADF) STEM image. (b) EELS elemental mapping results for the selected region B in panel (a).[148]

Similarly, in the field of PEC water splitting, the combination of TEM and EELS is an indispensable and powerful tool for analyzing the structure, morphological changes and chemical composition of the photoelectrodes before and after PEC measurements at nano scale. Specially, in this thesis all the results related to TEM and EELS characterizations were performed in CNR-IMM in Catania of Italy. And TEM analyses were characterized in two different ways including plan view and cross section, and their TEM specimens were prepared manually with the help of some small machines and tools, which is very distinct from FIB technique. In term of cross-sectional TEM, the following is the sample preparation processes: 1) Prepare the sample into a sandwiched structure using two pieces of Si as supporting and protective substrates; 2) Paste the prepared sandwich-structure sample (Si-sample-Si) on glass substrate and along the cross section cut one piece with a wide of ~1 mm using a low speed diamond wheel saw (model 650); 3) Paste the cut sample on the steel cylinder and make a round furrow on the cross section with a depth of 200 μm using a ultrasonic disc cutter (model 601) with silicon carbide; 4) Dig a basin inside the furrow which accounts for ~0.75 of the round circle using a dimple grinder (from Gatan, Inc., model 656) with polycrystalline diamond suspension; 5) Polish the opposite side (without furrow) of the

sandwiched sample with a glass cylinder and make the thickness thinner up to ~75 μm using a variable speed grinder/polisher (Buehler Ecomet 3). In this case, the furrow can be observed, and the thickness was calculated by an absolute digimatic indicator (from Mitutoyo). 6) Dig the basin obtained in step 4 until the orange light can be observed from the bottom of the dimple grinder, indicating that the thickness of the sample was 5-10 μm; 7) Separate the prepared round sample from the glass cylinder by immersing in acetone for long time (~2 h); and 8) Carry out ion milling with Ar ions under the voltage of 2-5 keV to produce a respected hole through the surface of the sample using a precision ion polishing system (from Gatan, Inc., model 691). In this case, the edge of the hole is ~50 nm, where it's possible to do TEM analysis. Importantly, the areas to do TEM should be protected by glue, which are not destroyed by ions. Overall, during the TEM specimen preparation, an optical microscope is available all the time for observing the sample.

Compared to cross-sectional TEM, the TEM specimen preparation for plan view analysis is easier. The detailed processes is that 1) Paste the sample on one Si substrate and put a thin glue layer on the surface of the sample for protection (this glue can't be removed by acetone); 2) Along the cross section cut one piece of Sample-Si with a wide of 1 cm and paste it on the steel cylinder; 3) Make a round furrow on the surface of the sample with a depth of 200 μm; 4) Polish the back side (without furrow) of the Sample-Si with a glass cylinder and make the thickness thinner up to ~75 μm (The furrow can be observed.); 5) Dig one basin in the middle of the furrow until the orange light can be observed from the bottom of the dimple grinder, indicating that the thickness of the sample was 5-10 μm; 6) Separate the prepared round sample from the glass cylinder by immersing in acetone for long time (~2 h); and 7) Do ion milling in the middle of the basin to get very thin areas for plan view TEM analysis.

1.7.4. X-ray photoelectron spectroscopy

X-ray photoelectron spectroscopy (XPS) is a useful characterization technique which is surface-sensitive quantitative spectroscopic. It enables to measure the elemental composition in the film and other elements boned to these elements. In 1954, the first XPS spectrum with high energy resolution of cleaved sodium chloride was performed by Siegbahn et al., which laid the strong foundation for the extensive application of XPS.[149] As the name implies, when a beam of X-rays are used to

irradiate a material, XPS simultaneously measures the kinetic energy and the number of electrons escaping from the surface of the analyzed material to obtain the spectrum. Although XPS measurements need to be operated under ultra-high vacuum environment, it has many functions, including the elemental composition located on the surface (usually 0 to 10 nm), the contaminated elements on the sample surface, electronic or chemical state of each element at the surface, empirical formula of pure materials, and the thickness of ultra-thin layers, among others.

In the field of PEC water splitting, performing the chemical composition of the photoelectrodes is an essential work to better understand the PEC performance. Compared to EDX, XPS has the advantages of quantitative analysis and chemical state for the elements in the material. Although the resolution is lower than that of EELS technique, XPS still plays a significant effect on observing the chemical composition changes before and after PEC tests, which has promoted many excellent works.[51,61,75,148,150] In my experiments, to perform the XPS measurement, it's very important to keep the analyzed sample clean, dry and stable. After determining the height where more signals can be collected, two types of XPS spectra will be done. First, under high pass energy, the XPS full spectrum (from 0 - 1200 eV) can be obtained to give a rough understanding about the sample composition. Then under low pass energy, the narrow spectra related to each analyzed element were recorded under lower scan speed and more scan cycles, which can gather more signals beneficial to detailed information on the sample. After converting kinetic energies to binding energy, in the XPS spectra that is plot of number of electrons versus binding energy of the detected electrons, the chemical composition analyses can be confirmed according to the position of peaks. As shown in Figure 1.25, by combining XPS depth profiling characterization with ion etching, Digdaya et al. clearly revealed that the metallic Ni film partially transferred into NiOx and $Ni(OH)_2$ at after 18 h PEC tests in alkaline electrolyte.[51]

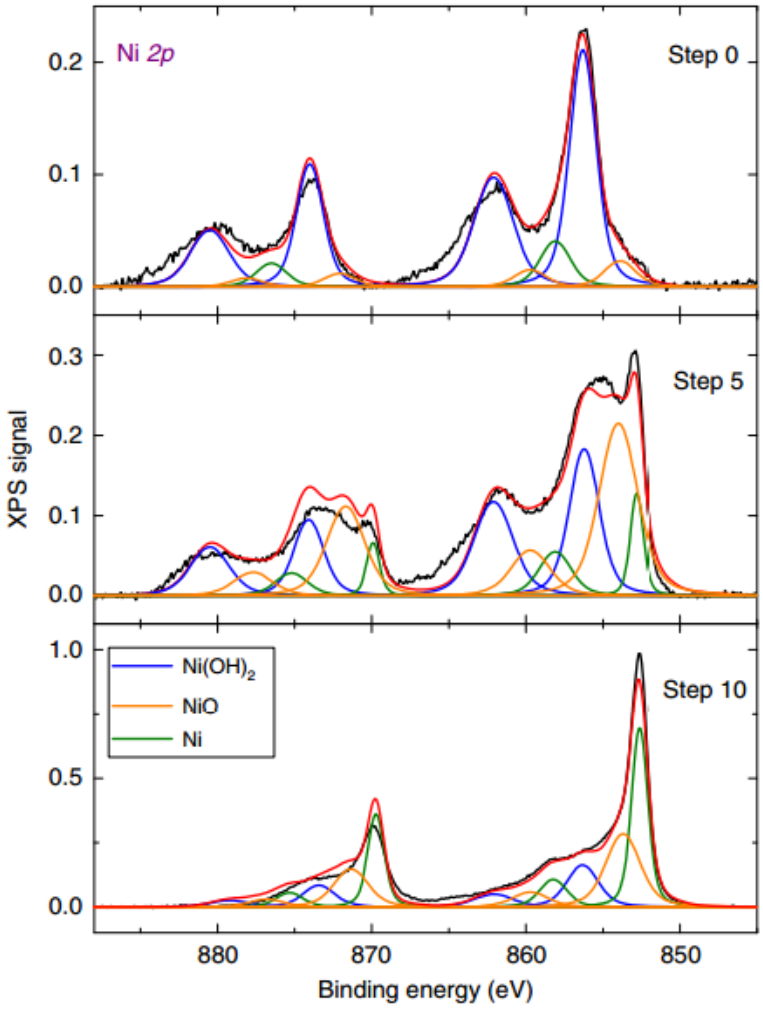

Figure 1.25 XPS spectra of Ni element on Ni/Pt/Al_2O_3/SiOx/n-Si photoanode after 18 h ageing procedure. Ni 2p signals as a function of etching step—step 0 (no etching), step 5 and step 10 (~3 nm etched depth)—showing variation of Ni phases. The electrode was etched using ion beam with an average etching rate of ~ 3 Å per step.[51]

1.8. Main Contribution of this PhD thesis

1.8.1. Objectives of this PhD thesis

The main goal of this thesis is to design, fabricate and measure different nanostructured coatings for semiconducting photoelectrodes (working immersed in electrolytes) for PEC water splitting, with the main goal of enhancing their efficiency for clean hydrogen fuel generation. This task can be divided in three objectives. The first one is to deeply study the ageing mechanisms of highly active and stable

nickel-coated n-type silicon photoanodes for water splitting. To do so, the ultrathin Ni layers have been analyzed by combining TEM and EELS technologies at the atomic and nano scale before and after long-term PEC characterizations for the first time. The second one is to investigate the effect of different alkaline electrolytes for OER by characterizing the activity and stability of Ni coated n-Si photoanodes. And the third one is to study the effect of noble metal nanoparticles (Au or Pt) deposited on n-3C-SiC/p-Si for hydrogen evolution reaction in strong alkaline electrolyte.

1.8.2. Key findings

In **Chapter 2** of this PhD thesis I studied the ageing mechanisms of ultrathin nickel films (with different thicknesses) coated n-Si photoanodes working in 1.0 M KOH electrolyte (pH = 14). To understand the morphology and chemical composition of the catalyst/protect Ni layer, before and after the PEC tests, we characterized the water-splitting solar cells combining scanning electron microscopy (SEM), atomic force microscopy (AFM), and cross-sectional transmission electron microscopy (X-TEM) coupled with electron energy lose spectroscopy (EELS), the latter having sub-nanometer resolution. I show that the ageing mechanisms of the photoanodes are strongly related to the thickness of the catalyst coating, and traditional characterization tools with low spatial resolution could ignore some essential degradation phenomena in the field of water splitting.

After understanding the degradation mechanisms of Ni-based Si photoanodes, in 1.0 M KOH electrolytes (pH = 14), in the second part I analyzed the PEC performance in three different alkaline electrolytes (pH = 9.5, pH = 12.5 and pH = 14) for OER taking 5 nm Ni-based n-Si photoanodes as an example. **Chapter 3** shows that in the mixture electrolyte of KOH and LiOH (pH = 12.5), the photoelectrodes show best OER performance considering both the activity and stability. This indicates that tuning the chemical composition of the electrolyte is an inexpensive and effective approach to improve the performance of Ni-coated n-Si photoanodes for PEC water splitting.

In **Chapter 4**, I studied 3C-SiC/p-Si based photocathodes for PEC water splitting in 1.0 M KOH electrolyte, and introduced noble metal nanoparticles on the surface of the SiC to improve the performance. I demonstrated that 3C-SiC covered on Si could produce high photocurrent and long stability since Si has very good ability to absorb visible light and SiC has excellent chemical resistance. Besides, after integrating Au or

Pt nanoparticles on the surface of 3C-SiC/Si, photocurrent enhancement and low onset potential can be observed due to the plasmonic and catalystic effects, respectively.

1.8.3. Thesis Outline

This thesis is divided in five chapters: Chapter 1 presents the dissertation summary, which introduces the most relevant aspects of this PhD thesis. Chapter 2 investigates the ageing mechanisms of different thicknesses of nickel based n-type silicon photoanodes for PEC water splitting in strong alkaline electrolyte. On the basis of the obtained results in Chapter 2, Chapter 3 introduces one advanced electrolyte consisting of KOH and LiOH to enhance the PEC performance of the Ni/SiOx/n-Si photoanodes by comparing three different pH electrolytes. Chapter 4 describes n-type 3C-SiC deposited on p-Si based photocathodes for PEC water splitting in strong alkaline electrolyte. I observe that the performance of the photocathodes could be enhanced when noble metal nanoparticles (e.g. Au or Pt) were deposited on the surface of the 3C-SiC layer due to their plasmonic and catalytic properties. Finally, Chapter 5 summarizes the main results of this thesis, conclusions and perspectives.

1.8.4. List of publications

The list of articles shown below only includes the publications which shall be considered for evaluation of this PhD dissertation, although during my PhD I have published many other research articles. A reproduction of each publication can be accessed by the information indicated below. A complete list of my publication (updated on June 10th 2020) is included in my scientific curriculum vitae (Appendix A).

Article 1 **Tingting Han**, Yuanyuan Shi, Xiaoxue Song, Antonio Mio, Luca Valenti, Fei Hui, Stefania Privitera, Salvatore Lombardo, Mario Lanza, Ageing mechanisms of highly active and stable nickel-coated silicon photoanodes for water splitting, **Journal of Materials Chemistry A.**, 4 (21): 8053-8060 (2016). Selected as back cover article.

**Contribution: Performing the experiments, including samples fabrication by electron beam evaporation and thermal evaporation, Photoelectrochemical (PEC) analyses for the photoanodes, samples characterizations by scanning elelctrn microscopy (SEM), atomic force microscopy (AFM), X-ray photoelectron spectroscope (XPS) and probe station, evaluation of the results and writing the main parts of the manuscript.*

Article 2 **Tingting Han**, Yuanyuan Shi, Zhouchangwan Yu, Byungha Shin, and Mario Lanza, Potassium hydroxide mixed with lithium hydroxide: an advanced electrolyte for oxygen evolution reaction, **Solar RRL**, 1900195 (2019).

**Contribution: Performing the experiments, including samples fabrication by magnetron sputtering, PEC characterization for the prepared photoanodes, samples characterizations by SEM, AFM and XPS, evaluation of the results and writing the manuscript.*

Article 3 **Tingting Han**, Stefania Privitera, Gabriela Milazzo, Corrado Bongiorno, Salvatore Di Franco, Francesco La Via, Xiaoxue Song, Yuanyuan Shi, Mario Lanza, Savatore Lombardo. Photo-electrochemical water splitting in silicon based photocathodes enhanced by plasmonic/catalytic nanostructures, **Materials Science and Engineering: B.**, 225: 128-133 (2017).

**Contribution: Performing the PEC characterization and external quantum efficiency (EQE) measurement for the prepared photocathodes, preparing the samples for transmission electron microscopy (TEM) characterization and analyzing the results.*

These articles have been developed in collaboration with the Institute of Microelectronics and Microsystems of the Italian National Research Council in Catania (CNR-IMM, Italy) and Soochow University (China). To do this work, I travelled one year to CNR-IMM in Catania, where I worked in the research group led by Dr.

Salvatore Lombardo. For my stay at CNR-IMM, I won a fellowship from the Program for Training and Research in Italian Laboratories (TRIL), which is funded by the Abdus Salam International Centre for Theoretical Physics (ICTP).

Chapter 2:
Ageing mechanisms of Ni-coated n-Si photoanodes for photoelectrochemical water splitting

2.1. Introduction

Due to the low cost and good ability to absorb light, silicon is the preferred semiconductor photoelectrode for PEC water splitting, but the amounts of hydrogen and oxygen produced when using Si (as well as any other semiconductor material) are, unfortunately, very modest, and the chemical reactions decay after a few minutes due to surface corrosion. To overcome these problems, the most advanced water-splitting cells use a catalytic and protective coating deposited directly on the semiconductor surface. Several metal-based catalysts, including Ru,[151] Ni,[49] NiO_X,[71,152] Ir,[59] Cu,[153] CuO_X,[154] MnO_X[78] and Co[155] have been demonstrated to enhance the activity of semiconductor photoelectrodes for water splitting, achieving current densities of up to tens of mA/cm^2.[71] While such cell activity amply exceeds the requirements of this technology, stability remains a major concern. Among all catalysts used, there is a consensus that nickel-based oxides and compounds are the most cost-effective and durable solution.[49,52,70-71,152,156-157] Kenney et al. observed that silicon photoanodes coated with ultrathin (2 nm) layers of nickel can generate current densities of 10 mA/cm^2 for more than 80 hours.[49] Mei et al. achieved stable water splitting for 300 h using p^+n silicon photoanodes coated with 50 nm thick Fe-treated NiO films,[157] and Sun et al. reported lifetimes of above 1200 h using generally even thicker, i.e. 35–160 nm thick, NiO_X films on np^+ silicon.[71] It is worth noting that the use of thick coatings reduces the transmittance of light to the silicon, leading to larger onset potentials and smaller saturation currents.[49] Moreover, the fabrication of buried np^+-Si junctions involves additional processing steps during the manufacturing process.

Despite the long lifetimes reported, the ageing mechanisms that produce a decay in activity and device failures in water splitting solar cells are still not understood, and one

of the main important reasons for this lack of understanding is the lack of in-depth studies of the reliability of the cells at the nano and atomic scales. Scanning electron microscopy (SEM), despite being a widely used technique, is unable to provide clear-cut information about the samples, and it has been mainly used to reveal the thickness of the coatings[49,71,157] and to provide an approximation of surface roughness.[52] Surface roughness has been quantitatively analyzed by using atomic force microscopy (AFM),[70-71,156] but a thorough characterization as a function of testing time has not been reported, hence precluding the detection of degradation trends and ageing mechanisms. X-ray photoelectron spectroscopy (XPS),[61,75.77] energy-dispersive X-ray spectroscopy (EDX)[52,157] and Auger electron spectroscopy (AES)[49] have been widely used for chemical characterizations, but the lateral resolution levels of these techniques are only 10 mm, 1 mm and 20 nm, respectively, so these techniques can mask local phenomena and defects produced during photoelectrochemical (PEC) processes. Few groups have reported the use of cross-sectional transmission electron microscopy (X-TEM) to obtain information at the atomic level,[52,59-60,70,77] but only images of fresh samples were reported (to indicate the thickness of the layers).

In this Chapter, we present the fabrication of nickel-coated n-type silicon photoanodes with long lifetimes of more than 260 hours, and we exhaustively analyzed their ageing mechanisms at the nano and atomic scales. Several characterization tools traditionally used in the field of water-splitting solar cells, such as SEM, XPS and AFM, were combined with X-TEM, and we introduced for the first time the use of electron energy loss spectroscopy (EELS) to the study of water-splitting solar cells. The higher resolution of this technique allowed us observing some features that are blind for widely used XPS technique. Our results demonstrated that the ageing of the photoanodes is strongly linked to the thickness of the catalyst coating, and we observed remarkable differences in the surface roughness, stack homogeneity, conduction mechanisms and formation of holes.

2.2. Experimental section

2.2.1. Fabrication of electrodes

As-received phosphorous-doped (100) n-type silicon wafers (from Prolog Semicor)

with a resistivity of 0.3-0.5 ohm·cm were cleaned using a three-step process. First, the wafers were immersed in acetone for ten minutes, then in ethyl alcohol for another ten minutes, and finally in deionized water for an additional ten minutes. For all cleaning steps, an ultrasonic bath was used. The samples were then dried with a N_2 gun. As a reference, one n-Si sample was immersed in water-diluted hydrofluoric acid (the volume ratio of HF and H_2O is 1 to 5) for ten seconds to remove the native oxide. Once the n-Si wafers were cleaned, a thin layer of nickel (with a thickness of 2 nm, 5 nm or 10 nm) was evaporated onto their top surface. Onto the backside of the wafers, a 20 nm thick layer of titanium was evaporated to form an ohmic contact. A PVD75 electron beam evaporator from Kurt J. Lesker Company was used under the electric field voltage of 8 kV at deposition rates of ~0.15 Å/s and ~0.45 Å/s for the Ni and Ti layers, respectively. Copper tape was used to affix the back side of Ni/native SiO_X/n-Si/Ti samples connecting to the electrochemical workstation for electrochemical experiments in the dark or under illumination.

2.2.2. Electrochemical characterization

The activity and stability of the Ni/SiO_X/n-Si photoelectrodes were measured for PEC water splitting by using the system shown in Figure 2.1. The electrodes were tested in a square container (made of Teflon material) with two circular apertures, as shown in Figure 2.2, with sizes of 0.5 cm^2 and 2.0 cm^2, located at opposite faces. The small aperture was sealed by the electrode using a rubber ring and a back tap fixed by four screws. The bigger aperture was sealed using a piece of glass, through which light was transmitted to the surface of the electrode. The light flux was generated using a 150 W xenon lamp from Newport Corporation, and the electrodes were irradiated using a light power density of 50 mW/cm^2. This value was confirmed by using an optical power meter from Newport Corporation (model 1918-R). A saturated calomel electrode (SCE, saturated potassium chloride (KCl)) was used as the reference electrode, and a stainless steel electrode worked as the counter electrode. Electrochemical experiments were performed in a three-electrode system controlled by a CHI 660E potentiostat (CH Instrument, Inc). Before the experiments, the container was filled with an electrolyte consisting of 1.0 M KOH (pH = 14), prepared by dissolving 5.6 g KOH flakes (from Sinopharm Chemical Reagent) in 100 mL deionized water. Before every measurement, bubbles were removed from the aperture using a plastic pipette. Since the generation of

bubbles (resulting from H_2 or O_2 gas) decreased the amount of electrolyte in the container, more KOH electrolyte was added when acquiring I–t curves for long times. Before and after the electrochemical tests, the electrical resistance of the system was recorded. During the experiments, cyclic voltammetry (CV), linear sweep voltammetry (LSV) and amperometric I–t curves were acquired under the condition of no iR compensation. CV and LSV data were collected with the scan rates of 100 mV/s and 10 mV/s, respectively. Furthermore, SCE was converted to RHE using the following relationship: E(RHE) = E(SCE) + 0.244 V + 0.059*pH

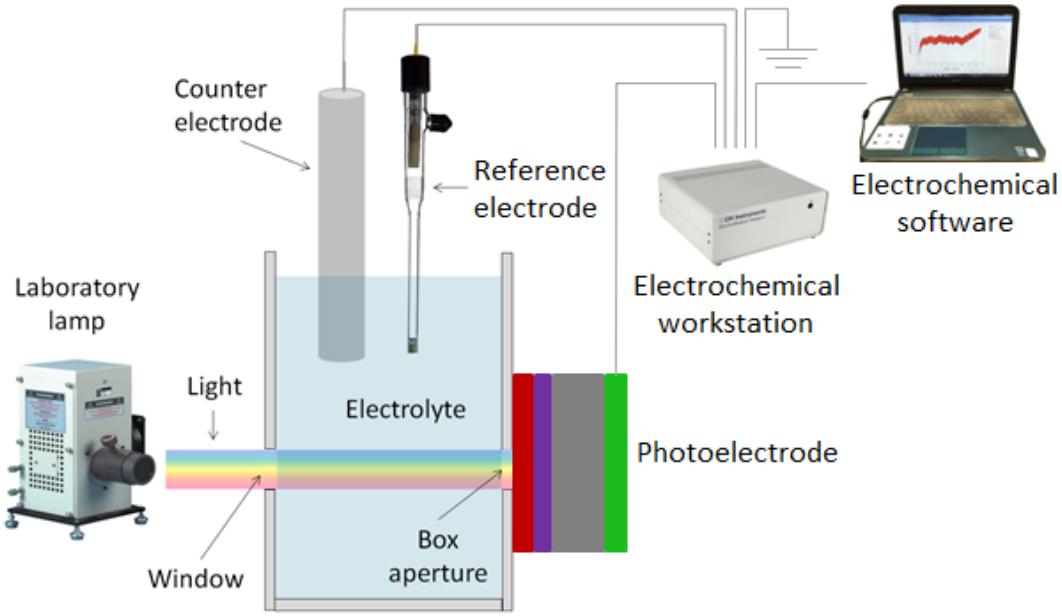

Figure 2.1 Overall system used for PEC characterization of water splitting solar cells

Figure 2.2 Custom designed Teflon box for electrodes to carry out the PEC tests.

2.2.3. Characterization of materials

After electrochemical characterization, the photoanodes were rinsed with water for ten seconds, washed again in deionized water for three minutes and dried with a N_2 gas gun. The morphological changes induced by the electrochemical tests were analyzed with two different scanning electron microscopes (SEMs), the FEI Quanta 200FEG and the Zeiss SUPRA55, and also by means of atomic force microscopy (AFM), using the MultiMode V from Veeco working in tapping mode and using NanoWorld Pointprobe tips (model NCH, item no. 78131F6L965). The chemical composition of the samples was determined by carrying out X-ray photoelectron spectroscopy (XPS) experiments, using a KRATOS AXIS Ultra DLD spectrometer from Shimadzu. In addition, atomic-scale morphological and chemical information was obtained by combining cross-sectional transmission electron microscopy (X-TEM) with the electron energy loss spectroscopy (EELS) acquired in scanning TEM mode (STEM), using a JEOL JEM 2010F electron microscope with a 200 kV accelerating voltage. The samples analyzed by X-TEM were protected with a 50 nm thick layer of Au right after the PEC experiments, to avoid the effects of the environment. A Leica Microsystems (DM4000M) fluorescence optical microscope was used to analyze the surfaces of the samples at the microscale. The conductivities of fresh and tested photoanodes were determined at both the nanoscale and the device level. Electrical conductivity values of the photoanodes were determined using a Bruker Multimode VIII conductive AFM (CAFM) provided with Pt-varnished silicon tips from Nano World (model PPP-CONTPt, item no. 80064F11L1115). In order to characterize the photocurrents through the photoanodes, current maps were collected under illumination (provided by the built-in laser of the CAFM) and without applying any external bias. For device-level characterization, metallic electrodes made of a 50 nm thick layer of Au were evaporated directly by thermal evaporation (Kurt J. Lesker, model: NANO36) onto the surfaces of the Ni-based n-Si photoanodes. And a laser-patterned shadow mask from Tecan (UK) was used to pattern the Au squared electrodes with different sizes (i.g. 100 μm ×100 μm, 50 μm × 50 μm and 25 μm × 25 μm). Then the devices were characterized by collecting current–voltage (I–V) curves using a probe station (Cascade, model: M150) and a semiconductor parameter analyzer (Keithley, model: 4200-SCS). Note that the morphological characterizations of the samples by AFM, SEM, TEM and EELS were performed *ex situ*. While the surfaces of the samples in operation (i.e. in contact with

the electrolyte) and during ex situ characterization (i.e., in air or vacuum) may differ, permanent damage induced by the PEC tests has been previously demonstrated.[49,59,78]

2.3. Results and discussion

2.3.1. PEC performance of Ni/SiO_X/n-Si/Ti photoanodes

By using electron beam evaporation, n-type silicon wafers (with their native oxide) were coated with nickel layers of different thicknesses (2 nm, 5 nm and 10 nm), and 20 nm Ti layer was deposited on the backside to form an ohmic contact. The resulting photoanodes (as shown in Figure 2.3) were tested under KOH electrolyte (pH = 14) in a three-electrode system, using a saturated calomel reference electrode (SCE) and a stainless steel counter electrode. Sequences of cyclic voltammograms (CVs) and amperometric current–time (I–t) curves were acquired under an illumination of 50 mW/cm^2 and in the dark. Figure 2.4a shows a schematic of the setup used to characterize the samples, and Figure 2.4b shows an X-TEM image of a silicon photoanode coated with a 5 nm thick layer of nickel, confirming that electron beam evaporation is an excellent method to deposit ultrathin metallic layers with low thickness fluctuations.

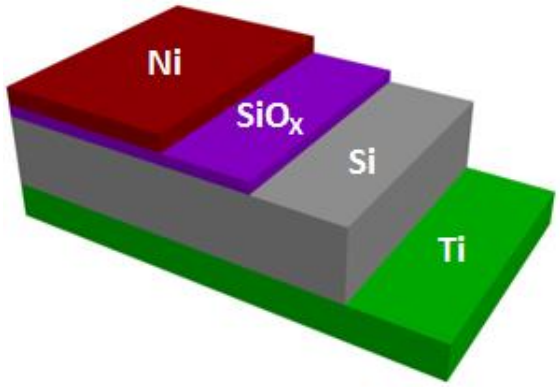

Figure 2.3 Structure of prepared photoanodes by electron beam evaporation.

Figure 2.4c shows typical CVs recorded for the three types of Ni/SiO_X/n-Si photoanodes. The sample with a 2 nm thick coating of Ni yielded the lowest onset potential (80 mV vs. SCE) and the largest saturation current (10 mA/cm^2 under 50

mW/cm^2), due to the greater transmittance of light into the silicon.[49,60] Moreover, one chopped linear sweep voltammetry (LSV) shown in Figure 2.5 was collected, confirming that the light plays an important role on the activity for water splitting. As a reference, a 2 nm thick Ni layer was also deposited on a native oxide-free n-Si photoanode (after etching the native SiO_X with a water-diluted HF solution). As seen in Figure 2.6 the current of this photoanode decreased after each CV scan, which indicates that the native SiO_X was necessary for ensuring the good stability of solar cells. It has been suggested that the SiO_X layer may work as an adhesive to retain the Ni material on the surface of the photoelectrodes.[49] Short-duration I–t curves at the constant potential of 1.8 V vs. SCE (Figure 2.4d) revealed stable currents during the first two hours for all samples, showing the characteristic sawtooth shape related to oxygen bubble formation during the OER (see Figure 2.7).

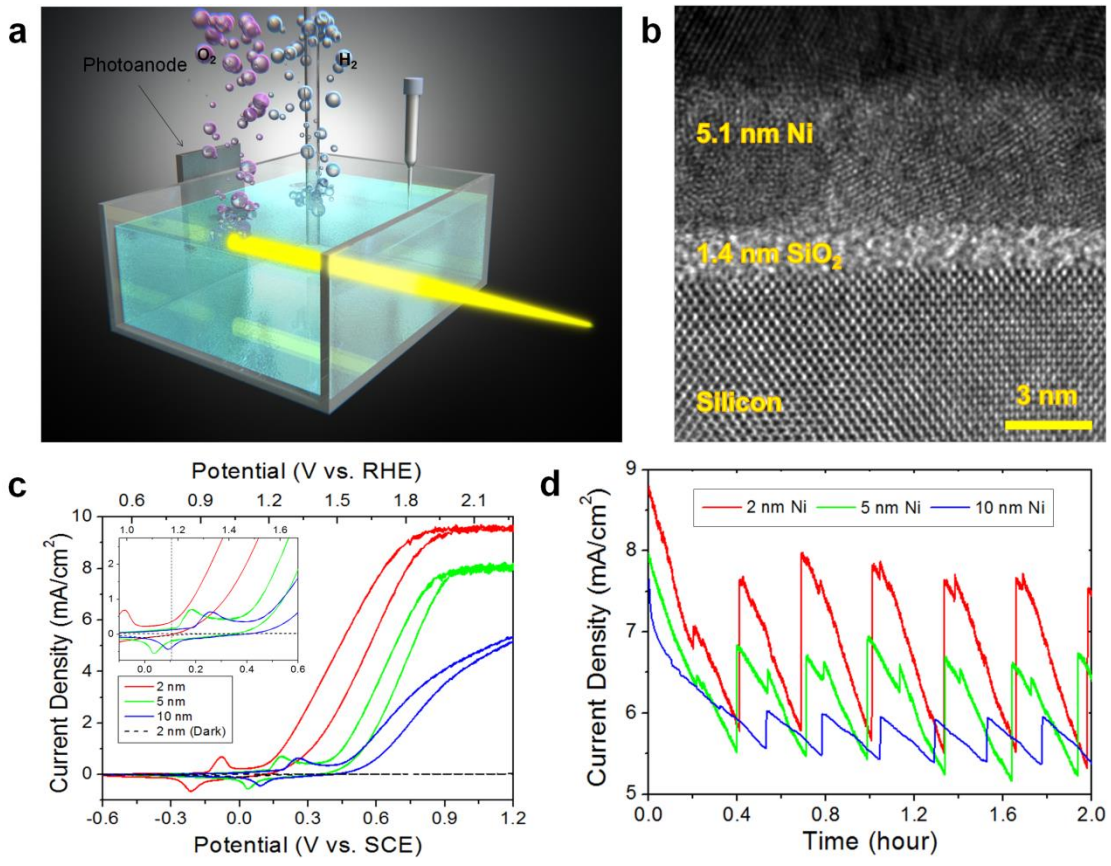

Figure 2.4 Fabrication and characterization of Ni/SiO_X/n-Si/Ti photoanodes. (a) 3D schematic of the setup used to characterize the photoanodes. (b) Cross-sectional TEM image of a fresh 5 nm Ni/SiO_X/n-Si/Ti photoanode. (c) Typical cyclic voltammograms (CV) measured for the Ni/SiO_X/n-Si/Ti photoanodes with nickel thicknesses of 2 nm, 5

nm and 10 nm, tested in 1.0 M KOH under illumination of 50 mW/cm^2. (d) Short-duration amperometric I–t curves measured at a constant potential of 1.8 V vs. SCE for the three Ni/SiO_X/n-Si/Ti photoanodes with different Ni thicknesses.

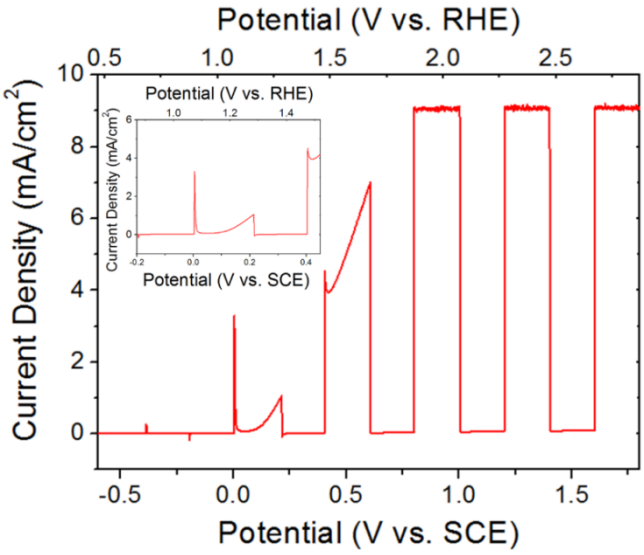

Figure 2.5 Linear sweep voltammetry (LSV) recorded for a 2 nm Ni coated silicon photoanode under an illumination of 50 mW/cm^2. In the LSV, the light is being chopped: the obvious current only was obtained under illumination, and no OER current was observed for the photoanodes under the absence of illumination. Besides, the inset image shows the magnified view of the collected LSV from -0.2 V vs. SCE to 0.45 V vs. SCE.

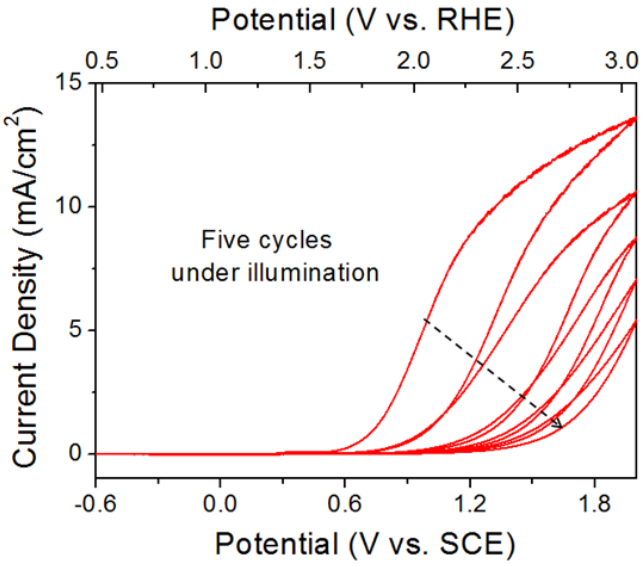

Figure 2.6 Consecutive five cycles CVs recorded for a 2 nm Ni coated silicon

photoanode (without native SiO_X) under an illumination of 50 mW/cm^2. The native SiO_X was etched by HF solution before nickel deposition. The fast decay indicates that SiO_X is beneficial to the stability of the photoanode.

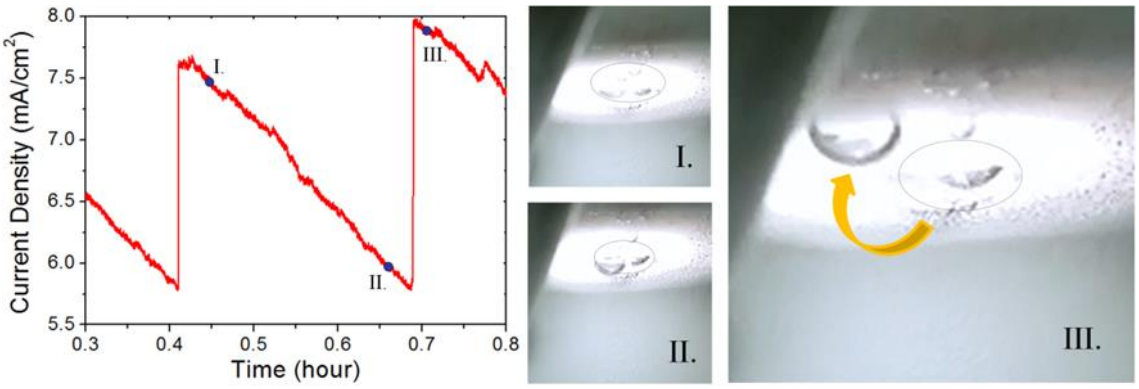

Figure 2.7 Amperometric I-t curve measured at 1.8 V vs. SCE for the 2 nm Ni photoanode under an illumination of 50 mW/cm^2. The I-t curve clearly displays the typical sawtooth shape related to the formation process of a bubble. On the right, the digital camera pictures of the detachment of a bubble in the points I, II and III were highlighted in the I-t curve.

2.3.2. Ageing mechanisms of 5 nm and 10 nm Ni/SiO_X/n-Si/Ti photoanodes

The lifetime and ageing mechanisms of the photoanodes were analyzed by carrying out long-duration PEC tests. Figure 2.8a shows representative I–t curves for silicon electrodes coated with 5 nm thick and 10 nm thick nickel layers tested for different periods of time. In total, four photoanodes with 5 nm thick layers of nickel and three photoanodes with 10 nm thick layers of nickel (fabricated in three different batches) were analyzed. The samples with 5 nm thick layer of nickel showed stable currents for 6.5 days, followed by a linear decrease of the current signal with the time. Figure 2.8b and c show SEM and AFM images from these 5 nm thick Ni samples at different testing times. The initial root mean square (RMS) roughness of a fresh 5 nm thick nickel layer was determined to be 0.147 nm (which is very similar to that of bare silicon [158]) and was found to increase with increasing testing time, reaching 2.66 nm after 3.5 days. Interestingly, this morphological change did not degrade the performance of the sample, indicating the formation of a rough layer able to split water. For longer testing times, all the SEM and AFM images revealed the progressive formation of holes, and after 6.5

days, the density of holes became prohibitive and the performance of the cell started to decay linearly. After ten days, the SEM images showed the typical picture of a silicon substrate etched by KOH[49] (see also Figure 2.9) indicating that the nickel coating was completely etched. This analysis was further supported by the observed dramatic increase of the sample roughness in the AFM maps. The chemical composition of this sample was analyzed by means of XPS (Figure 2.10). The spectra collected after different testing times revealed a change in the nickel (Ni^0 to Ni^{3+}) and oxygen peaks, indicating the formation of an effective NiO_X layer after a 24 h PEC test. The XPS data also revealed the presence of potassium element from the electrolyte after the PEC test. The absence of a strong silicon signal indicated the presence of the coating after 24 h PEC test (in agreement with the SEM pictures, which showed corrosion only after 6.5 days).

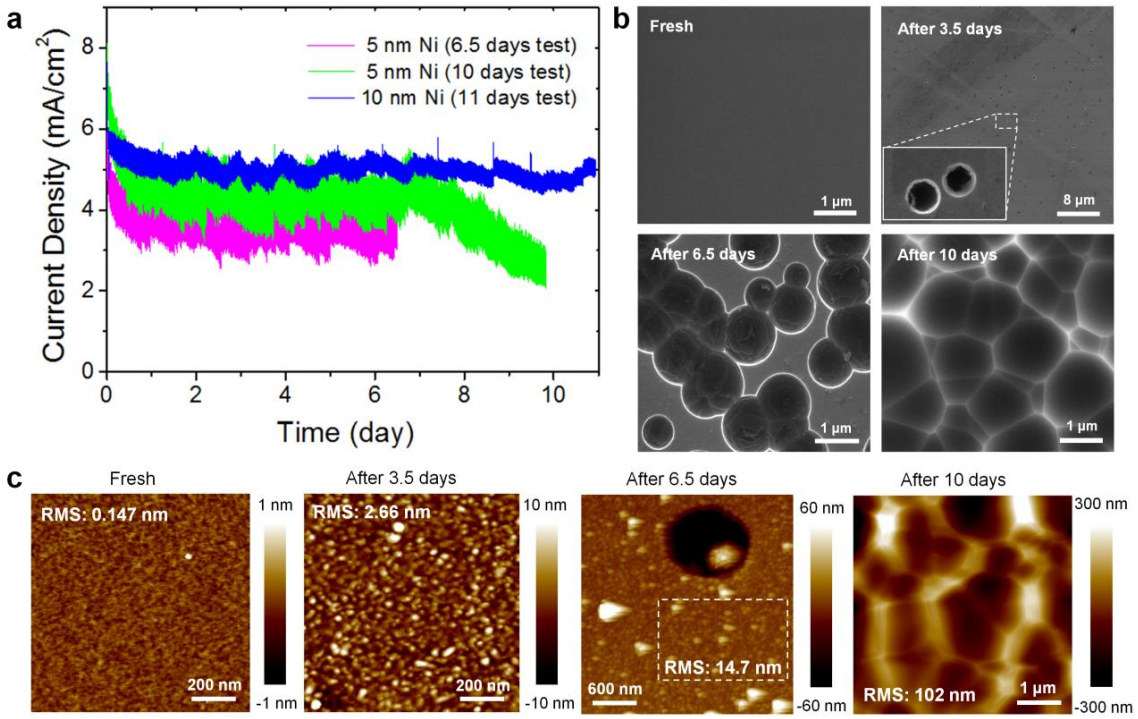

Figure 2.8 Degradation processes of n-type silicon photoanodes coated with 5 nm thick and 10 nm thick Ni layers. (a) Representative amperometric I–t curves measured at the controlled potential of 1.8 V vs. SCE for the 5 nm thick and 10 nm thick Ni/SiOx/n-Si/Ti photoanodes in 1.0 M KOH under an illumination of 50 mW/cm^2. Panels (b) and (c) show the SEM and AFM images collected after different testing times for the silicon photoanodes coated with 5 nm thick layers of Ni. The images of the fresh

samples are also shown as reference. The 5 nm thick sample formed a rough layer that, unlike for the sample coated with the 2 nm thick Ni layer, was able to split water, and the sample only degraded when the density of holes became critical (after 6.5 days).

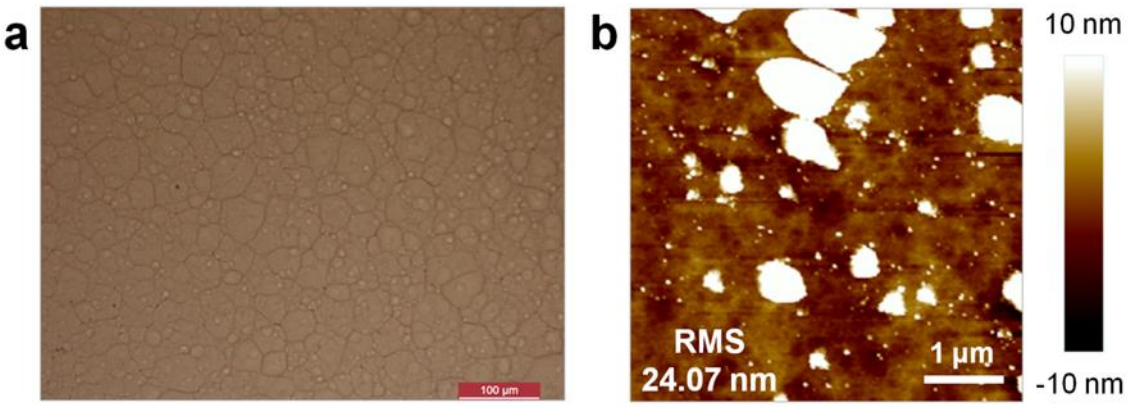

Figure 2.9 (a) Optical microscope and (b) AFM images of a piece of silicon corroded in 1.0 M KOH solution during 5 days, showing a high surface roughness.

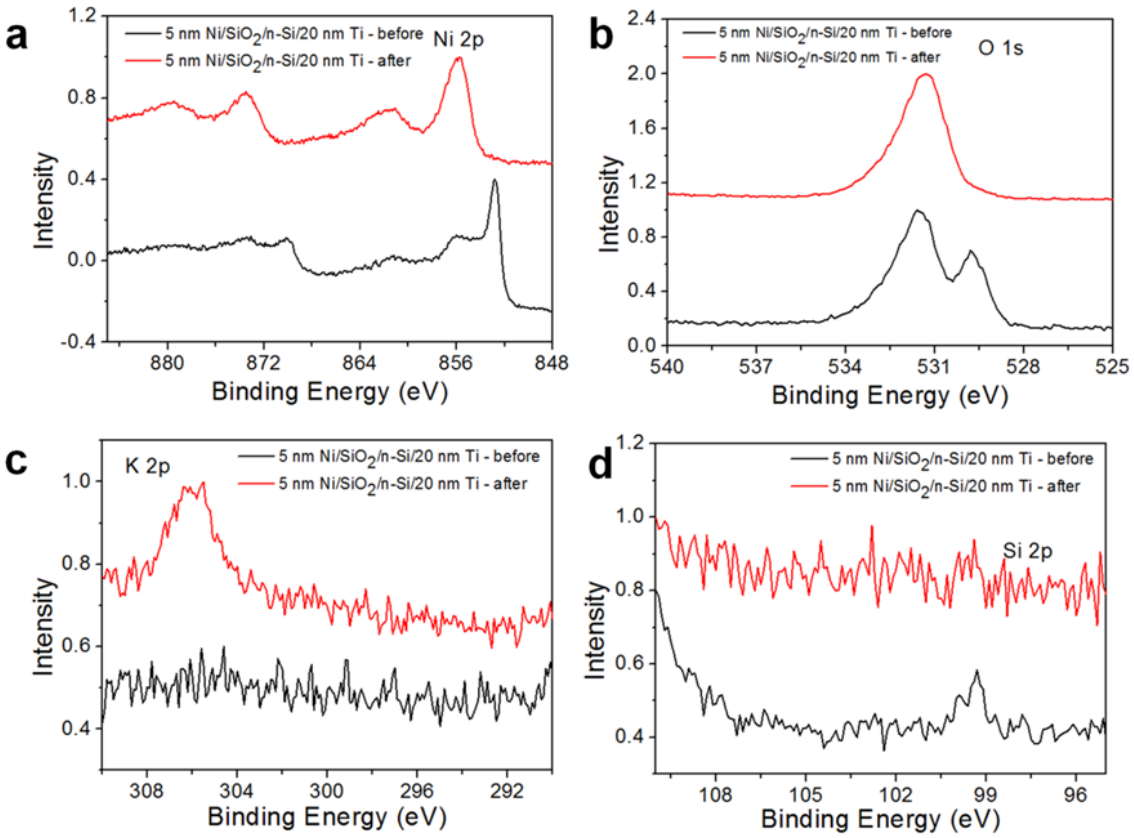

Figure 2.10 XPS spectra for the 5 nm Ni coated n-Si photoanode after 24 h PEC tests

(red line). The spectra of the fresh sample are also showed as reference (black). Panels (a), (b), (c) and (d) are the narrow spectra of Ni 2p, O 1s, K 2p and Si 2p elements, respectively.

The above interpretations were corroborated by the results of X-TEM and EELS experiments, which provided morphological and chemical information at sub-nanometer lateral resolution. Figure 2.11a and b show the X-TEM pictures for the 5 nm thick samples before and after the 24 h PEC test, respectively. The nickel layer in the fresh sample showed a polycrystalline structure, and its thickness was very close to the theoretical value of the evaporator. After the PEC test, the thickness of the coating increased to 6 nm, although nanometer-scale statistical variability of the roughness should not be ignored (see Figure 2.12). The chemical maps obtained with EELS (Figure 2.11c) indicated the Ni coating transformed into NiO_X, which furthermore was very homogeneous. The surface of the sample tested for 24 h (Figure 2.11b) also revealed the formation of a very thin bright layer on top of the NiO_X, which was probably related to the potassium from the 1.0 M KOH electrolyte, as suggested by the XPS data of K 2p element (Figure 2.10c). In any case, the bulk of the NiO_X coating seemed to be free of impurities. The volume expansion in the NiO_X film was expected, since it is known that oxygen evolution is preceded by three-dimensional oxide film formation,[159] on which discharge of OH and/or O takes place. Note that the thickness of the interfacial native SiO_X film typically experienced a small increase of 0.4 nm.

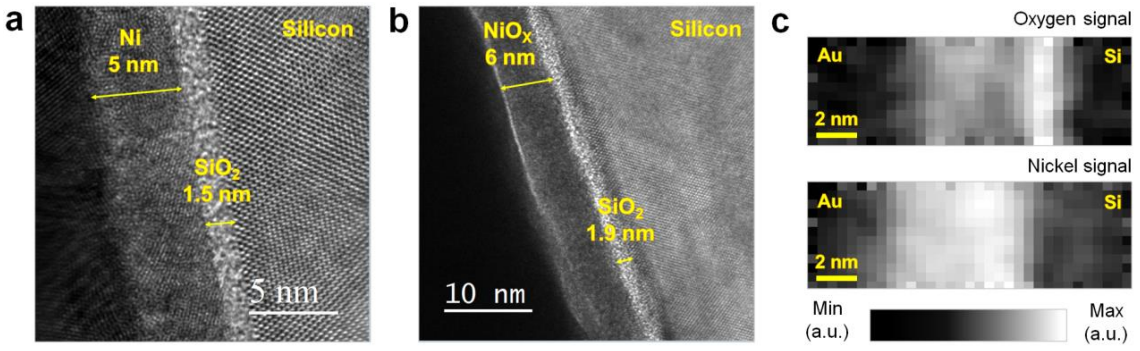

Figure 2.11 Atomic-scale information of fresh and tested silicon n-type photoanodes coated with 5 nm thick layers of Ni. Cross-sectional TEM images for the 5 nm thick Ni/SiO_X/n-Si/Ti samples (a) before and (b) after 24 h of the PEC test. (c) Oxygen and nickel maps collected with EELS on the sample tested for 24 h.

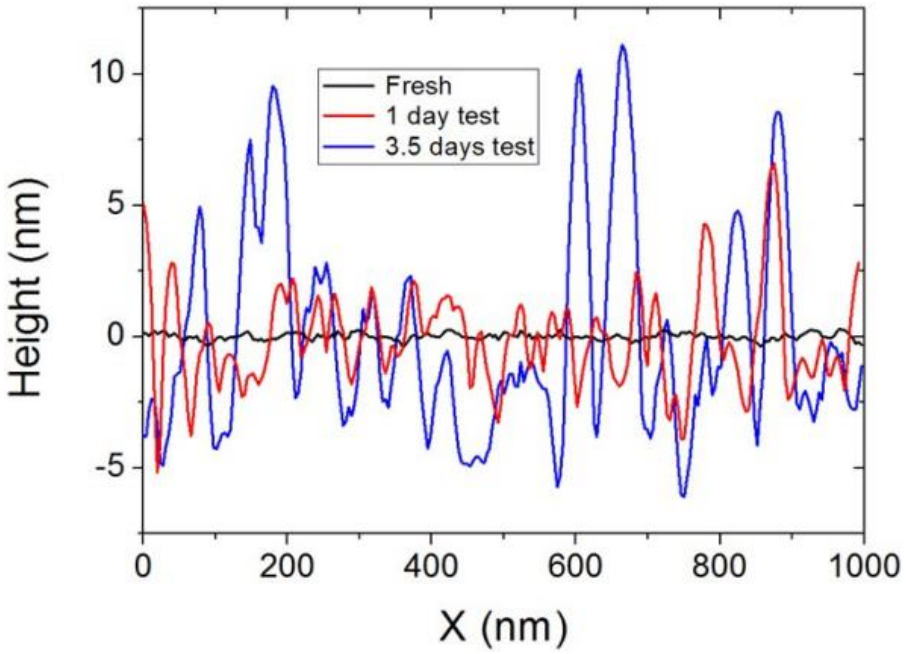

Figure 2.12 Cross section of the topographic map collected from 5 nm Ni coated n-Si photoanodes before and after PEC tests. The surface of the sample stressed during 1 day reveals typical thickness fluctuations between ± 2 nm, with some local hillocks that may correspond to degradation at pinholes. Therefore, this analysis indicates that the change on the thickness displayed in Figure 2.11b may be susceptible to some nanometric deviations.

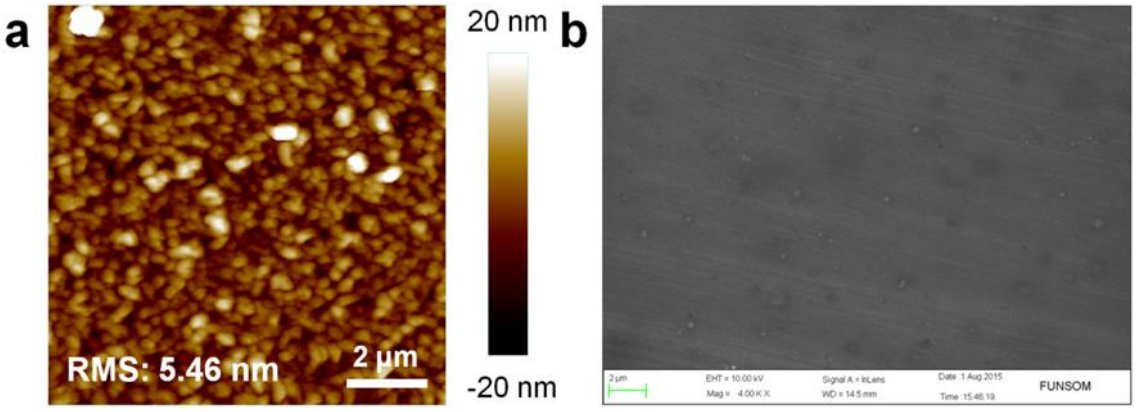

Figure 2.13 (a) AFM and (b) SEM images for the 10 nm Ni/SiOx/n-Si/Ti sample after 11 days OER test under 50 mW/cm^2 illumination. The AFM image corroborates the increase of the surface roughness.

Moreover, an n-type Si based sample coated with a 10 nm thick layer of nickel showed a stable photocurrent under the constant potential of 1.8 V vs. SCE during more

than eleven days (blue line in Figure 2.8a). Here, the roughness was clearly observed to increase after being subjected to a few days test (Figure 2.13a), as observed for the electrode coated with a 5 nm thick layer of nickel, again corroborating the formation of a rough layer able to split water. In the 10 nm thick Ni layer case, the sample showed a much longer lifetime (at least eleven days) when exposed to the continuous OER, and most of the sample surface showed a morphology free of holes (Figure 2.13b). The thicker nature of the layer probably reduced the initial density of pinholes,[160] leading to a less ion-permeable layer that was less susceptible to corrosion.

2.3.3. Ageing mechanisms of 2 nm Ni/SiO_X/n-Si/Ti photoanodes

Similar experiments were performed for the samples coated with 2 nm thick layers of nickel. Figure 2.14 shows the I–t curves acquired after 8 h, 11 h, 15 h, 28 h and 57 h OER tests for five photoanodes with 2 nm thick layers of nickel fabricated in three different batches; the results revealed excellent repeatability and small variability. Interestingly, all photoanodes coated with 2 nm thick layers of nickel showed a degradation profile quite different from the degradation of the other photoanodes, and that was characterized by three degradation steps during the long-duration I-t tests at the constant potential of 1.8 V vs. SCE: (I) a slow decay in the current during the first seven hours, (II) a severe current degradation for the next four hours; and (III) then a slow decay again with a slope similar to that observed in the first step. Again, both SEM and AFM images, shown in Figure 2.14b and c, respectively, revealed an increase of the surface roughness with testing time: the roughness progressively increased from an initial value of 0.11 nm up to a final value of 2.86 nm after 57 h PEC test. There are two particularly noteworthy aspects of this degradation process: (i) this final 2.86 nm value was much smaller than the 102 nm roughness value measured for the sample with 5 nm thick Ni (in Figure 2.8c), and the 24.07 nm value measured for a piece of silicon corroded by KOH (in Figure 2.9b); and (ii) the SEM images did not reveal the formation of large hole defects in the catalyst within the first 57 h PEC test (see Figure 2.14b).[49,152] In fact, in longer-duration water-splitting tests of 2 nm Ni coated n-Si photoanodes, hole defects started to appear on the electrode only after three days (see inset in Figure 2.14b and 2.15a). Sun et al. associated the formation of holes to silicon corrosion through small pores and/or grain boundaries in the NiO_X film.[71] Our sequences of SEM images provided new insights about the formation of hole defects:

the average diameter of the holes increased with the thickness of the nickel coating increasing (as shown in Figure 2.15), and the sizes of the holes for each nickel thickness show relatively low variability (i.e., the largest holes for the 2 nm thick sample were always smaller than the smallest holes in the 5 nm thick sample).

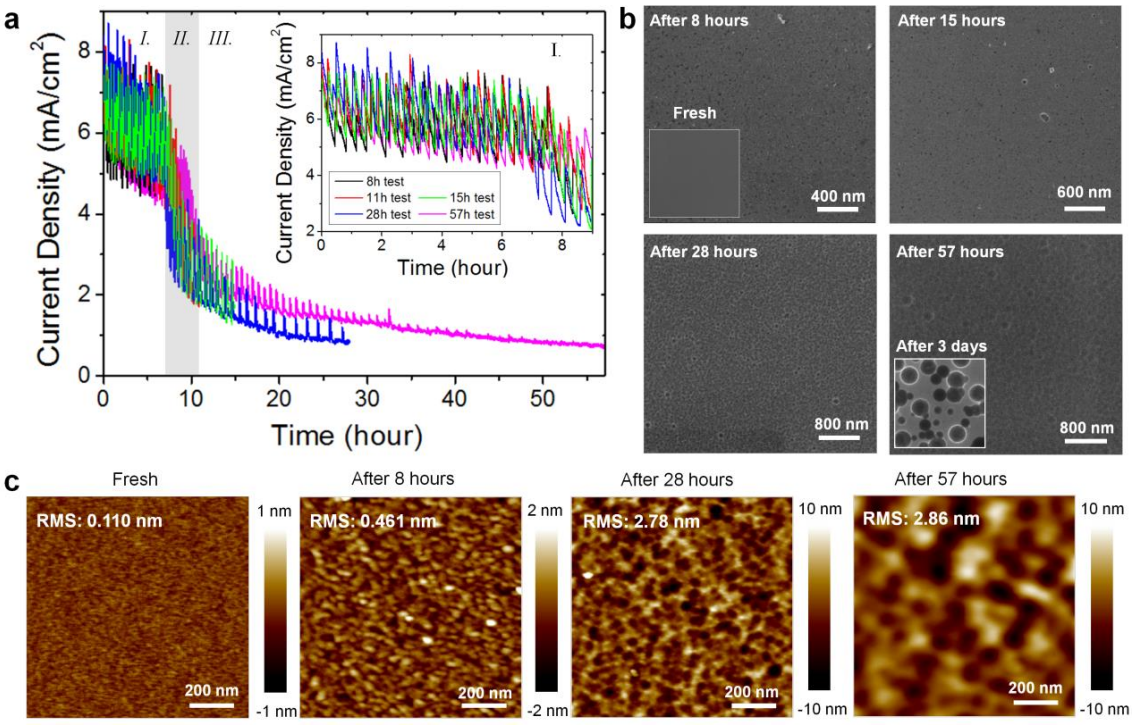

Figure 2.14 Degradation process of silicon photoanodes coated with 2 nm thick layers of Ni. (a) Amperometric I–t curves measured at a constant potential of 1.8 V vs. SCE on five different 2 nm thick Ni/SiOx/n-Si/Ti photoanodes for different periods of times in 1.0 M KOH under an illumination of 50 mW/cm^2. The degradation of each photoanode sample took place in three clearly distinguished steps (I, II and III). The inset shows a magnified view of the first step, and excellent reproducibility was observed. Panels (b) and (c) show the SEM and AFM images collected on the Ni-coated silicon photoanodes after different testing times. The images of the fresh samples are also shown as a reference. The sample showed dramatic degradation after the 57 h test, which was accompanied by an increase in the roughness, but almost no holes were detected. (They appeared only after three days of the test).

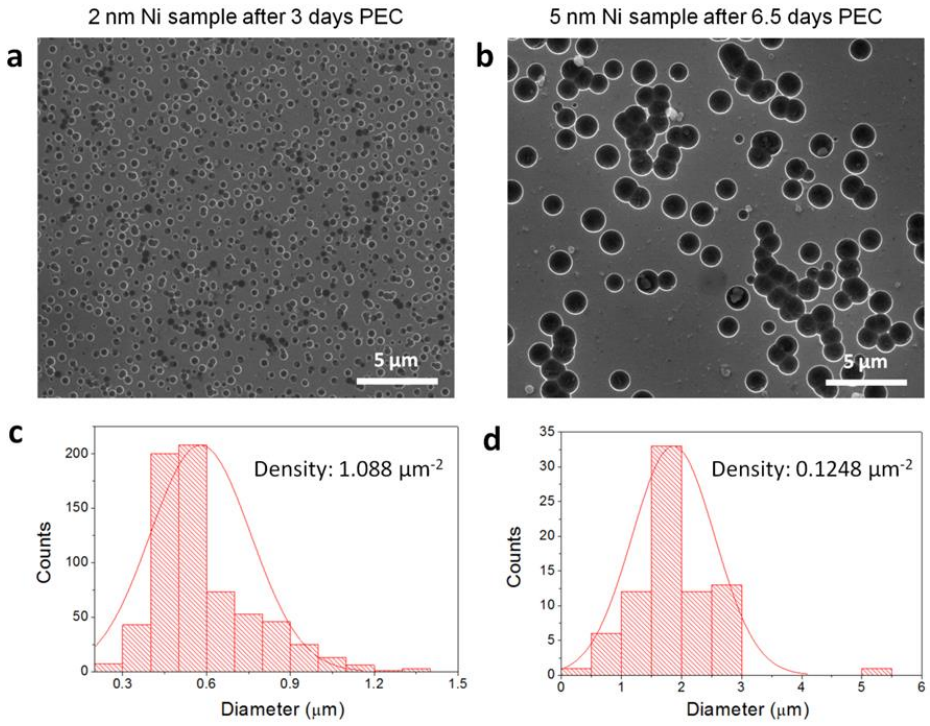

Figure 2.15 Morphological change of the two photoanodes with different nickel thicknesses after different testing times under the continued potential of 1.8 V vs. SCE and the light illumination of 50mW/cm^2. Panels (a) and (b) show SEM images of 2 nm Ni/SiO$_X$/n-Si/Ti sample after 3 days PEC test and 5 nm Ni/SiO$_X$/n-Si/Ti sample after 6.5 days PEC test, respectively. Panels (c) and (d) show the size distributions of the formed holes appeared on SEM images (a) and (b), respectively. The corrosion-related holes start to appear at different times and they have different sizes. Also the amount of holes per micrometer square is different for each photoanode.

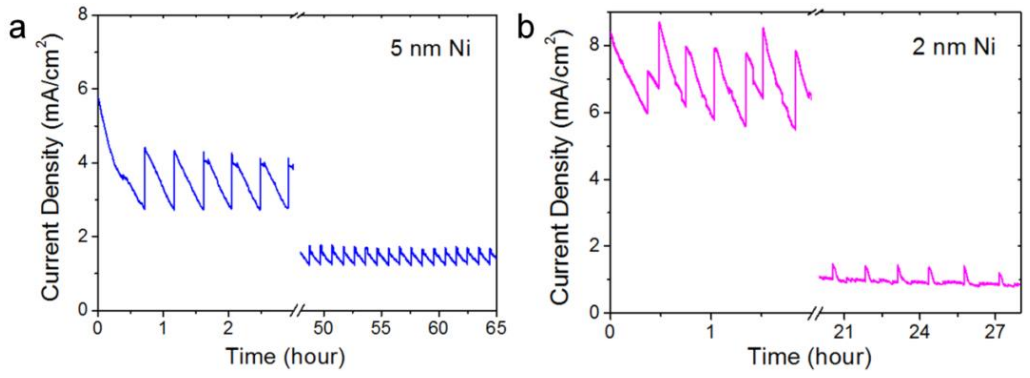

Figure 2.16 Amperometric I-t curves measured for the 5 nm Ni/SiO$_X$/n-Si/Ti photoanode (a) and 2 nm Ni/SiO$_X$/n-Si/Ti photoanode (b) collected under 50 mW/cm^2 light intensity in 1.0 M KOH by applying a constant potential of 1.8 V vs. SCE. The

plots display the different shapes (conduction mechanisms) of the I-t curves for initial and final times.

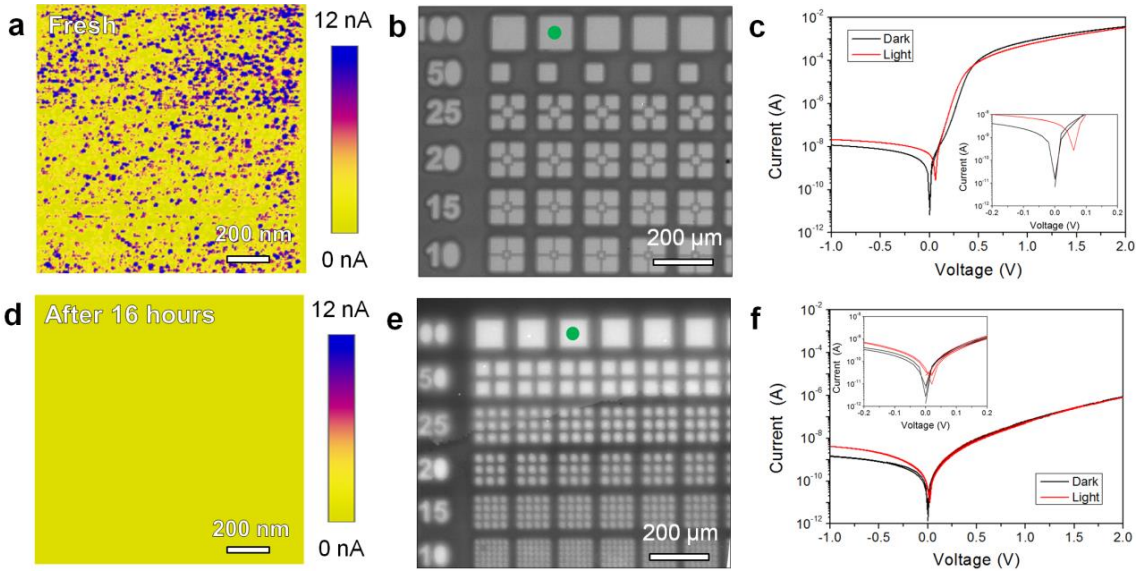

Figure 2.17 Electrical characterization of the silicon photoanodes coated with 2 nm thick layers of Ni. CAFM current maps of the 2 nm thick Ni/SiOx/n-Si/Ti photoanode before (a) and after (d) a 16 h continuous OER measurment. The maps were obtained without bias and under illumination. Panels (b) and (e) show the SEM images of the patterned squared electrodes on the fresh and tested samples, respectively. Panels (c) and (f) show the I–V curves collected with the probe station for the fresh and tested samples, respectively. The black and red lines correspond to the I–V curves collected in the dark and under illumination, respectively. The I–V curves shown in panels (c) and (f) were collected at the capacitors highlighted with green spots in panels (b) and (e), respectively. And the insets in panels (c) and (f) show the magnified views of I-V curves from -0.2 V to 0.2 V.

The absence of holes in the 2 nm thick samples before three days PEC test indicated that the degradation of the cells was not related to the appearance of these defects during the OER, but instead to the formation of a rough layer unable to split water. Note that the thicker samples maintained the initial sawtooth shape during the entire degradation process (see Figure 2.16a), while in the 2 nm thick samples the initial sawtooth shape (related to the formation of bubbles during the PEC test) changed into sharp peaks (see Figure 2.16b), indicating a change in the mechanisms of conduction

through the photoanode. This behavior was analyzed in-depth at the nanoscale and device level using the CAFM and the probe station, respectively. Figure 2.17a and d show the CAFM current maps of the fresh and tested 2 nm thick Ni/SiO_X/n-Si/Ti photoanodes (under illumination and without bias). The abundant photocurrent observed in the fresh sample completely vanished in the sample exposed to the OER for 16 h. For the device-level characterization, squared Au electrodes of different sizes were patterned on the fresh and tested samples using a shadow mask and a thermal evaporator (Figure 2.17b and e). The measured I–V curves collected on the fresh sample (Figure 2.17c) showed a typical photocurrent at 0 V, as well as an open-circuit voltage of 60 mV. In contrast, the sample exposed to 16 h of the OER showed an almost negligible photocurrent and open-circuit potential, as well as much smaller currents at high biases (Figure 2.17f), indicating that the conductivity of the photoanode had been dramatically reduced after the PEC test. The XPS analysis (Figure 2.18) of the samples containing 2 nm thick Ni layers did not reveal any significant change compared to the samples containing 5 nm thick Ni layers: the nickel, oxygen and potassium profiles were very similar, and the only remarkable change was the larger silicon signal for the samples with the thinner layer of nickel. Interestingly, there was a correlation between the potassium signal and the degradation of the sample.

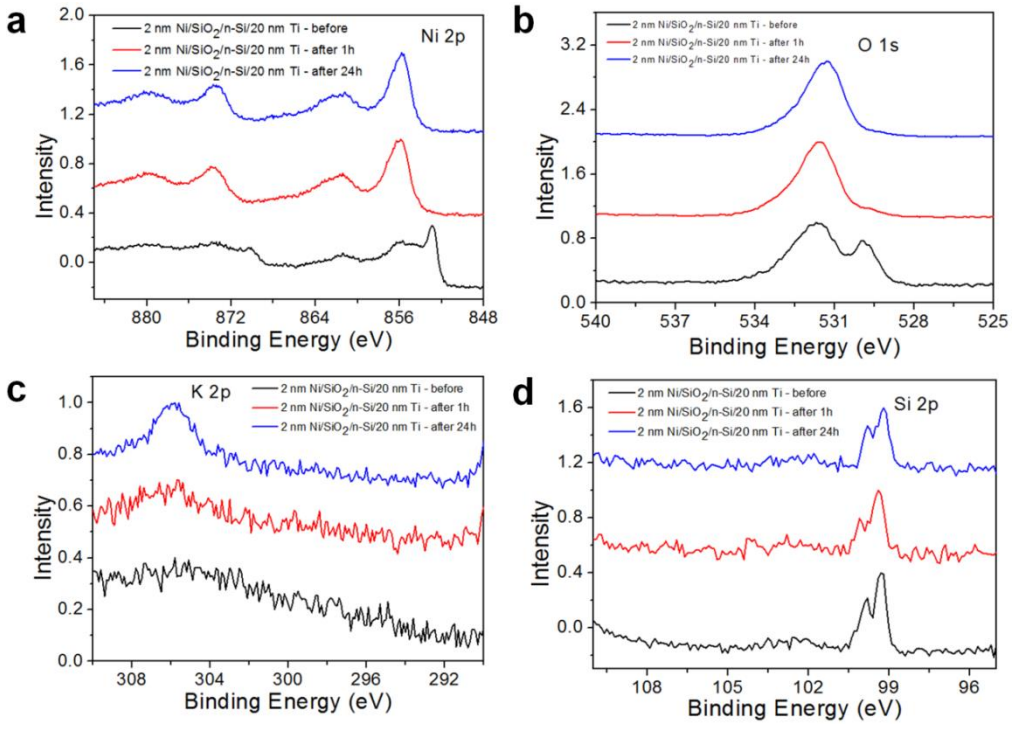

Figurer 2.18 XPS spectra for the 2 nm Ni coated n-Si photoanodes after 1 h (red) and

24 h (blue) PEC tests. The spectra of the fresh sample are also showed as reference (black). Panels (a), (b), (c) and (d) are the narrow spectra of Ni 2p, O 1s, K 2p and Si 2p elements, respectively.

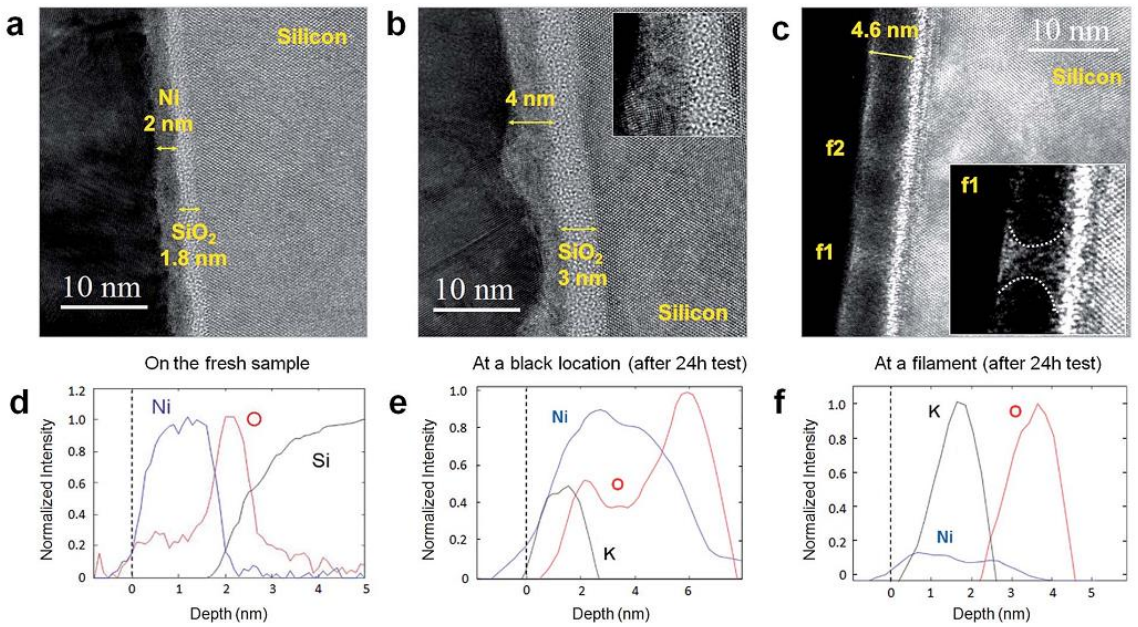

Figure 2.19 Atomic-scale information of fresh and tested silicon photoanodes coated with 2 nm thick layers of Ni. Cross-sectional TEM images for the 2 nm thick Ni/SiOx/n-Si sample (a) before the PEC tests, (b) after a one-hour test and (c) after a 24 h test. Panel (b) shows a location with especially high surface roughness and film modification, and the inset shows the magnified view of a partial area in the Ni layer. Panel (d) shows the EELS chemical composition of the fresh sample. Panels (e) and (f) show the EELS chemical composition of the sample after the 24 h test, along the sections containing a dark and a light region in panel (c). The inset in Panel (c) also clearly shows one light filament (f1) in the Ni layer.

Further observations were made when the sample was analyzed with X-TEM and EELS techniques. Again, the fresh sample showed the expected thickness, chemical composition and polycrystalline structure (Figure 2.19a), and the EELS data in Figure 2.19d also confirmed the chemical composition and thickness of Ni layer and SiO_X adhesion layer. After 1 h PEC test, the X-TEM images clearly displayed an increase in the roughness. Figure 2.19b shows a part of the sample that was especially corroded, and local changes in the morphology of the material were clearly identified (see inset in

Figure 2.19b). Interestingly, in this case the interfacial native SiO_X film experienced a much larger increase in the thickness, leading to a film with an effective thickness always above 3 nm. Such a thick insulating layer was probably the main factor limiting the conduction from the electrolyte to the silicon substrate, as observed in Figure 2.17d and f, and producing the activity decay (Figure 2.14a). After 24 h of the PEC test (Figure 2.19c), the thickness of the Ni layer increased to 4.6 nm, the film became darker and, interestingly, some light nanofilaments (i.g. f1, f2) connecting both sides of the coating were distinguished. The EELS chemical profiles obtained from a black location and a light filament in Figure 2.19c (displayed in Figure 2.19e and f, respectively) revealed the formation of an NiO_X layer rich in potassium on its surface (Figure 2.19e), in clear agreement with our interpretation of the XPS data. The very high lateral resolution of this technique allowed us to assess the chemical composition of the light nanofilaments, and revealed them to be rich in potassium, which can penetrate the nickel layer and reach the underlying SiO_X layer (Figure 2.19f). Figure 2.19f shows an inverse relationship between the Ni concentration and the potassium signal, indicating that the potassium was present only where pinholes formed. We speculate that pinholes nucleated at defects in the Ni surface, which became rough and rich with defects after a few hours of operation, and punched through the whole Ni layer and reached the Si/SiO_X surface. Then, the KOH solution started to etch the Si layer below, as consequence of the well-known large etching rate of KOH on (100) Si due to the OH ions. As suggested by the results for the samples with the 5 nm thick and 10 nm thick layers of Ni, the increased Ni thickness was beneficial to extend the operation lifetime, since the pinholes had to extend through a thicker film. The unprecedented observation of local potassium filaments in the sample coated with only a 2 nm thick layer of Ni demonstrated that XPS may have masked essential information with regard to the degradation process of the samples, and future investigations should include such kinds of analyses.

2.4. Conclusions

In summary, in this chapter the degradation process of $Ni/SiO_X/n\text{-}Si/Ti$ photoanodes under a light-driven OER has been analyzed on the sub-nanometer scale. The main conclusions of this work are as follows. (i) The use of a thicker Ni coating resulted in a lower solar cell activity yet longer lifetime. (ii) The failure of the samples coated with a

2 nm thick layer of nickel within 18 h for PEC water splitting was due to the formation of a thick interfacial SiO_X film, which blocks hole/electron transfer to the electrolyte/substrate. And the extensive penetration of potassium impurities into the NiO_X layer that was detected by EELS also made significant effects on the degradation process. (iii) The samples coated with the 5 nm thick and 10 nm thick nickel layers showed stable currents under a constant potential lasting for more than 150 and 260 h, respectively. These thicker Ni films were also converted to NiO_X, but the resulting layer was very homogeneous and free of impurities. The degradation of these samples was related to the formation of numerous holes in the active NiO_X layer, and the size/density of holes depended on the thickness of the NiO_X layer. (iv) We demonstrated that essential information was masked in the XPS profiles, as the potassium contamination in the NiO_X film could only be detected by combining TEM and EELS techniques. This information indicated that previous reports in the field of water splitting (which normally use traditional characterization tools with low spatial resolution) may be ignoring essential degradation phenomena. These findings may be of interest to the investigators who focus on water splitting project, as they reveal essential information that could be useful to enhance the lifetime of PEC water splitting solar cells.

Chapter 3:
Effect of different alkaline electrolytes on photoelectrochemical performance

3.1. Introduction

Since Fujishima and Honda developed the first electrodes (n-type TiO_2) for water photolysis in 1972,[12] sunlight-driven photoelectrochemical (PEC) water splitting has been one of the most promising approaches to produce clean and sustainable energy. Using this method, inexhaustible solar energy can be used to split molecules of water (H_2O) and produce abundant hydrogen, which is an attractive clean fuel that can be easily stored and transported.[10,161-162] PEC water splitting systems use semiconducting photoelectrodes, which are immersed in a liquid electrolyte. When illuminated, the photoelectrodes can generate free electron–hole pairs, leading to a net exchange of charges with the electrolyte that results in the splitting of water molecules. This process consists of two chemical half reactions, named oxygen evolution reaction (OER) and hydrogen evolution reaction (HER), which take place on the surface of the photoanode and photocathode, respectively. Silicon is an excellent candidate material for being used as a photoelectrode for splitting water due to its high photon absorption and low price, and several Si-based photoelectrodes for PEC water splitting have been reported.[50,78,163-164] However, silicon can be corroded easily in alkaline and acid electrolytes, which results in the premature failure of the entire device. To solve this problem, one easy and effective solution is to coat the surface of silicon photoelectrodes with a protective metallic layer, which, at the same time, can act as a catalyzer, improving both the activity and stability of the PEC water splitting system. This solution has also used other wide band gap semiconductors,[52-54,70-71,152,165-169] metals,[49,66,113,164,170-171] and other variety of materials[163,172-175] considered as photoelectrodes for PEC water splitting solar cells.

Materials based on the first-row transition metal have been widely used as coatings on silicon photoelectrodes for PEC water splitting. Especially, Ni-based coatings (e.g., Ni, NiO_X) have attracted a lot of interest in the field of water splitting due to their low

cost and good ability to enhance the activity and stability of the photoelectrodes.[49,66,70-71,113,152,170,176] Gong et al. summarized the most relevant research progress using Ni-based catalysts to generate highly active HER in the alkaline electrolytes.[176] Moreover, Ni-based catalysts can also produce fast OER in alkaline conditions. Kenney et al. fabricated 2 nm Ni-coated n-Si photoanodes that exhibited a very low onset potential (V_{ON}) of ~1.07 V vs. reversible hydrogen electrode (RHE) in 1.0 M potassium hydroxide (KOH), but its stability was only ~12 h.[49] In our previous work,[170] we have statistically analyzed the ageing mechanisms of similar 2 nm Ni-coated n-type Si photoanodes in 1.0 M KOH, and we found that the performance decayed fast due to the formation of a thick interfacial SiO_X film that blocked the current. In n-Si photoanodes coated with thicker Ni films (≥5 nm), the degradation was slowed down, achieving stabilities of ~156 h. In this case, the mechanism triggering the failure of the device changed: the thicker Ni film avoided the oxidation of the underlying n-Si by blocking oxygen ion penetration, but prolonged exposure to KOH, resulting in the formation of pinholes on the surface of the Ni film. However, the use of thicker Ni coatings reduces the amount of sunlight penetrating into the underlying n-Si photoanode, resulting in a lower activity at pH 14 (i.e., the V_{ON} of 2 nm Ni/SiO_X/n-Si/Ti photoanodes is ~1.07 V vs. RHE, whereas the V_{ON} of 5 nm Ni/SiO_X/n-Si/Ti photoanodes is ~1.37 V vs. RHE).[49,170] Therefore, this presents an important trade-off when designing metal-coated Si photoanodes, and a still unresolved dilemma.

One potential solution to avoid this problem is the use of thicker NiO_X coatings, which can effectively passivate the surface of the silicon-based photoelectrode and, at the same time, allow effective light transmission. Using this concept idea, Sun et al. stabilized n-type Si photoanodes by coating them with a > 50 nm thick NiO_X-based p-type conducting oxide and achieved a V_{ON} of 1.36 V vs. RHE and a stability of ~600 h in 1.0 M KOH electrolyte.[71,152] The performance of these cells was further improved using np^+-Si photoanodes, which generate a larger built-in potential and promote more abundant electron–hole separation (compared with n-type Si), leading to larger photocurrents. As a result, the authors managed to fabricate a NiO_X/np^+-Si photoanode with the Ni thichkness of > 50 nm that exhibited a V_{ON} of 1.03 V vs. RHE and a stability of ~1200 h.[71] However, the use of much thicker coatings and np^+-Si junctions remarkably increases the fabrication time and cost of these photoanodes.

A much cheaper approach is to engineer the chemical composition of the electrolyte by including specific species that could slow down the degradation of the metal-coated

Si photoelectrode. As an example, Kenney et al. observed that the 2 nm Ni/SiO_X/n-Si/Ti photoanodes (which showed an onset potential of ~1.07 V vs. RHE and a stability of ~12 h in KOH) exhibited an onset potential of ~1.205 V vs. RHE and a stability of > 80 h when using an electrolyte made by mixing 1.9 g of KOH with 0.65 g of lithium hydroxide (LiOH) and 6 g of boric acid in 50 mL of water.[49] Therefore, this species combination in the electrolyte resulted in an improved stability, although the activity remarkably decreased. Other works also observed that electrolyte engineering has non-negligible effects on the electrical performance of water splitting solar cells.[24,49,126] As an example, HER is much easier to occur in acid electrolytes, whereas OER is easier to occur in alkaline electrolytes. In various acid electrolytes, different types of anions and cations could exert a substantial influence on the solar-to-oxygen conversion efficiency.[24] In strong alkaline electrolytes with different cations, the long-term activity for PEC water oxidation relies on the cations, and lithium ions could help stabilize the photoelectrodes by decreasing the strength of O-H bonds.[126] However, Ding et al. used this strategy to fabricate photoelectrodes made of metal oxides (not silicon).[126]

In this work, we have developed a novel electrolyte for highly active and stable OER using 5 nm Ni-coated n-type Si photoanodes. When immersed in 1.0 M KOH electrolytes (pH 14), these photoanodes exhibited the lowest V_{ON} (1.191 V vs. RHE), but the performance decayed after ~144 h (at 10 mA/cm^2 under the illumination of simulated 1 sun). The stability of the 5 nm Ni-coated n-type Si photoanodes (under similar testing conditions) could be enhanced to > 264 h using an electrolyte consisting of 0.68 M K-borate and 0.31 M Li-borate (pH 9.5); however, this reduced the activity of the devices (i.e., V_{ON} increased to 1.473 V vs. RHE). These two types of electrolytes were used in previous studies.[49-50,52,66,71,78,126,152,165,170,172,174,176,178] The novel electrolyte we have developed here consisted of 0.68 M KOH and 0.31 M LiOH (pH 12.5) and resulted in a competitive V_{ON} of 1.254 V vs. RHE and a stability of > 264 h. This novel KOH + LiOH electrolyte presents the best activity/stability compromising among all tests and is a promising candidate electrolyte for future silicon based photoanodes for PEC water splitting devices.

3.2. Experimental section

3.2.1. Fabrication of Electrodes

As-received phosphorus-doped (100) n-type silicon wafers (from Prolog Semicor Ltd.) with a resistivity of 0.3-0.5 Ω cm and ~1 nm native silicon oxide (SiO_X) were cleaned in acetone (first) and alcohol (second) for 10 min with sonication (power: 40 W), and dried with a nitrogen gun. After that, a 5 nm nickel layer was deposited on the polished surface of the n-Si wafer by electron beam evaporator (AJA International, Inc.) with the low pressure of $< 5 \times e^7$ (from Stanford Nanofabrication Facility). To form an ohmic contact, a 30 nm titanium layer was also deposited on the back side of the wafers with the deposition rate of ~0.28 Å/s under the voltage of 8 kV using an electron beam evaporator (from Kurt J. Lesker, model PVD75).

3.2.2. PEC characterization in different electrolytes

The photoanodes were tested in a teflon box containing the electrolyte, as shown in Figure 2.2 and 2.4a for the real Teflon box and 3D schematic one, respectively.[170] This box had two apertures facing each other, one with an area of 0.50 cm^2 to fix the photoanode and another one a bit larger to fix a glass through which light could be driven into the system. The voltages applied and currents generated were registered using a potentiostat (CHI 660E from CH Instruments, Inc.) connected to three electrodes: 1) the prepared 5 nm Ni/SiO_X/n-Si/30 nm Ti photoanodes; 2) a saturated calomel electrode (SCE, saturated KCl) as reference electrode; and 3) a solid Pt wire as counter electrode. The back side of the photoanodes was connected to the potentiostat using copper tape, and one rubber ring was used between the sample and the container to seal and avoid the leakage of the electrolytes. We prepared electrolytes with three different acidities: 1) pH 14 electrolyte, which consisted of 1.0 M KOH; this was prepared by dissolving 5.6 g of KOH in 100 mL of deionized water; 2) pH 12.5 electrolyte, which consisted of 0.68 M KOH and 0.31 M LiOH; this was prepared by mixing 3.8 g of KOH and 1.3 g of lithium hydroxide monohydrate ($LiOH \cdot H_2O$) dissolved in 100 mL of deionized water; and 3) pH 9.5 electrolyte, which consisted of 0.68 m K-borate and 0.31 m Li-borate; this was prepared by mixing 3.8 g of KOH, 1.3 g of $LiOH \cdot H_2O$, and 12 g of boric acid (H_3BO_3) in 100 mL of deionized water; 4) To compare with 0.68 M K-borate and 0.31 M Li-borate electrolyte, as a reference, another pH 9.5 (1.0 M K-borate) made of 5.6 g of KOH and 12 g of H_3BO_3 dissolved in 100 mL of deionized water. The pH of each electrolyte was measured using a standard pH meter from Mettler-Toledo Instruments (model FE20). All the chemicals used in this work

were purchased from Sinopharm Chemical Reagent Co., Ltd. During the experiments, CV with iR compensation and multi-current steps (ISTEP, Potential versus time under one constant current density) and CV without iR compensation were measured on the photoanodes under a light density of ~100 mW/cm^2 (1 sun). The illumination was provided by a 150 W Xenon lamp, and the illuminated density was calibrated by an optical power meter (model 1918R), both from Newport Corporation. During the measurements, to avoid the formation of crystals, we refilled the Teflon box with more electrolyte every 12 h and completely exchanged the electrolyte every 48 h. In this work, the onset potential is defined as the potential where the CV shows a current density of 3 mA/cm^2. To compare the activity of the photoanodes measured at different pH electrolytes, the applied potential versus RHE and related overpotential (Vover) for water oxidation can be calculated by the following Equation (4.1) and (4.2), respectively.

$$V\,(RHE) = V\,(SCE) + 0.244\ V + 0.059 * pH \qquad \text{Equation (3.1)}$$

$$Vover\,(NHE) = V_{ON}\,(SCE) + 0.244\ V - (1.23\ V - 0.059 * pH) \qquad \text{Equation (3.2)}$$

3.2.3. Materials characterization

After the electrical tests, the surface of the photoanodes was characterized at the micro and nano scales to detect the impact of different pH electrolytes on the photoanodes. The morphological changes of the samples before and after PEC tests were characterized using scanning electron microscopy (SEM, Zeiss SUPRA55) and atomic force microscopy (AFM, Veeco Multimode V) in tapping mode with NanoWorld Pointprobe tips (model NCH). Besides, the chemical composition of the samples was characterized using X-ray photoelectron spectroscopy (XPS) with the X-ray source of mono-chromatic Al Kα (model Shimadzu KRATOS AXIS Ultra DLD Scanning XPS Microprobe).

3.3. Results and discussion

The 5 nm Ni/SiO_X/n-Si/Ti photoanodes were tested in the three different kinds of electrolytes, namely, pH 14 (KOH), pH 12.5 (the mixed solution of KOH and LiOH), and pH 9.5 (the mixed solution of KOH, LiOH, and H_3BO_3), by collecting cyclic voltammetry (CV) in the dark and under 1 sun illumination (see Figure 3.1a-c). In each

electrolyte, 3–5 samples were measured, showing high reproducibility, and Figure 3.1 presents the typical PEC performance of 5 nm Ni/SiO_X/n-Si/Ti photoanodes measured in different electrolytes. The dashed lines stand for the first CV measurements with iR compensation. After different short-time (< 10 h) potential versus time (P–t) tests under a constant density of 10 mA/cm^2,[171] another CV was collected, which is shown in Figure 3.1a–c, as a solid line (activated). And the horizontal black dash lines in Figure 3.1a-c show that there is no OER current on the photoanodes measured in different electrolytes under the absence of illumination. The 5 nm Ni/SiO_X/n-Si/Ti photoanodes measured at pH 14 show lowest onset potential, 0.039 V more cathodic than the thermal dynamic potential for water oxidation, and it has achieved the saturation current (~22.0 mA/cm^2) at the potential of 1.371 V vs. RHE (see Figure 3.1a). The 5 nm Ni/SiO_X/n-Si/Ti measured at pH 9.5 with Li ions electrolyte shows an overpotential of 0.243 V (see Figure 3.1c). At pH 12.5, the onset potential for water oxidation of the 5 nm Ni/SiO_X/n-Si/Ti photoanode is 1.254 V vs. RHE, that is, an overpotential of 0.024 V (see Figure 3.1b). Also, the corresponding potentials obtaining the saturation current at pH 9.5 with Li ions and pH 12.5 are ~2.155 V vs. RHE and 1.533 V vs. RHE, respectively. These results indicate that the activity of the photoanode at pH 12.5 is much better than that at pH 9.5. For the saturated current density, there is no obvious difference among the measurements in three different electrolytes, which is more related to light absorption of the photoanodes. On the other hand, the stability of the photoanodes in different alkaline electrolytes has also been analyzed by ISTEP (P-t) tests at a constant current density of 10 mA/cm^2 under the illumination of 1 sun. As shown in Figure 3.1d, to obtain the constant current density of 10 mA/cm^2, the 5 nm Ni/SiO_X/n-Si/Ti photoanode tested at pH 14 (blue curve) initially needed ~1.860 V vs. RHE, but, after 141 h, this voltage increased up to > 2.680 V vs. RHE, which means that the sample starts to decay. At pH 9.5 (red curve in Figure 3.1d) and pH 12.5 electrolytes with Li ions (green curve in Figure 3.1d), the photoanodes still show stable potential even after 264 h PEC tests, which is related to the slower corrosion. Considering both the activity and stability of the photoanodes in these three kinds of alkaline electrolytes, the photoanodes show the best OER performance in the mixture of KOH and LiOH electrolyte (pH 12.5).

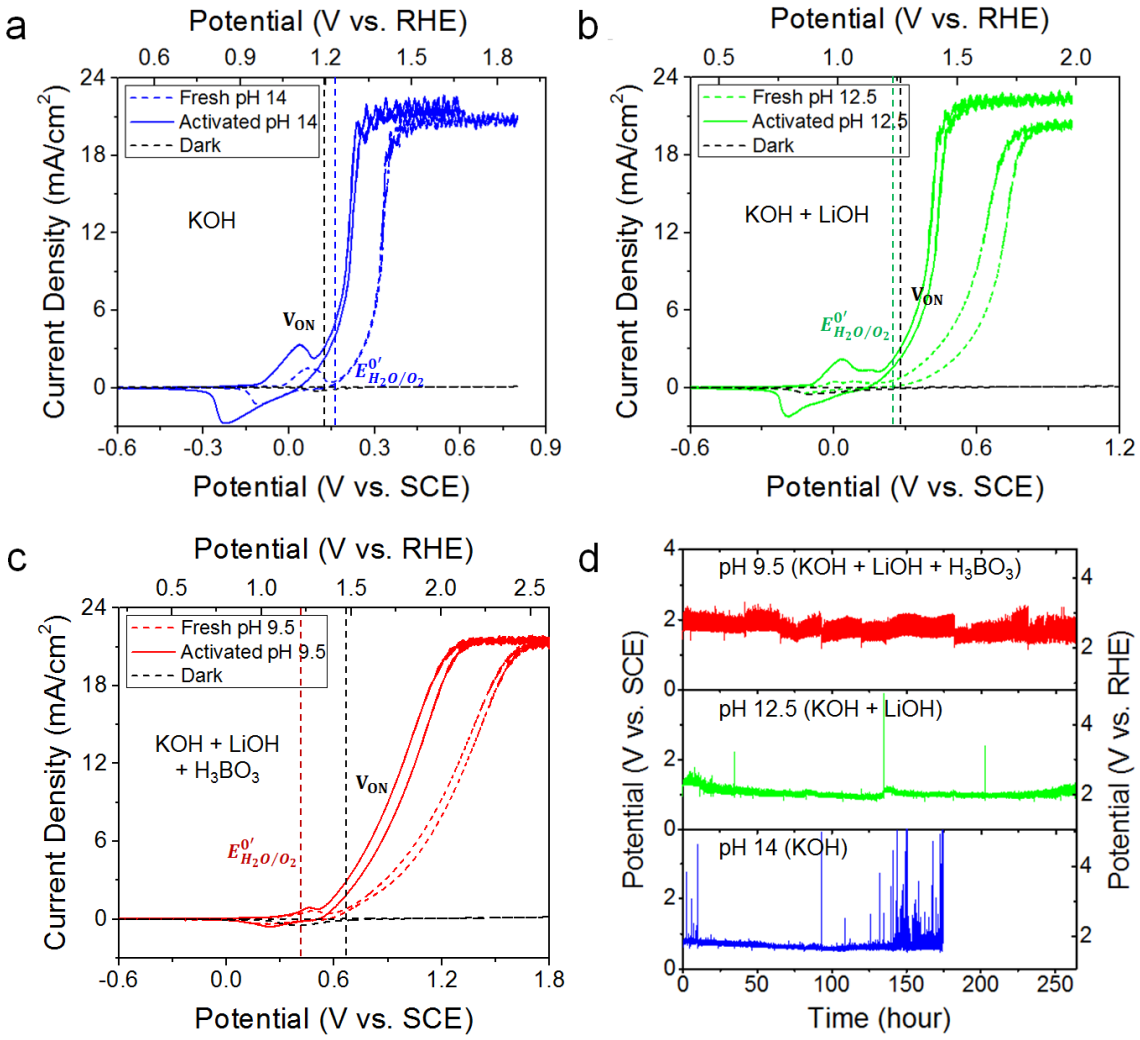

Figure 3.1 Characterization of 5 nm Ni/SiOx/n-Si/Ti photoanodes at different pH electrolytes. Typical cyclic votammograms (CV) of fresh and activated 5 nm Ni/SiOx/n-Si/Ti photoanodes measured at (a) pH 14, (b) pH 12.5 and (c) pH 9.5 under the illumination of 100 mW/cm^2. (d) Representative multi-current steps (ISTEP) under the constant current density of 10 mA/cm^2 for 5 nm Ni/SiOx/n-Si/Ti photoanodes at different electrolytes under the illumination of 100 mA/cm^2. ISTEP test results in potential versus time (P-t) data under one constant current density. The horizontal black dash lines in (a), (b) and (c) show the CV measurements in the dark at pH 14, 12.5 and 9.5. The positions located at vertical black dash line in (a), (b) and (c) stand for the onset potential at pH 14, 12.5 and 9.5, respectively. And the vertical blue, green and red dash lines in (a), (b) and (c) are the thermal dynamic potential for water oxidation at pH 14, 12.5 and 9.5, respectively. The red, green and blue curves in (d) stand for P-t curves for 5 nm Ni/SiOx/n-Si photoanodes measured at pH 9.5, pH 12.5 and pH 14, respectively.

To further understand the effects of pH value and Li ions on the stability of 5 nm Ni-based n-Si photoanodes, another type of pH 9.5 (1.0 M K-borate) electrolyte was prepared and used for PEC characterization. As shown in Figure 3.2a, the photoanode tested in 1.0 M K-borate electrolyte without Li ions shows an onset potential of 1.453 V vs. RHE for water oxidation, similar to the result at pH 9.5 with Li ions electrolyte. Besides, in 1.0 M K-borate, the photoanode just shows stability in 80 h, as shown in Figure 3.2b, which is much less stable than the measurement in 0.68 M K-borate and 0.31 M Li-borate electrolyte (> 264 h). These results from the photoandes measured at four different electrolytes with or without Li ions demonstrate that the influence of pH value is much lower than that of Li ions in the electrolytes.

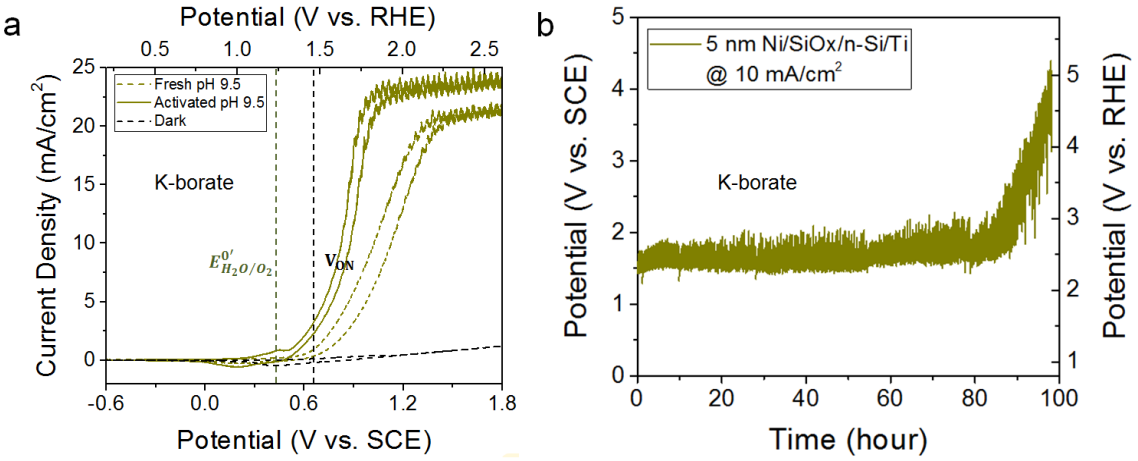

Figure 3.2 Photoelectrochemical (PEC) characterization of 5 nm Ni/SiO_X/n-Si/Ti photoanode under the illumination of 100 mW/cm^2 at pH 9.5 (1.0 M K-borate) electrolyte without Li ions. (a) Typical cyclic voltammograms (CV) of fresh and activated sample. (b) Representative multi-current steps (ISTEP) under the constant current density of 10 mA/cm^2. The horizontal black dash line in (a) shows the CV measurement in the dark at pH 9.5 electrolyte. The position located at vertical black dash line in (a) stands for the onset potential, and the vertical yellow dash line in (a) stands for the thermal dynamic potential for water oxidation at pH 9.5 electrolyte without Li ions.

To identify the reason why the activation takes place, X-ray photoelectron spectroscopy (XPS) characterization was performed to analyze the chemical composition of fresh 5 nm Ni/SiO_X/n-Si/Ti photoanode, the photoanodes after 144 h

PEC tests at pH 9.5 with Li ions and pH 12.5, and the one measured at pH 14 for 174 h. For fresh sample, due to thick 5 nm Ni layer on the surface, black trace in Figure 3.3a shows weak signal for the Si 2p spectrum. The peaks of O 1 s in Figure 3.3b (black trace) at 531.3 and 529.3 eV should be related to the oxygen on the surface and the formation of few NiO_X in the air, respectively.[66]

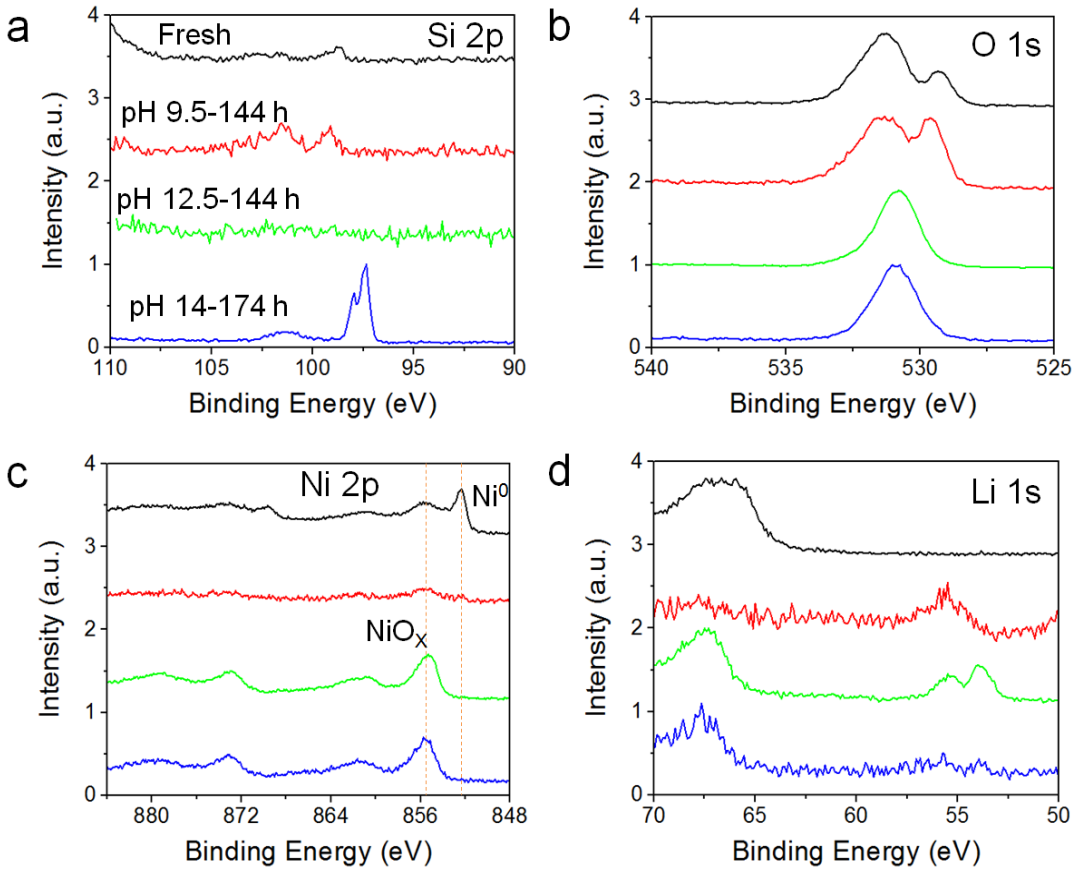

Figure 3.3 Chemical composition analyses of 5 nm Ni/SiO_X/n-Si/Ti photoanodes before and after PEC characterization measured at different pH electrolytes. XPS spectra of Si 2p, O 1s, Ni 2p and Li 1s element composition are shown in (a), (b), (c) and (d), respectively, which track the changes of the 5 nm Ni/SiO_X/n-Si/Ti photoanodes after PEC tests at different pH electrolytes. In each panel, black, red, green and blue curves show XPS spectra of fresh and 5 nm Ni/SiO_X/n-Si/Ti photoanodes at pH 9.5 with Li ions for 144 h PEC test, pH 12.5 for 144 h PEC test, and pH 14 for 174 h PEC test, respectively.

After PEC tests, the two peaks at 852.4 and 869.6 eV (black trace in Figure 3.3c)—which may be related to the $2p^{3/2}$ and $2p^{1/2}$ binding energies of Ni^0 metal on the

surface of fresh sample—disappeared, and another two peaks at 855.4 and 872.9 eV (green and blue traces in Figure 3.3c) appeared, indicating the formation of nickel oxide.[66,170] The activation process may be produced by the catalytic nickel oxide formed by the Ni oxidation, which could act as a p-type hole conducting layer contributing to the charge separation and transportation of holes toward the surface of the photoanodes. Compared with the fresh samples, the strengthened peak of O 1s at 529.5 eV (red trace in Figure 3.3b) after 144 h tests in 0.68 M K-borate and 0.31 M Li-borate electrolyte (pH 9.5) may be attributed to the formation of LiO_X, as indicated by the obvious peak of Li 1s at 55.6 eV (red trace in Figure 3.3d). Furthermore, after 144 h PEC tests at pH 12.5, XPS analyses show two small peaks of Li 1 s at 55.4 and 54.0 eV, as shown with green curve in Figure 3.3d, indicating the presence of lithium oxide or lithium hydroxide. These demonstrate that Li penetrates into the Ni layer and improves the stability of the photoanodes for PEC water splitting, which makes the photoanodes be able to split water after 264 h.

To understand the morphology changes of the photoanodes after PEC tests at different alkaline electrolytes, scanning electron microscopy (SEM) and atomic force microscopy (AFM) in tapping mode analyses were collected on the surface of the tested photoanodes. As a reference, Figure 3.4a and e shows the SEM and AFM images of fresh 5 nm Ni/SiO_X/n-Si/Ti photoanode, which is very flat with a surface roughness of 0.35 nm. After 144 h PEC tests in 0.68 M K-borate and 0.31 M Li-borate electrolyte (pH 9.5), the surface is rich of small particles (see Figure 3.4b and f), and the surface roughness of the photoanode increased from the initial value (0.35 nm) to 11.8 nm. The increase of surface roughness does not degrade the performance of the photoanode for PEC water splitting (red trace in Figure 3.1d). The peak of Ni 2p in the XPS spectrum (red trace in Figure 3.3c and Figure 3.5) after 144 h PEC tests probably is related to the formation of many particles on the surface, which can hide the Ni signal detected by XPS technique. However, after 174 h PEC tests at pH 14, large amounts of big holes can be clearly observed on the surface of the photoanodes by SEM and AFM characterizations, as shown in Figure 3.4d and h, which exhibit a surface roughness increase up to 66.0 nm, demonstrating that the Ni coating is severely etched. This is in agreement with the observation of two obvious peaks of Si 2p at a binding energy of 97.5 and 101.3 eV shown with blue trace in Figure 3.3a. The first peak at 97.5 eV is related to the presence of Si, and the second one at 101.3 eV is related to the presence of

silicon oxide, indicating the severe corrosion of the Ni layer at pH 14 electrolyte (1.0 M KOH).

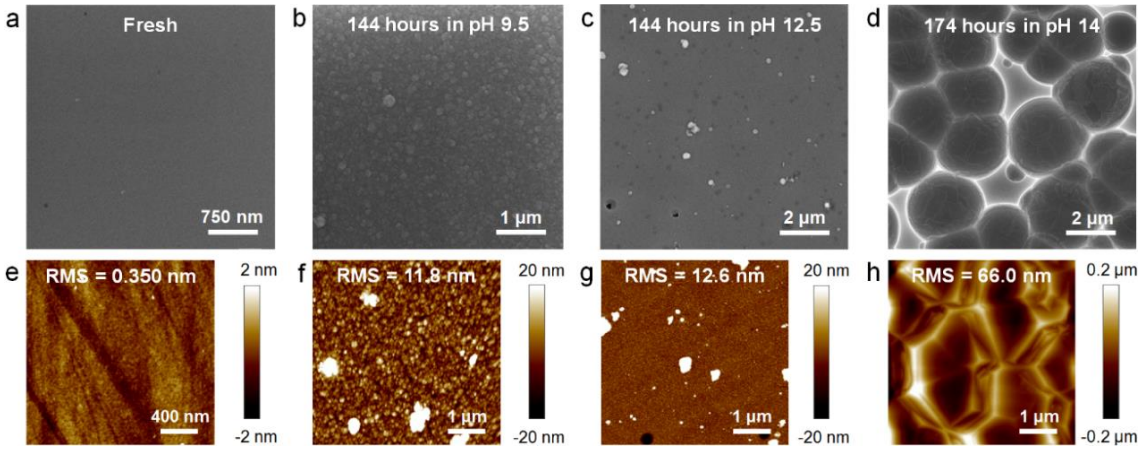

Figure 3.4 Topographical and morphological characterizations for fresh and tested 5 nm Ni/SiO_X/n-Si/Ti photoanodes at different pH electrolytes. The surface changes can be observed by SEM images of (a) fresh sample, (b) the photoanode measured at pH 9.5 with Li ions for 144 h, (c) the photoanode measured at pH 12.5 for 144 h, (d) the photoanode measured at pH 14 for 174 h and AFM images of (e) fresh sample, (f) the photoanode measured at pH 9.5 with Li ions for 144 h, (g) the photoanode measured at pH 12.5 for 144 h, (h) the photoanode measured at pH 14 for 174 h.

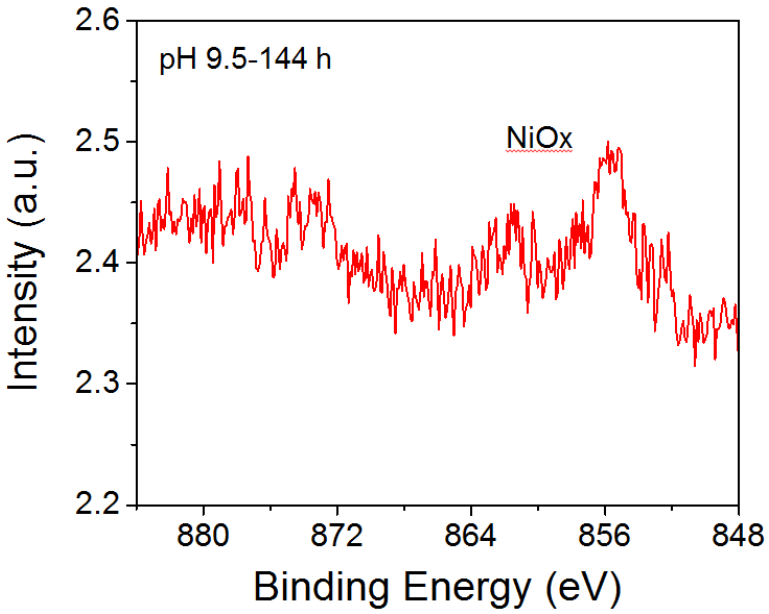

Figure 3.5 Chemical composition annalysis of 5 nm Ni/SiO_X/n-Si/Ti photoanode measured at 0.68 M K-borate and 0.31 M Li-borate (pH 9.5) after 144 h ISTEP (P-t)

PEC tests under the constant current density of 10 mA/cm^2 with 1 sun illumination. The red trace is the zoom-in XPS spectrum of Ni 2p in Figure 3.3c with red trace.

Interestingly, compared with the morphology of the photoanodes tested at pH 9.5 with Li ions, the surface of the photoanodes is rougher due to the formation of some big particles after 144 h PEC tests at pH 12.5, as observed in Figure 3.4c and g. Although the SEM image also showed few small pinholes, the long-time P–t test at pH 12.5 shown in Figure 3.1d (green trace) is still stable, indicating that few pinholes on the surface do not impact the total ability of the photoanode to split water in this electrolyte.

3.4. Conclusions

Generally speaking, the influence of different alkaline electrolytes on the performance of 5 nm Ni-based n-Si photoanodes for PEC water splitting has been analyzed. In terms of the activity, the onset potential of the photoanodes for water oxidation shows the trend of $V_{ON,\ pH\ 14} < V_{ON,\ pH\ 12.5} < V_{ON,\ pH\ 9.5}$. The photoanodes at pH 9.5 with Li ions and pH 12.5 need an overpotential of 0.243 and 0.024 V for water splitting (respectively), whereas the onset potential of the photoanode at pH 14 shows to be 0.039 V more cathodic than the thermal dynamic potential for water oxidation (0.404 V vs. NHE). However, under the long-time PEC test, the photoanodes showed much more stable at pH 9.5 and 12.5 (both with Li ions) than at pH 14, mainly due to the presence of lithium ions in the electrolytes, and they still stay stable potential after 264 h P–t tests under the constant current density of 10 mA/cm^2. Considering both the activity and stability, it is worth emphasizing that the 5 nm Ni-coated n-Si photoanodes show the best OER performance at pH 12.5 electrolyte. Overall, tuning the chemical composition of the electrolyte is an inexpensive and effective method to improve the performance of Ni-coated n-Si photoanodes for PEC water splitting. Future works should explore this approach that may also be useful to improve the performance of other metal-coated photoelectrodes for water splitting, not only for OER but also for HER.

Chapter 4:
Photoelectrochemical water splitting in silicon based photocathodes enhanced by plasmonic and catalytic nanostructures

4.1. Introduction

Using sunlight to split water into hydrogen and oxygen recently raised considerable interest to produce sustainable and clean fuels alternative to fossil fuels. Photoelectrochemical (PEC) water splitting was initially studied in wide band gap semiconductors (e.g. TiO_2, $SrTiO_3$, $KTaO_3$, RuO_2 or 4H-SiC) to achieve sufficient photovoltage to split water.[12,179-182] However, most of the wide band gap semiconductors only operate under ultraviolet (UV) light, which accounts for only ca. 4% of the total solar energy.[183] Therefore such approaches imply an inherently low photocurrent. To increase photocurrent, photoelectrodes with the ability to work under visible light are highly desirable, since visible light contributes to almost half of the incoming solar energy. For example, metal sulphides[184-185] and selenides[186-187] are considered promising for water splitting by visible light. Silicon is also a very attractive material because of its earth-abundance and prevalence in the electronics and PV industries. In particular, using crystalline silicon junctions would take advantage of the very advanced technology, low cost, and high photovoltaic efficiency (25.6% on crystalline Si solar cell).[188] However, the realization of a silicon based PEC device must overcome the inherent corrosion of this semiconductor in electrolytes with high basic pH,[189] which are required in high efficiency electrolyzers. For this reason, initially, the stand-alone water splitting PEC cell configurations based on silicon photoelectrodes used wires[190] or conductive oxide[191-192] to physically shield the silicon from the electrolyte and to connect the semiconductor to the hydrogen and/or oxygen generating electrodes. More recently, catalysts comprising earth-abundant materials have been integrated with silicon solar cells, obtaining almost stable production for 10 h, but with current density on the order of 4 mA/cm^2.[193] Tunneling

oxide layers have also been recently explored to stabilize silicon photoelectrodes covered with metals.[49,52,59-60,167,170,194] The metal layers act as catalytic films and improve the photoelectrode endurance, but since metals are not transparent, they can remarkably reduce the amount of light arriving into the semiconductor. There is therefore a trade-off between stability and maximum photovoltaic (PV) current.[170] To overcome those limits another approach is to cover silicon based photoelectrodes with wide band gap semiconductors such as $BaTiO_3$,[54] TiO_2[52,167,194-196] and Al_2O_3,[197] or with ultra-thin 2D semiconductors such as MoS_2,[95,198] reaching current density up to 25 mA/cm^2, as reported in a recent paper.[198]

In this chapter we have used n-type 3C-SiC/p-type Si heterojunction as photocathode. We investigated a 3C-SiC polycrystalline layer deposited by chemical vapour deposition (CVD) on crystalline Si. SiC acts as both Si protective layer and PEC cell emitter. The absorber material of the photocathode is the p-type crystalline Si substrate. The following are the reasons why employ 3C-SiC on Si. First, SiC is a very stable material under harsh environments. Second, among the SiC various polytypes, the 3C-SiC can be grown (amorphous, polycrystalline or even epitaxial) on Si at a relatively low CVD deposition temperature. Third, the band alignment of 3C-SiC (4.0 eV electron affinity[199] and 2.3 eV band gap) may enable the formation of an effective heterojunction solar cell on Si, as it suppresses the minority carrier injection from the Si substrate (both when it works as photocathode, thanks to the 1 eV barrier for holes injected from Si into SiC, and when it works as photoanode, thanks to the 0.2 eV barrier to the injection of electrons into the SiC layer).

As an example, Figure 4.1 shows the energy-band diagram of an n-type 3 C-SiC/p-type Si heterojunction solar cell forward biased under the illumination of 100 mW/cm^2 with AM 1.5G spectrum. The band diagrams have been calculated using a computer program called PC1D that solves the fully coupled differential equations for the quasi-one-dimensional transport of electrons and holes in semiconductor devices.[200] E_C and E_V denote the conduction band and valence band, respectively. E_{Fn} and E_{Fp} denote the quasi-electron and quasi-hole Fermi levels under illumination. The E_C and E_V band offsets at the SiC/Si heterojunction as above described are evident.

About 3C-SiC/Si photovoltaic cells, previous studies showed that n-type Al-doped ZnO (AZO)/n-type 3C-SiC/p-type (100) oriented crystalline Si heterojunction cells have good electrical characteristics, although the open circuit voltage is quite low, because of a low minority carrier lifetime.[201]

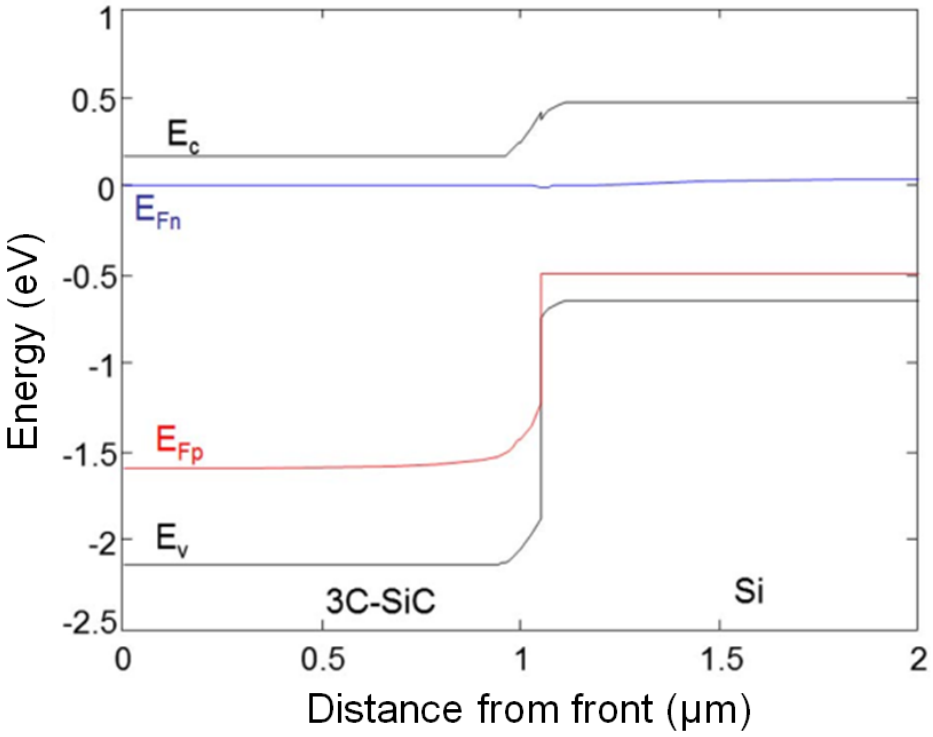

Figure 4.1 Energy-band diagram of n-type 3C SiC/p-type Si heterojunction photovoltaic (PV) cell calculated using the PC1D simulation software under AM 1.5G illumination of 1 sun (100 mW/cm^2).

Moreover, in this chapter we also studied the effect of integrating noble metal nanoparticles (NPs) on the 3C-SiC film surface to investigate the catalytic effects on the hydrogen (H_2) production. Recently, noble metal (such as Au, Ag or Pt) nanostructures have been extensively studied for improving the photoactivity of wide band gap semiconductors.[202-206] In this work we show that, under suitable conditions of metal nanoparticle deposition, evidence for photocurrent enhancement can be obtained with a p-Si based photocathode covered by n-3C-SiC. And the enhancement is attributed to plasmonic effects of metal NPs.

4.2. Experimental section

4.2.1. Photocathodes fabrication

N-type 3C-SiC polycrystalline layers were grown by hot-wall chemical vapor deposition (CVD) as detailed in Ref. [207] on (100) p-type 6″ Si wafers (from

STMicroelectronics, Catania, Italy) with a resistivity of 1.5-4 Ohm·cm. During the fabrication process by CVD, trichlorosilane (TCS) has been employed as silicon precursor, ethylene as carbon precursor and hydrogen as gas carrier. The thickness of 3C-SiC film was ~1 μm, determined by cross-sectional transmission electron microscopy (TEM), as shown by the micrograph in Figure 4.2b. The n-type doping was achieved by introducing nitrogen in the CVD chamber with a flux of 0.75 slm. A multi-step process was adopted in order to minimize the formation of voids at the Si/SiC interface. The carbonization step was performed at 900°C and then the temperature was increased up to 1200°C for a more effective incorporation of nitrogen. The back surface field (BSF) contact to the Si substrate was obtained by depositing boron doped amorphous Si on the back of the wafer and with rapid thermal annealing at 1100 °C. To check the functionality of the cells, on top of some wafers AZO contacts of 900 nm thickness were deposited by sputtering and defined by photolithography and wet etch processing. The resulting cells size was from 0.3×10^{-4} cm^2 to 0.32 cm^2.[201]

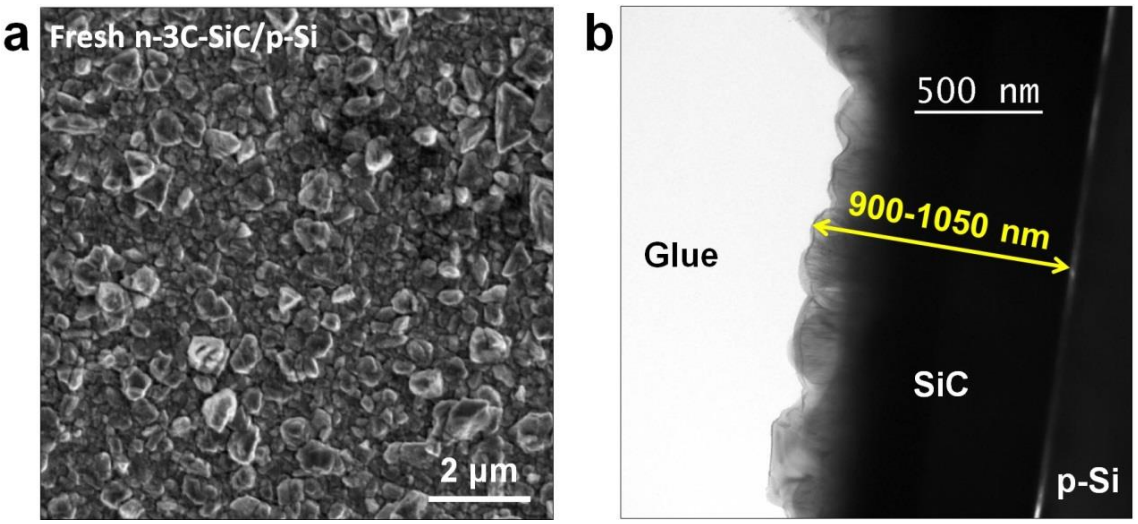

Figure 4.2 (a) SEM micrograph of the n-type 3C-SiC layer deposited on Si (100). (b) 3C-SiC polycrystalline layer on Si (100) observed in cross section by TEM. The thickness is ~1 μm.

Some of the 3C-SiC/Si samples were covered by a layer of Au or Pt NPs after cleaning in acetone with sonication for 3 min at 60 ºC. For Pt NPs deposition, some of the 3C-SiC/Si samples were etched in hydrofluoric acid (HF) for 4 min, which was prepared by mixing HF liquid (from VWR, which has a mass of 40%) and deionized

water with a ratio of 1 to 7. Subsequently, the resulting samples were covered by a layer of Pt NPs using magnetron sputtering (from Quorum Technologies, model: Q300T D) under a current of 20 μA for 20 s. While Au NPs were directly deposited on the surface of cleaned 3C-SiC/Si by galvanic displacement using an Au NPs solution of 1.0 mM Potassium gold (III) chloride ($KAuCl_4$, 99.995% pure from Sigma-Aldrich) in 4.8 M HF.[208] As a result, two different sets of samples were fabricated. The first, indicated in the following as Au NPs 1, was obtained by a single immersion in the Au solution for 240 s and then rinsed in deionized water. The second (Au NPs 2) was obtained by immersion for 60 s in the Au solution, followed by rinsing in deionized water. This procedure was repeated for three times, obtaining a total immersion time of 180 s in the Au solution.

4.2.2. PEC characterization of the photocathodes

The photoelectrodes were characterized using a polytetrafluoroethylene (PTFE) cylindrical container with a 0.5 cm^2 circular aperture at its bottom face, through which the 3C-SiC/Si photoelectrode was placed. The back-contact to the sample was a 0.2 cm-thick Al substrate. The electrolyte for PEC water splitting was 1.0 M KOH (pH 14), prepared by dissolving 14.0 g KOH pellets from Carlo Erba Reagents into 250 mL deionized water. The samples were illuminated at 1 sun, i.e. 100mW/cm^2 with AM 1.5G spectrum, using a L.O.T. QuantumDesign solar simulator with a high-pressure 150 W Xe short arc lamp. A mirror was used to reflect the horizontal light to irradiate the samples, and the light intensity was calibrated using a crystalline silicon solar cell as reference. PEC measurements were performed in a three-electrode system in which: *i)* our samples placed the role of photocathode, *ii)* a Pt wire was used as counter electrode, and *iii)* a saturated calomel electrode (SCE, saturated KCl solution) was used as reference electrode. To bias the various electrodes and measure voltages and currents a Keithley 4200A-SCS parameter analyzer equipped with 8 SMUs was employed. The activity and stability of the samples was analyzed by current-voltage (I-V) characteristics and voltage-time (V-t) measurements at a constant current. Before every measurement, bubbles were removed from the aperture of the container using a plastic pipette. Moreover, the onset potential values of the photocathodes reported in this work have been always collected at the current density of -1 mA/cm^2.

4.2.3. Materials characterization

The morphology and structure of the photoelectrodes before and after the PEC tests have been characterized by Scanning Electron Microscopy (SEM) with a ZEISS SUPRA™ 35, Transmission Electron Microscopy (TEM), and Scanning TEM (STEM) by using a JEOL JEM-2010F microscope operating at 200 kV. The size of the NPs in the TEM images was statistically evaluated by employing the ImageProPlus software. The external quantum efficiency (EQE) of the photocathodes in the range of 300–1100 nm was measured with no electrolyte solution by using a PVE300 Bentham System (Bentham Instrument Ltd), equipped with a 450 W Xenon lamp and 300 mm focal length monochromator. And this equipment also can be used to measure the transmittance and reflectivity of the samples.

4.3. Results and discussion

Figure 4.2a shows a SEM micrograph of the surface of the n-3C-SiC layer grown on p-Si. Figure 4.2b reports a cross-sectional TEM micrograph. Photons, on average, travel through the SiC layer and are absorbed by the Si substrate, generating electron-hole pairs which separate and are collected at the cathode and at the anode, respectively. At the cathode the electrons cause the H^+ reduction, producing H_2.

We measured the I-V characteristics under dark and 1sun illumination with 3C-SiC/Si, Au NPs/3C-SiC/Si or Pt NPs/3C-SiC/Si employed as cathodes, and with a Pt wire as counter anode electrode, and a SCE as reference electrode. Figure 4.3 reports schematically the measurements configuration during the PEC or electrochemical (EC) measurements for all the prepared cathodes. Figure 4.4a shows the current density as a function of the cathode voltage for all the samples. The cathode voltage is reported either versus the measured SCE or the calculated reversible hydrogen electrode (RHE), evaluated according to the Nernst equation at room temperature:

$$E\,(RHE) = E\,(SCE) + 0.244\ V * 0.059 \cdot pH \qquad \text{Equation (4.1)}$$

where E (SCE) is the experimentally measured potential against the reference electrode and 0.244 V is the standard redox potential of the saturated calomel electrode at 25 °C.

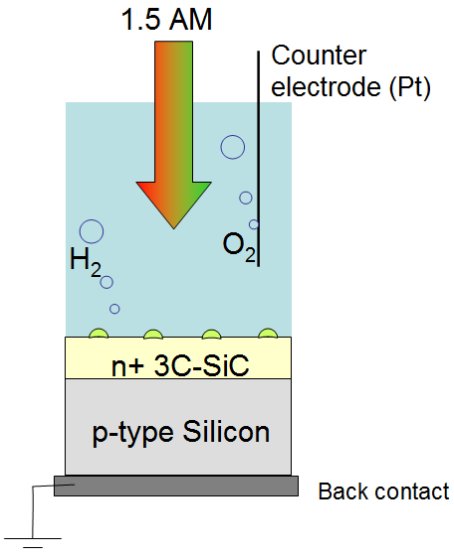

Figure 4.3 (a) The setup used to characterize the photocathodes.

In this work, two types of Au NPs (Au NPs 1 and Au NPs 2) were characterized, which prepared by galvanic displacement with two different fabrication processes, as described in Experimental section for detailed information.

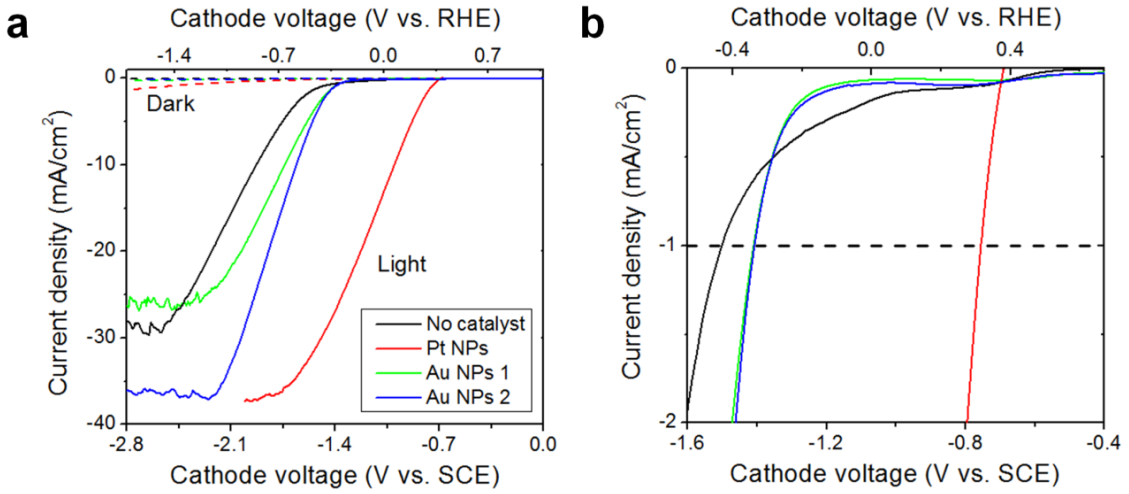

Figure 4.4 The activity measurement of n-3C-SiC/p-Si based photocathodes. (a) shows the current density versus cathode voltage (I-V) of four different samples, 3C-SiC/p-Si, two types of Au NPs on 3C-SiC/Si and Pt NPs on 3C-SiC/Si measured in 1.0 M KOH electrolyte. To clearly observe the onset potential at the current density of -1 mA/cm^2 of all the samples, (b) is the partial zoom-in image from -0.4 V vs. SCE to -1.6 V vs. SCE in (a). The dash and solid lines were collected in the dark and under the illumination of 100 mW/cm^2, respectively.

The catalytic effect of both the noble metals (Au and Pt) is evident. As shown in Figure 4.4b (partial zoom-in view in Figure 4.4a), the onset potential, defined at a current level of -1 mA/cm^2, is -1.50 V vs. SCE for the 3C-SiC/Si sample with no catalyst, and it is reduced to -1.40 and -0.76 V vs. SCE when using Au NPs (same onset potential value for Au NPs 1 and Au NPs 2 samples) or Pt NPs catalysts, respectively. The I-V characteristics are very reproducible from sample to sample (5–10 samples for each type), with deviations within ± 0.15 V. The samples without noble metal coverage (black solid line in Figure 4.4a) exhibit an average saturated current of 30 mA/cm^2 under 1 sun illumination. In the case of gold NPs on the surface, the sample Au NPs 1 (green solid line in Figure 4.4a) shows a lower value, 26 mA/cm^2, while the Au NPs 2 (blue solid line in Figure 4.4a) generates larger saturated current, up to 38 mA/cm^2. Similar value of the saturation current (~38 mA/cm^2) is found also with the photocathode with Pt NPs catalyst.

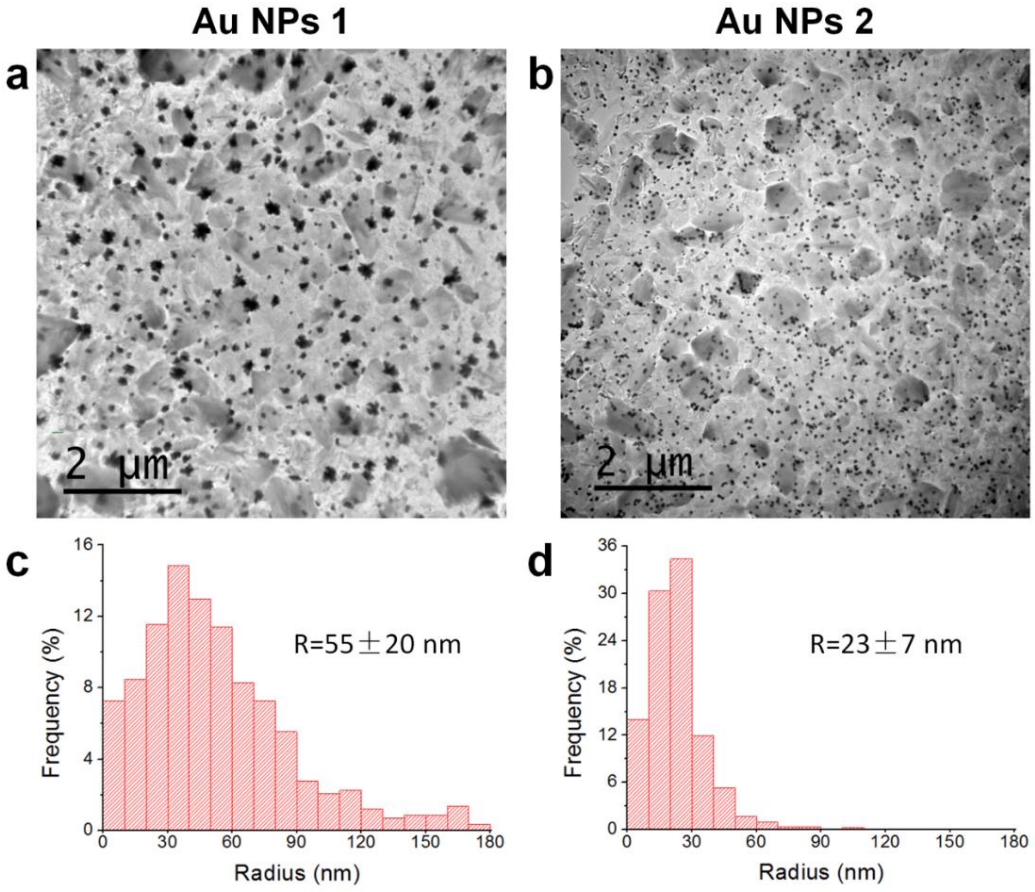

Figure 4.5 TEM micrograph in plan view of the 3C-SiC layer after deposition of Au: (a) Au NPs 1 by single immersion for 240 s; (b) Au NPs 2, by multiple immersions for a total immersion time of 180 s. Gold particles appear as black dots. (c) and (d) are the

grain size distributions of Au NPs 1 and Au NPs 2, obtained from statistical analyses of several images, as those shown in (a) and (b), respectively.

To understand why the two photocathodes with Au NPs on the surface show different activity, the morphological difference was characterized by plan view TEM technique. Figure 4.5a and b show plan view TEM micrographs of the as-prepared Au NPs 1 and Au NPs 2 samples, respectively. And the Au NPs are visible as black dots. The Au covered areas in the two samples analyzed by digital micrograph software are similar, around 10% and 7% for NPs 1 and NPs 2, respectively. The nanoparticles size, however, is very different. The Au NPs 1 sample fabricated by single immersion for 240 s shows a broad size distribution, characterized by the presence of very large particles, with an average particle radius of 55 nm and a standard deviation of 20 nm (see Figure 4.5c). On the contrary, the Au NPs 2 sample fabricated by three-step immersion for total 180 s shows a tight size distribution with average NP radius of 23 nm with a 7 nm standard deviation, as shown in Figure 4.5d.

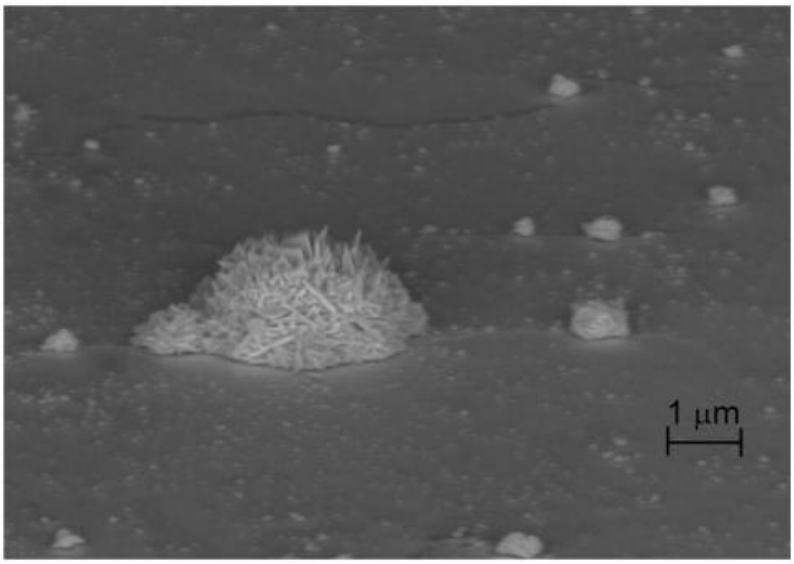

Figure 4.6 SEM micrograph in tilted view of Au grains in the Au NPs 1 sample. Typical flower-like shape can be observed, as well as small grains.

The larger Au grains in the Au NPs 1 sample exhibit typical flower-like shape, as shown by the SEM micrograph in tilted view, reported in Figure 4.6. This is due to the preferential growth on already nucleated Au grains,[209] which give rise to 3D nanostructures. Considering the spread of the grain size distribution, to have a good

statistical evaluation of the average equivalent thickness of the deposited metal, we also performed Rutherford Backscattering Spectrometry (RBS) analyses.[208] Compared to the microscopic techniques, this technique allows analyzing large areas, and from this we evaluated an average equivalent thickness of deposited metal of 65 nm. Such a value is quite high, related to the presence of relatively large and thick Au grains, large enough to locally shadow the light, which therefore cannot be absorbed by the Si to produce photocurrent. This explains why in the Au NPs 1 sample, despite the Au grains are effective in reducing the onset potential, the saturated photocurrent is lower than that in Au NPs 2. The decreased photocurrent is due to the presence of the large and thick Au grains which essentially produce a shadowing effect. In fact, from the TEM micrographs the percentage of covered area is about 10%, and this decrease is consistent with the observed decrease of the saturated photocurrent on Au NPs 1, also about equal to 10%.

On the contrary, in Au NPs 2 sample only small size particles can be observed, as shown by the plan view TEM micrograph in Figure 4.5b and the High resolution TEM micrograph in Figure 4.7 appearing as black dots.

In terms of the Pt NPs sample, the morphology is shown in the TEM micrographs of Figure 4.8a and b, corresponding to plan and cross-sectional view, respectively. Pt NPs are almost homogeneously deposited on the surface of SiC. The average particle size is around 3 nm and the aspect ratio is close to 1. The coverage of Pt NPs on 3C-SiC obtained from the plan view TEM image of Figure 4.8a is slightly less than 30%. Also, with the deposition time increasing, the transmittance of Pt NPs layer obviously decreased, as measured by a PVE300 Bentham System equipped with a 450 W Xenon lamp and 300 mm focal length monochromator The transmittance of the Pt nanoparticles (deposited under the current of 20 μA for 20 s by magnetron sputtering) is about 80%, calculated from the characterization of different deposition time of Pt on glass (see Figure 4.9).

Noble metal NPs are characterized by surface plasmon resonance that depends on their size, as well explained by the Mie theory of light scattering from metal nanoparticles.[210,211] We previously showed that electroless deposited Au nanoparticles on 3C-SiC exhibit plasmonic surface resonance in the visible range.[208] In particular, a clear broad peak in the reflectance spectrum of Au nanoparticle covered 3C-SiC was observed. Such peak corresponds to the occurrence of the Fröhlich condition of resonance, in which the nanoparticle polarization has a resonant

enhancement. The resonance depends on the nanoparticle size and we observed a red shift of the resonance as the size of the Au nanoparticles deposited on 3C-SiC increases.[208]

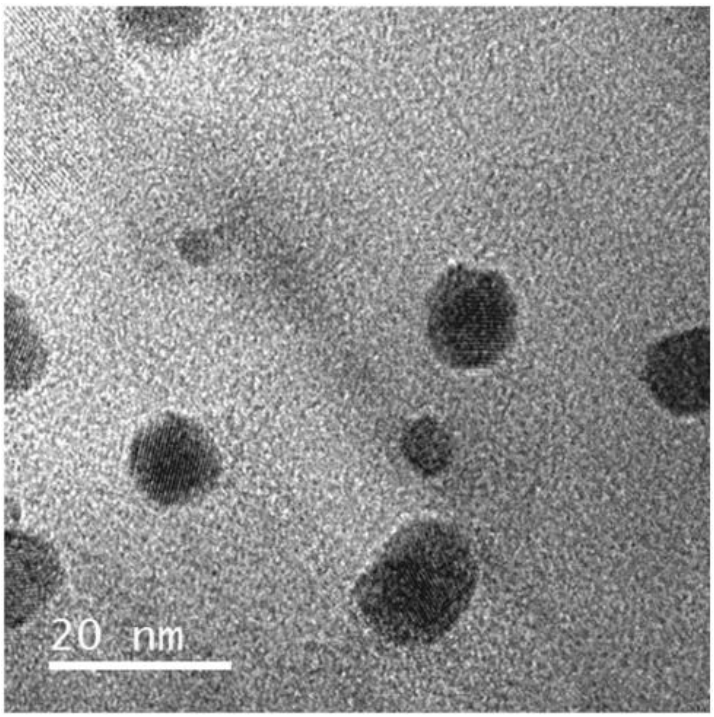

Figure 4.7 High resolution TEM micrograph with plan view of small Au grains on the surface of 3C-SiC in the Au NPs 2 sample.

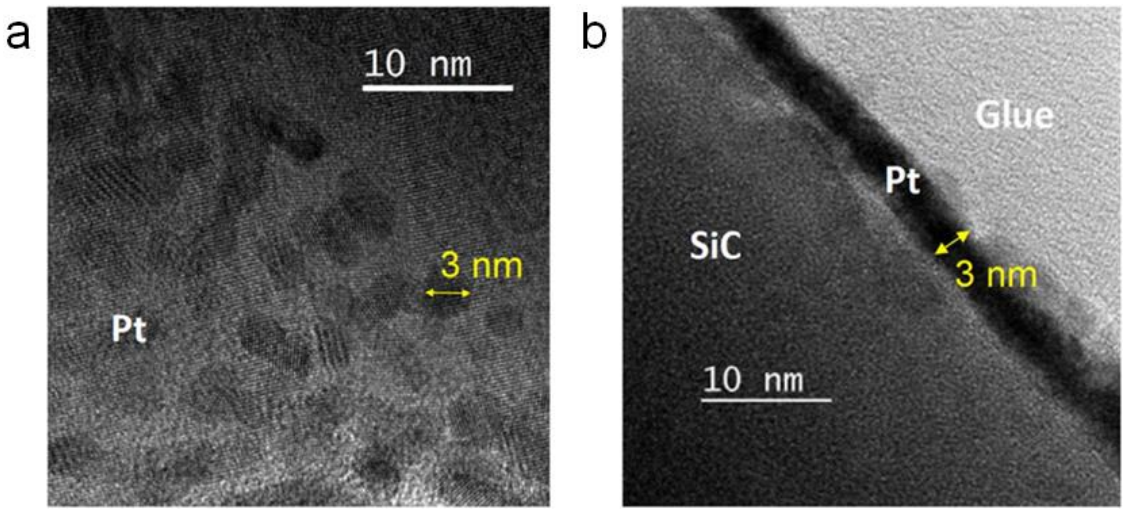

Figure 4.8 TEM images of the sample with Pt NPs on the surface of 3C-SiC deposited by magnetron sputtering, observed in plan view (a) and cross section (b). The size of Pt NPs is ~3 nm.

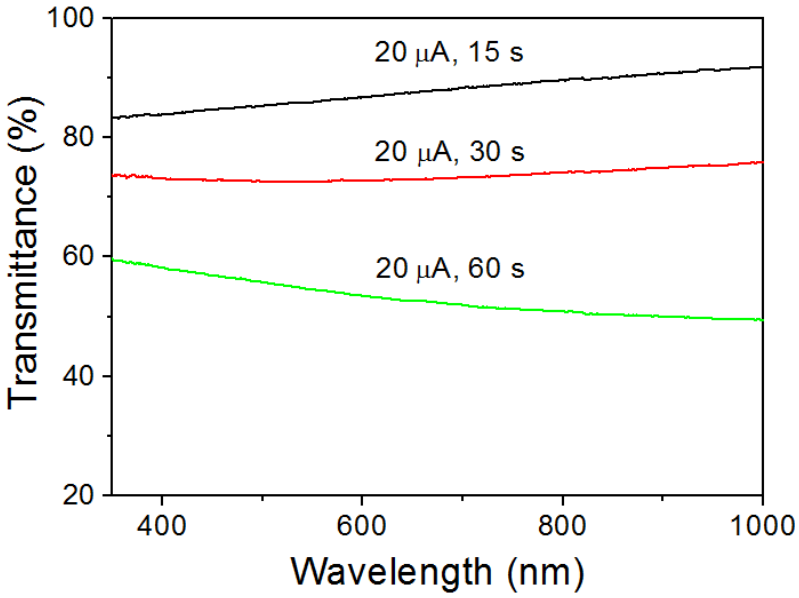

Figure 4.9 Transmittance measurements of Pt NPs layer deposited on glass by magnetron sputtering under different conditions. Black, red and green solid lines stand for the transmittance of Pt NPs deposited under the current of 20 μA for 15 s, 30 s and 60 s, respectively. According to the trend that the deposition time longer, the transmittance lower, the transmittance of Pt NPs deposited under the current of 20 μA for 20 s should be between the values from deposition condition of 15 s and 30 s, about 80%.

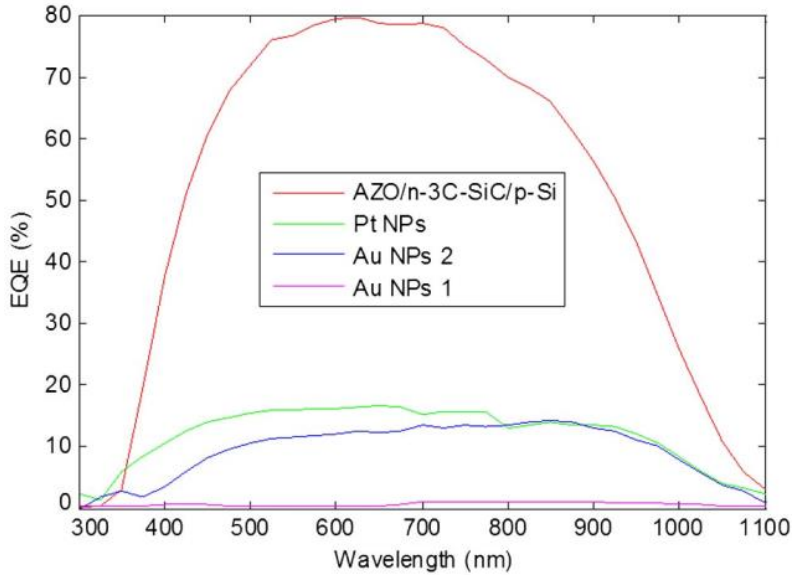

Figure 4.10 External quantum efficiency of AZO/n-3C-SiC/p-Si, Pt NPs sample, Au NPs 2 and Au NPs 1 samples, corresponding to the red, green, blue and magenta lines, respectively.

Additional evidence that the increased saturation current found in the Au NPs 2 and also in the Pt NPs sample is likely due to plasmonic effects is given by the measurements of external quantum efficiency (EQE) spectra in these samples. In order to decouple the plasmonic effects from the catalytic effects we performed the EQE measurements with no electrolyte solution. Without the electrolyte solution, that provides a good electrical contact, to measure the photocurrent as a function of pump wavelength a transparent top contact with low series resistance is crucial. This can be, for example, a transparent conductive oxide (TCO). For this purpose, to measure the EQE of the n-3C-SiC/p-Si cell, we deposited an AZO film by magnetron sputtering on top of the 3C-SiC layer. In the case of the samples covered with the Pt or Au metallic nanoparticles such TCO deposition has not been done to avoid strong damage and/or modifications of the metal nanoparticles during the sputtering process. For these samples as top contact we simply relied on the layer of metal nanoparticles. Figure 4.10 compares the EQE measured in the AZO/n-3C-SiC/p-Si reference cell and in the cells without TCO, covered by Pt or Au NPs. The reference cell (AZO/n-3C-SiC/p-Si) without NPs has a maximum EQE value of 80%, while lower values are measured for the NPs decorated samples (Pt NPs/n-3C-SiC/p-Si, Au NPs 1/n-3C-SiC/p-Si and Au NPs 2/n-3C-SiC/p-Si). Since with the NPs the surface coverage is relatively low (less than 10% for Au and less than 30% for Pt), close or below to the percolation threshold for horizontal electrical conduction, the series resistance is high. So, the charge collection is not optimal and a lower photocurrent is measured, obtaining lower values in the EQE. This detrimental effect is present in the EQE measurement but it does not occur when the cells with NPs are used as photocathodes for PEC measurements, since in this case a very good electrical contact is ensured by the electrolyte solution (1.0 M KOH). Despite the absolute EQE value is affected by the high series resistance, this measurement gives information on the dependence of the photocurrent on the wavelength, giving insights on the effects responsible for the observed improvement in the water splitting performance. The lowest EQE value is measured in the Au NPs 1 sample, characterized by a broad Au grains size distribution and by large and thick (65 nm in average) flower-like shaped grains. As already observed, such large grains shield the underlying Si from the incident light, therefore reducing the amount of photons that can be absorbed.

To better compare the shape and the wavelength dependence, Figure 4.11 shows the EQE characterization in arbitrary units of the two samples (Pt NPs/n-3C-SiC/p-Si, Au

NPs 2/n-3C-SiC/p-Si) exhibiting the higher saturated photocurrent. Their shapes are quite different: the Pt NPs and the Au NPs 2 samples have EQE spectra peaked in the ultraviolet (UV) region and in the infrared (IR) region, respectively. An evident increase of the EQE for the cell covered with Pt NPs is obviously observed in the UV region. On the contrary, the EQE of the reference n-3C-SiC/p-Si cell without NPs is peaked in the visible region from 600 nm to 700 nm (see Figure 4.10).

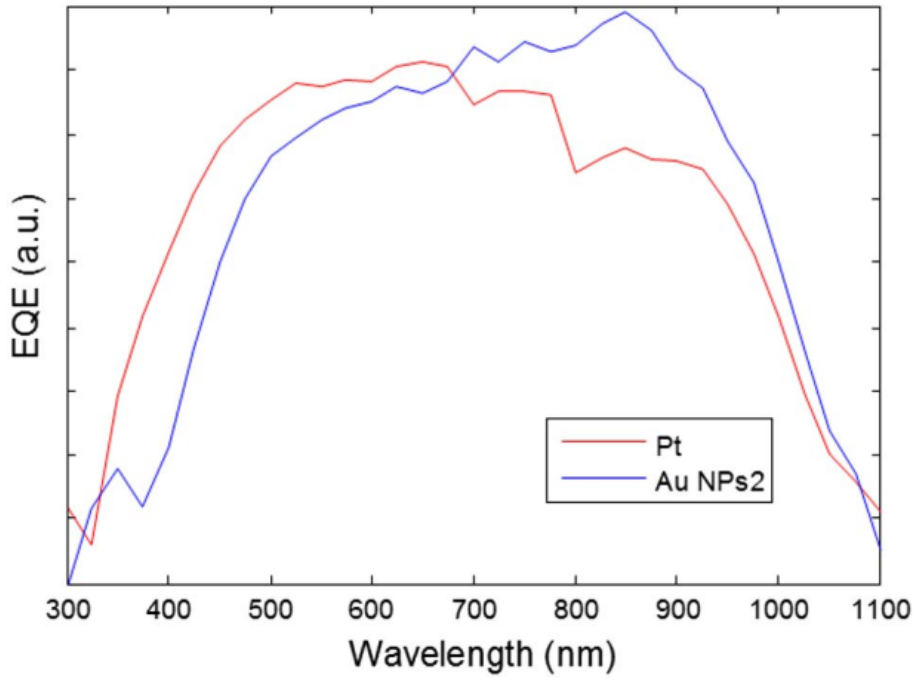

Figure 4.11 External quantum efficiency of the samples covered with Pt or Au NPs 2, corresponding to the red and blue lines, respectively.

These differences are well explained by the wavelength dependence of the Au and Pt localized plasmons. The plasmonic resonance peak of Au nanoparticles with diameter of about 50 nm is known to occur at about 600 nm wavelength,[208,212-213] while in the case of Pt nanoparticles the resonance is at about 250 nm.[214-215] Hence, the EQE spectra of the Pt NPs sample in Figure 4.11 are peaked in correspondence with the plasmonic resonances of the respective metallic nanoparticles. This supports the conclusion that in such samples the plasmonic resonances of the Au and Pt nanoparticles produce a relevant EQE enhancement, and therefore, a higher saturated photocurrent when the samples are illuminated by the broad solar spectrum. Furthermore, considering the cross section of the plasmon decay pathway, according to

the previous report, it is known that both Pt disks with radius smaller than 210 nm,[214] as well as spherical Au particles with radius smaller than 50 nm (as in the Au NPs 2 sample) have larger cross section for plasmon resonance energy transfer (PRET) through non-radiative processes and hot electrons production, compared to the light scattering cross section.[214] This suggests that PRET and hot electrons are the plasmonic effects responsible for the larger saturation current observed in the Pt NPs and Au NPs 2 samples. On the contrary, the large Au grains obtained in the Au NPs 1 sample produce random light scattering, which may be useful for light trapping into the semiconductor, but it is likely overwhelmed by the above mentioned shadowing effect.

In summary, considering both the onset voltage reduction and the current increase, compared to the photocathodes with Au NPs, the Pt NPs sample appears to be very efficient for both processes. Furthermore, as shown in Figure 4.4a with red solid line, the saturated current of the Pt NPs photocathode is reached at -0.82 V vs. RHE, and at 0 V vs. RHE the current density is ~13 mA/cm^2. Such a result is not achievable with a Pt electrode, but it is obtained thanks to the open circuit voltage of the solar cell.

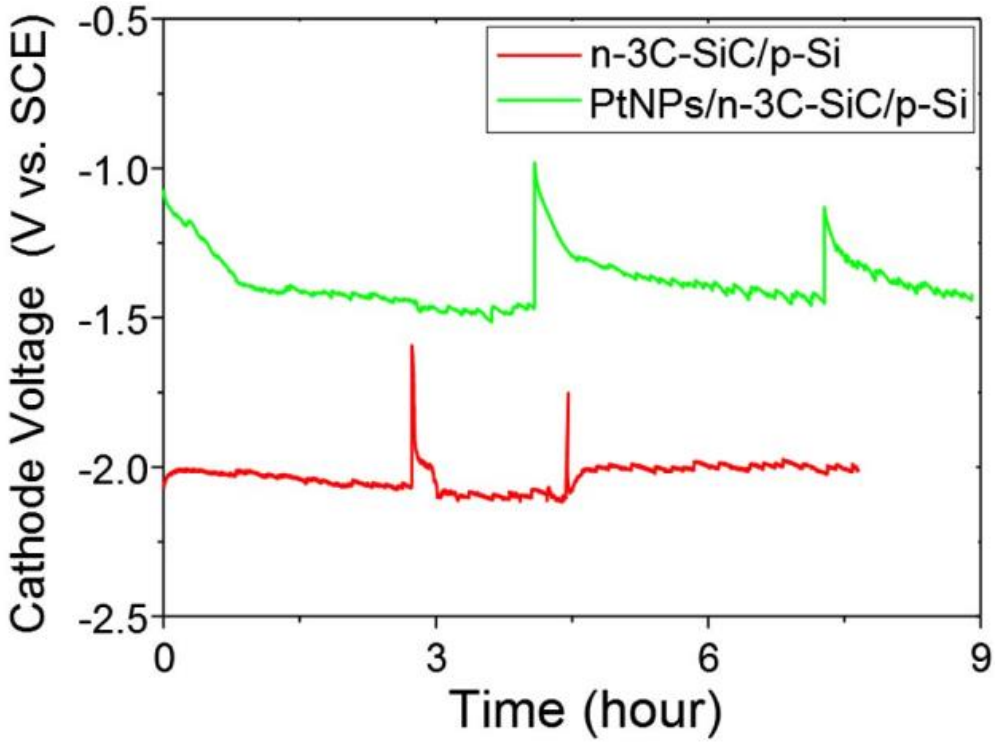

Figure 5.12 Voltage vs. time (V-t) test collected using a photocathode n-3C-SiC/p-Si or Pt NPs/n-3C-SiC/p-Si in 1.0 M KOH electrolyte under 1 sun illumination while producing hydrogen with a current density of 12 mA/cm^2.

We then tested the stability of the Pt NPs photocathodes in 1.0 M KOH electrolyte solution by measuring the voltage as a function of time under continuous DC operation at the current density of 12 mA/cm^2. Figure 4.12 shows the V-t plots and compares the sample with Pt NPs to the bare n-3C-SiC/p-Si photocathode. The stress measurements were briefly interrupted (after ~4 h and ~7 h for the bare sample without catalyst, and after ~2.8 h and ~4.5 h for the sample with Pt NPs) to collect I-V trace measurements. The V-t curves show ripples with a frequency of one on every ~10 min, attributed to the formation of bubbles on top of the photocathodes. The photocathodes appear quite stable, although they exhibit a transient in correspondence with each stress off/on time. During this transient the voltage increases and it reaches a plateau in ~1 h. The reason of such transient is still unclear and further study in deep to understand its origin is expected.

4.4. Conclusions

In conclusion, in this chapter we employed a Si-based PEC cell covered by n-type 3C-SiC as photocathode for hydrogen production in 1.0 M KOH electrolyte solution. The 3C-SiC layer is employed as emitter and silicon protection layer. The hydrogen evolution reaction on the surface shows a high saturated photocurrent, of about 30 mA/cm^2. Noble metal (Au or Pt) nanoparticles deposited on 3C-SiC are effective in reducing the onset potential. By properly tuning the size, shape and density of the nanoparticles, the plasmonic properties can also be enhanced, obtaining an increase of the saturated current up to 38 mA/cm^2, i.e. very close to the physical limit for silicon at AM 1.5G (100 mW/cm^2). Long PEC stability, without any appreciable decay in 1.0 M KOH under 1 sun illumination for 9 h at 12 mA/cm^2 is demonstrated on Pt NPs/n-3C-SiC/p-Si photocathodes.

Chapter 5:
Conclusions and perspectives

In conclusion, during this PhD thesis I have learned how to grow high quality metal/metal oxide thin films via physical vapor deposition methods including magnetron sputtering, e-beam evaporation, thermal evaporation and ALD, as well the electrochemical deposition using a potentiostat. In my research, the photoelectrochemical analysis is one of the most important characterization methods. I have learned how to build/assemble the configurations for various solar-driven water splitting devices, and I have obtained lots of experiences from basic analyses to better understand on metal/metal oxides or photoelectrodes. Moreover, I also have learned how to analyze the samples by a series of morphological, topographical, electrical, mechanical and chemical characterizations at nano and microscale through AFM, SEM, EDX, TEM, and XPS, and even perform the electrical property by a probestation and a PVE300 Bentham System at the device scale.

In the first part of my thesis I have investigated the ageing mechanisms of Ni-based n-Si photoanodes in 1.0 M KOH (pH 14) electrolyte for light-driven oxygen evolution reaction at nano and atomic scales. My experiments indicate that:

- The ageing mechanisms of Ni/SiO_X/n-Si/Ti photoanodes depend on the thickness of Ni layers. The photoanodes with a thinner Ni coating resulted in a higher solar cell activity yet short stability.
- The failure of the samples coated with a 2 nm thick layer of nickel within 18 hours was due to the formation of a thick interfacial SiO_X film, which blocks hole/electron transfer to the electrolyte/substrate, and also the extensive penetration of potassium impurities into the NiO_X layer.
- The photoanodes with the 5 nm and 10 nm thick nickel layers showed stable currents under a constant potential for more than 150 and 260 hours, respectively. The degradation of these samples was due to the formation of many holes in the active NiO_X layer, and the size/density of holes relied on the thickness of the NiO_X layer.

- By combining TEM and EELS techniques, the potassium contamination in the NiO_X film could be detected, which was masked in the XPS profiles, indicating that previous reports observed by traditional characterization tools with low spatial resolution in the field of water splitting may be ignoring essential degradation phenomena. These findings revealing essential information may be of interest to the researchers for studying the lifetime enhancement of water splitting solar cells.

After understanding the degradation process of Ni based n-Si photoanodes for PEC water splitting, I decided to study the effect of electrolytes to enhance the performance of the photoanodes. 5 nm Ni-based n-Si photoanodes for PEC water splitting has been analyzed in four different alkaline electrolytes. My main achievements are:

- As for the activity, the onset potential of the photoanodes for water oxidation shows the trend of $V_{ON,\ pH\ 14} < V_{ON,\ pH\ 12.5} < V_{ON,\ pH\ 9.5}$. The photoanodes at pH 9.5 with Li ions and pH 12.5 need an overpotential of 0.243 V and 0.024 V for water splitting, respectively. However, the onset potential of the photoanode at pH 14 shows to be 0.039 V more cathodic than the thermal dynamic potential for water oxidation.
- As for the stability test, the photoanodes showed much more stable at pH 9.5 and 12.5 (both with Li ions) than at pH 14, mainly thanks to the presence of Li ions in the electrolytes, and they still stayed stable potential after 264 h P–t PEC tests under the constant current density of 10 mA/cm^2.
- Considering both the activity and stability, 5 nm Ni based n-Si photoanodes show the best OER performance at pH 12.5 electrolyte. In general, tuning the chemical composition of the electrolyte is an inexpensive and effective method to improve the performance of Ni-coated n-Si photoanodes for PEC water splitting. Future works should explore that this approach may also be useful to enhance the performance of other metal-coated photoelectrodes for water splitting, not only for OER but also for HER.

Finally, we also studied the photocathodes consisting of n-3C-SiC/p-Si decorated with noble metal nanoparticles (e.g. Au, Pt) for HER in 1.0 M KOH (pH 14) electrolyte. The main conclusions of this work are:

- The n-type 3C-SiC layer was used as emitter and silicon protection layer. 3C-SiC/Si photocathode showed a high saturated photocurrent of about 30 mA/cm^2, and in 7.5 h, the photocathode revealed the good stability for HER.
- Noble metal nanoparticles deposited on the surface of 3C-SiC are effective in reducing the onset potential. By properly tuning the size, shape and density of the Au or Pt nanoparticles, the plasmonic properties can also be enhanced, obtaining a high saturated current of about 38 mA/cm^{-2}, very close to the physical limit for silicon at AM 1.5G (1sun). And Pt NPs/n-3C-SiC/p-Si photocathode showed long PEC stability without any appreciable decay for 9 h in KOH electrolyte.

By making use of sufficient sunlight, PEC water splitting solar cells have provided a promising way to produce sustainable hydrogen energy without contamination under combustion. A great deal of advanced nanostructured materials have been exploited as catalysts for photoanodes or photocathodes. However, to carry out OER or HER, apart from the sunlight, extra potential usually has to be applied to overcome the overpotential of the electrodes. Our goal is to assemble water splitting tandem cells, which could produce H_2 and O_2 only under the illumination of sun. In this case, it's essential to consider light absorption and energy band matching of different photoelectrodes for enhanced conversion efficiency. Future works should promote the performance of semiconductor materials, find new materials, develop advanced electrolyte and optimize the configuration, among others. In addition, the combination of high resolution TEM and EELS techniques could provide detailed information for researchers to understand the mechanisms of the photoelectrodes and obtain improvement for PEC performance. Furthermore, in order to meet the living demands of human with a friendly environment, scalable solar-driven water splitting devices are expected to be achieved for H_2 generation.

References

[1] International Energy Agency (IEA), Global energy and CO_2 status report **2018**.

[2] BP, Statistical Review of World Energy **2019**, 68th edition.

[3] International Energy Agency (IEA), Energy and air pollution, World Energy Outlook special report, **2016**.

[4] The 2° institute, https://www.co2levels.org/#sources

[5] Goddard Space Flight Center of National Aeronautics and Space Administration (NASA), https://www.giss.nasa.gov/research/news/20190523/.

[6] World Health Organization (WHO), 9 out of 10 people worldwide breathe polluted air, but more countries are taking action, **2018**.

[7] World Health Organization (WHO), Ambient (outdoor) air pollution, **2018**.

[8] U.S. Energy Information Administration, International Energy Outlook **2019**, https://www.eia.gov/ieo.

[9] R. E. Blankenship, D. M. Tiede, J. Barber, G. W. Brudvig, G. Fleming, M. Ghirardi, M. R. Gunner, W. Junge, D. M. Kramer, A. Melis, T. A. Moore, C. C. Moser, D. G. Nocera, A. J. Nozik, D. R. Ort, W. W. Parson, R. C. Prince, R. T. Sayre, Comparing photosynthetic and photovoltaic efficiencies and recognizing the potential for improvement. *Science* **2011**, *332*, 805.

[10] M. G. Walter, E. L. Warren, J. R. McKone, S. W. Boettcher, Q. Mi, E. A. Santori, N. S. Lewis, Solar water splitting cells. *Chemical Reviews* **2010**, *110*, 6446.

[11] N. S. Lewis, Toward cost-effective solar energy use. *Science* **2007**, *315*, 798.

[12] A. Fujishima, K. Honda, Electrochemical photolysis of water at a semiconductor electrode. *Nature* **1972**, *238*, 37.

[13] C.-H. Liao, C.-W. Huang, J. C. S. Wu, Hydrogen production from semiconductor-based photocatalysis via water splitting. *Catalysts* **2012**, *2*, 490.

[14] T. Bak, J. Nowotny, M. Rekas, C. C. Sorrell, Photo-electrochemical hydrogen generation from water using solar energy. Materials-related aspects, *International Journal of Hydrogen Energy* **2002**, *27*, 991.

[15] X. An, T. Li, B. Wen, J. Tang, Z. Hu, L. M. Liu, J. Qu, C. Huang and H. Liu, New insights into Defect-mediated heterostructures for photoelectrochemical water splitting, *Advanced Energy Materials* **2016**, *6*, 1502268.

[16] C. Jiang, S. J. A. Moniz, A. Wang, T. Zhang, J. Tang, Photoelectrochemical

devices for solar water splitting - materials and challenges. *Chemical Society Review*, **2017**, *46*, 4645.

[17] P. Peerakiatkhajohn, J.-H. Yun, S. Wang, L. Wang, Review of recent progress in unassisted photoelectrochemical water splitting: from material modification to configuration design. *Journal of Photonics for Energy* **2016**, *7*, 012006.

[18] D. Li, J. Zheng, X. Chen, Z. Zou, The study on photocatalytic water splitting system and materials. *Progress in Chemistry*, **2007**, *19 (4)*, 464.

[19] G. Zheng, Solar energy-driven photoelectrochemical conversion using earth-abundant materials, TeraWatts, TeraGrams, TeraLiters Workshop on Challenges and Opportunities for Sustainable Production of Chemicals and Fuels beyond the Shale Gale, **2015**.

[20] M. Ni, M. K. H. Leung, D. Y. C. Leung, K. Sumathy, A review and recent developments in photocatalytic water splitting using TiO_2 for hydrogen production. *Renewable and Sustainable Energy Reviews* **2007**, *11 (3)*, 401. https://doi.org/10.1016/j.rser.2005.01.009.

[21] J. Tian, Z. Zhao, A. Kumar, R. I. Boughton, H. Liu Recent progress in design, synthesis, and applications of one dimensional TiO_2 nanostructured surface heterostructures: A review. *Chemical Society Reviews* **2014**, *43 (20)*, 6920. https://doi.org/10.1039/C4CS00180J.

[22] C. Santato, M. Odziemkowski, M. Ulmann, J. Augustynski, Crystallographically oriented mesoporous WO_3 films: synthesis, characterization, and applications. *Journal of the American Chemical Society* **2001**, *123*, 10639.

[23] J. A. Seabold and K.-S. Choi, Effect of a cobalt-based oxygen evolution catalyst on the stability and the selectivity of photo-oxidation reactions of a WO_3 photoanode. *Chemistry of Materials* **2011**, *23*, 1105–1112.

[24] J. C. Hill, K.-S. Choi, Effect of electrolytes on the selectivity and stability of n-type WO_3 photoelectrodes for use in solar water oxidation. *The Journal of Physical Chemistry C* **2012**, *116*, 7612.

[25] K. Sivula, F. Le Formal, and Grätzel M. Solar water splitting: Progress using hematite (α-Fe_2O_3) photoelectrodes. *ChemSusChem* **2011**, *4 (4)*, 432. https://doi.org/10.1002/cssc.201000416.

[26] P. Sharma, J.-W. Jang, and J. S. Lee, Key Strategies to Advance the Photoelectrochemical Water Splitting Performance of α-Fe_2O_3 Photoanode, *ChemCatChem* **2019**, *11*, 157.

[27] M. S. Islam, M. F. Hossain, S. M. A. Razzak Enhanced photoelectrochemical performance of nanoparticle ZnO photoanodes for water-splitting application. *Journal of Photochemistry and Photobiology A: Chemistry* **2016**, *326*, 100. https://doi.org/10.1016/j.jphotochem.2016.04.002.

[28] S. B. A. Hamid, S. J. Teh, C. W. Lai, Photocatalytic water oxidation on ZnO: A review. *Catalysts* **2017**, *7*, 93. https://doi.org/10.3390/catal7030093.

[29] Y. Park, K. J. McDonald, K.-S. Choi, Progress in bismuth vanadate photoanodes for use in solar water oxidation. *Chemical Society Reviews* **2013**, *42 (6)*, 2321. https://doi.org/10.1039/C2CS35

[30] T. W. Kim, K.-S. Choi, Nanoporous $BiVO_4$ photoanodes with dual-layer oxygen evolution catalysts for solar water splitting, *Science* **2014**, *343*, 990.

[31] X. Feng, T. J. LaTempa, J. I. Bastiam, G. K. Mor, O. K. Varghese, C. A. Grimes, Ta_3N_5 nanotube arrays for visible light water photoelectrolysis. *Nano Letters* **2010**, *10 (3)*, 948. https://doi.org/10.1021/nl903886e.

[32] A. Dabirian, R. Van De Krol, High-temperature ammonolysis of thin film Ta_2O_5 photoanodes: Evolution of structural, optical, and photoelectrochemical properties. *Chemistry of Materials* **2015**, *27 (3)*: 708.

[33] R. Abe, M. Higashi, K. Domen, Facile fabrication of an efficient oxynitride TaON photoanode for overall water splitting into H_2 and O_2 under visible light irradiation. *Journal of the American Chemical Society* **2010**, *132 (34)*, 11828. https://doi.org/10.1021/ja1016552.

[34] M. Higashi, K. Domen, R. Abe, Highly stable water splitting on oxynitride TaON photoanode system under visible light irradiation. *Journal of the American Chemical Society* **2012**, *134 (16)*, 6968. https://doi.org/10.1021/ja302059g.

[35] A. Paracchino, V. Laporte, K. Sivula, M. Grätzel, E. Thimsen. Highly active oxide photocathode for photoelectrochemical water reduction. *Nature Materials* **2011**, *10*, 456. https://doi.org/10.1038/nmat3017.

[36] I. V. Bagal, N. R. Chodankar, M. A. Hassan, A. Waseem, M. A. Johar, D.-H. Kim, S.-W. Ryu, Cu_2O as an emerging photocathode for solar water splitting - A status review. *International Journal of Hydrogen Energy* **2019**, *44*, 21351.

[37] Y. Oh, W. Yang, J. Kim, S. Jeong, J. Moon, Enhanced photocurrent of transparent $CuFeO_2$ photocathodes by selflight-harvesting architecture. *ACS Applied Materials & Interfaces* **2017**, *9 (16)*, 14078.

[38] Z. Liu, X. Lu, D. Chen, Photoelectrochemical water splitting of $CuInS_2$

photocathode collaborative modified with separated catalysts based on efficient photogenerated electron-hole separation. *ACS Sustainable Chemistry & Engineering* **2018**, *6*, 10289.

[39] F. F. Abdi, T. J. Savenije, M. M. May, B. Dam, R. van de Krol, The origin of slow carrier transport in $BiVO_4$ thin film photoanodes: A time-resolved microwave conductivity study, *The Journal of Physical Chemistry Letters* **2013**, *4 (16)*, 2752.

[40] N. Guijarro, M. S. Prévot, K. Sivula, Surface modification of semiconductor photoelectrodes, *Physical Chemistry Chemical Physics* **2015**, *17 (24)*, 15655.

[41] R. Fan, Z. Mi, M. Shen, Silicon based photoelectrodes for photoelectrochemical water splitting, *Optics Express* **2019**, *27 (4)*, A51.

[42] B. Y. Alfaifi, H. Ullah, S. Alfaifi, A. A. Tahir, T. K. Mallick, Photoelectrochemical solar water splitting: From basic principles to advanced devices. *Veruscript Functional Nanomaterials* **2018**, *2*, #BDJOC3.

[43] A. C. Nielander, M. R. Shaner, K. M. Papadantonakis, S. A. Francis, N. S. Lewis, A taxonomy for solar fuels generators, *Energy & Environmental Science* **2015**, *8 (1)*, 16.

[44] A. Currao, Photoelectrochemical water splitting, *Chimia* **2007**, *61 (12)*, 815.

[45] X.-T. Xu, L. Pan, X. Zhang, L. Wang, J.-J. Zou, Rational design and construction of cocatalysts for semiconductor-based photo-electrochemical oxygen evolution: A comprehensive review. *Advanced Science* **2019**, *6*, 1801505.

[46] N. S. Lewis, Light work with water, *Nature* **2001**, *414*, 589

[47] J. Oh, T. G. Deutsch, H.-C. Yuan, H. M. Branz, Nanoporous black silicon photocathode for H_2 production by photoelectrochemical water splitting. *Energy & Environmental Science* **2011**, *4 (5)*, 1690.

[48] S. W. Boettcher, E. L. Warren, M. C. Putnam, E. A. Santori, D. Turner-Evans, M. D. Kelzenberg, M. G. Walter, J. R. McKone, B. S. Brunschwig, H. A. Atwater, N. S. Lewis, Photoelectrochemical hydrogen evolution using Si microwire arrays. *Journal of the American Chemical Society* **2011**, *133 (5)*, 1216.

[49] M. J. Kenney, M. Gong, Y. Li, J. Z. Wu, J. Feng, M. Lanza, H. Dai, High-performance silicon photoanodes passivated with ultrathin nickel films for water oxidation. *Science* **2013**, *342*, 836.

[50] K. Sun, S. Shen, Y. Liang, P. E. Burrows, S. S. Mao, D. Wang, Enabling silicon for solar-fuel production. *Chemical Reviews* **2014**, *114*, 8662.

[51] I. A. Digdaya, G. W. P. Adhyaksa, B. J. Trześniewski, E. C. Garnett, W. A. Smith,

Interfacial engineering of metal-insulator-semiconductor junctions for efficient and stable photoelectrochemical water oxidation, *Nature Communicaitons* **2017**, *8,* 15968.

[52] S. Hu, M. R. Shaner, J. A. Beardslee, M. Lichterman, B. S. Brunschwig, N. S. Lewis, Amorphous TiO_2 coatings stabilize Si, GaAs, and GaP photoanodes for efficient water oxidation. *Science* **2014**, *344*, 1005.

[53] D. Bae, B. Seger, P. C. K. Vesborg, O. Hansen, I. Chorkendorff, Strategies for stable water splitting via protected photoelectrodes. *Chemical Society Reviews* **2017**, *46*, 1933.

[54] L. Ji, M. D. McDaniel, S. Wang, A. B. Posadas, X. Li, H. Huang, J. C. Lee, A. A. Demkov, A. J. Bard, J. G. Ekerdt, E. T. Yu, A silicon-based photocathode for water reduction with an epitaxial $SrTiO_3$ protection layer and a nanostructured catalyst. *Nature Nanotechnology* **2015**, *10*, 84.

[55] Hara M., Nunoshige J., Takata T., Kondo J. N., and Domen K. Unusual enhancement of H_2 evolution by Ru on TaON photocatalyst under visible light irradiation. *Chemical Communications* **2003**, *(24)*, 3000.

[56] M. Mikolasek, K. Frohlich, K. Husekova, J. Racko, V. Rehacek, F. Chymo, M. Tapajna, L. Harmatha, Silicon based MIS photoanode for water oxidation: A comparison of RuO_2 and Ni Schottky contacts. *Applied Surface Science* **2018**, *461*, 48.

[57] P. Dias, L. Andrade, A. Mendes, Hematite-based photoelectrode for solar water splitting with very high photovoltage, *Nano Energy* **2017**, *38*, 218.

[58] L. Ouattara, S. Fierro, O. Frey, M. Koudelka, C. Comninellis, Electrochemical comparison of IrO_2 prepared by anodic oxidation of pure iridium and IrO_2 prepared by thermal decomposition of H_2IrCl_6 precursor solution. *Journal of Applied Electrochemistry* **2009**, *39*, 1361.

[59] Y. W. Chen, J. D. Prange, S. Dühnen, Y. Park, M. Gunji, C. E. D. Chidsey, P. C. McIntyre, Atomic layer-deposited tunnel oxide stabilizes silicon photoanodes for water oxidation. *Nature Materials* **2011**, *10*, 539.

[60] A. G. Scheuermann, J. D. Prange, M. Gunji, C. E. D. Chidsey, P. C. McIntyre, Effects of catalyst material and atomic layer deposited TiO_2 oxide thickness on the water oxidation performance of metal–insulator–silicon anodes. *Energy & Environmental Science* **2013**, *6*, 2487.

[61] B. Mei, B. Seger, T. Pedersen, M. Malizia, O. Hansen, I. Chorkendorff, P. C. K.

Vesborg, Protection of p^+-n-Si photoanodes by sputter-deposited Ir/IrO_X thin films. *The Journal of Physical Chemistry Letters* **2014**, *5*, 1948-1952.

[62] V. Pfeifer, T. E. Jones, J. J. Velasco Vélez, R. Arrigo, S. Piccinin, M. Hävecker, A. Knop-Gericke, R. Schlögl, In situ observation of reactive oxygen species forming on oxygen-evolving iridium surfaces. *Chemical Science (Camb.)* **2017**, *8 (3)*, 2143.

[63] L. Gao, Q. Li, H. Chen, S. Hayase, T. Ma, In situ fabrication of nanoepitaxial TiO_2 protection layer on Si substrate: hole chemical conduction instead of tunneling effect. *Solar RRL* **2017**, *1 (8)*, 1700064.

[64] T. Yao, R. Chen, J. Li, J. Han, W. Qin, H. Wang, J. Shi, F. Fan, and C. Li, Manipulating the tnterfacial energetics of n-type silicon photoanode for efficient water oxidation. *Journal of the American Chemical Society* **2016**, *138 (41)*, 13664.

[65] S. Oh, J. Oh, High performance and stability of micropatterned oxide-passivated photoanodes with local catalysts for photoelectrochemical water splitting. *The Journal of Physical Chemistry C* **2016**, *120 (1)*, 133.

[66] Y. Shi, T. Han, C. Gimbert-Suriñach, X. Song, M. Lanza, A. Llobet, Substitution of native silicon oxide by titanium in Ni-coated silicon photoanodes for water splitting solar cells. *Journal of Materials Chemistry A* **2017**, *5*, 1996.

[67] Q. Cai, W. Hong, C. Jian, J. Li, W. Liu, Impact of silicon resistivity on the performance of silicon photoanode for efficient water oxidation reaction. *ACS Catalysis* **2017**, *7 (5)*, 3277.

[68] C. Li, Y. Xiao, L. Zhang, Y. Li, J.-J. Delaunay, H. Zhu, Efficient photoelectrochemical water oxidation enabled by an amorphous metal oxide-catalyzed graphene/silicon heterojunction photoanode. *Sustainable Energy & Fuels* **2018**, *2 (3)*, 663.

[69] M. R. Shaner, S. Hu, K. Sun, N. S. Lewis, Stabilization of Si microwire arrays for solar-driven H_2O oxidation to O_2(g) in 1.0 M KOH(aq) using conformal coatings of amorphous TiO_2. *Energy & Environmental Science* **2015**, *8 (1)*, 203.

[70] K. Sun, N. Park, Z. Sun, J. Zhou, J. Wang, X. Pang, S. Shen, S. Y. Noh, Y. Jing, S. Jin, P. K. L. Yu, D. Wang, Nickel oxide functionalized silicon for efficient photo-oxidation of water. *Energy & Environmental Science* **2012**, *5*, 7872.

[71] K. Sun, M. T. McDowell, A. C. Nielander, S. Hu, M. R. Shaner, F. Yang, B. S. Brunschwig, N. S. Lewis, Stable solar-driven water oxidation to O_2(g) by

Ni-oxide-coated silicon photoanodes. *The Journal of Physical Chemistry Letters* **2015**, *6*, 592.

[72] S. Yoon, J.-H. Lim, B. Yoo, Efficient Si/SiOx/ITO heterojunction photoanode with an amorphous and porous NiOOH catalyst formed by $NiCl_2$ activation for water oxidation. *Electrochimica Acta* **2017**, *237*, 37.

[73] G. Xu, Z. Xu, Z. Shi, L. Pei, S. Yan, Z. Gu, Z. Zou, Silicon photoanodes partially covered by Ni@$Ni(OH)_2$ core-shell particles for photoelectrochemical water oxidation. *ChemSusChem* **2017**, *10 (14)*, 2897.

[74] X. Zhou, R. Liu, K. Sun, D. Friedrich, M. T. McDowell, F. Yang, S. T. Omelchenko, F. H. Saadi, A. C. Nielander, S. Yalamanchili, K. M. Papadantonakis, B. S. Brunschwig, N. S. Lewis, Interface engineering of the photoelectrochemical performance of Ni-oxide-coated n-Si photoanodes by atomic-layer deposition of ultrathin films of cobalt oxide. *Energy & Environmental Science* **2015**, *8 (9)*, 2644.

[75] J. H. Yang, K. Walczak, E. Anzenberg, F. M. Toma, G. Yuan, J. Beeman, A. Schwartzberg, Y. Lin, M. Hettick, A. Javey, J. W. Ager, J. Yano, H. Frei, I. D. Sharp, Efficient and sustained photoelectrochemical water oxidation by cobalt oxide/silicon photoanodes with nanotextured interfaces, *Journal of the American Chemical Society* **2014**, *136*, 6191.

[76] J. Yang, J. K. Cooper, F. M. Toma, K. A. Walczak, M. Favaro, J. W. Beeman, L. H. Hess, C. Wang, C. Zhu, S. Gul, J. Yano, C. Kisielowski, A. Schwartzberg, and I. D. Sharp, A multifunctional biphasic water splitting catalyst tailored for integration with high-performance semiconductor photoanodes. *Nature Materials* **2017**, *16 (3)*, 335.

[77] K. Jun, Y. S. Lee, T. Buonassisi, J. M. Jacobson, High photocurrent in silicon photoanodes catalyzed by iron oxide thin films for water oxidation. *Angewandte Chemie International Edition* **2012**, *51*, 423.

[78] N. C. Strandwitz, D. J. Comstock, R. L. Grimm, A. C. NicholsNielander, J. Elam, N. S. Lewis, Photoelectrochemical behavior of n-type Si(100) electrodes coated with thin films of manganese oxide grown by atomic layer deposition. *The Journal of Physical Chemistry C* **2013**, *117*, 4931.

[79] B. Guo, A. Batool, G. Xie, R. Boddula, L. Tian, S. U. Jan, J. R. Gong, Facile integration between Si and catalyst for high-performance photoanodes by a multifunctional bridging layer. *Nano Letters* **2018**, *18 (2)*, 1516.

[80] X. Yu, P. Yang, S. Chen, M. Zhang, G. Shi, NiFe alloy protected silicon photoanode for efficient water splitting. *Advanced Energy Materials* **2017**, *7 (6)*, 1601805.

[81] S. Oh, H. Song, J. Oh, An optically and electrochemically decoupled monolithic photoelectrochemical cell for high-Performance solar-driven water splitting," *Nano Letters* **2017**, *17 (9)*, 5416.

[82] L. Chen, J. Yang, S. Klaus, L. J. Lee, R. Woods-Robinson, J. Ma, Y. Lum, J. K. Cooper, F. M. Toma, L. W. Wang, I. D. Sharp, A. T. Bell, J. W. Ager, p-type transparent conducting oxide/n-type semiconductor heterojunctions for efficient and stable solar water oxidation, *Journal of the American Chemical Society* **2015**, *137 (30)*, 9595.

[83] C. Ros, N. M. Carretero, J. David, J. Arbiol, T. Andreu, J. R. Morante, Insight into the degradation mechanisms of atomic layer deposited TiO_2 as photoanode protective layer. *ACS Applied Materials & Interfaces* **2019**, *11*, 29725.

[84] R. Fan, W. Dong, L. Fang, F. Zheng, X. Su, S. Zou, J. Huang, X. Wang, M. Shen, Stable and efficient multi-crystalline n^+p silicon photocathode for H_2 production with pyramid-like surface nanostructure and thin Al_2O_3 protective layer. *Applied Physical Letters* **2015**, *106 (1)*, 013902.

[85] R. Fan, J. Min, Y. Li, X. Su, S. Zou, X. Wang, M. Shen, n-type silicon photocathodes with Al-doped rear p^+ emitter and Al_2O_3-coated front surface for efficient and stable H_2 production. *Applied Physical Letters* **2015**, *106 (21)*, 213901.

[86] W. Vijselaar, R. M. Tiggelaar, H. Gardeniers, J. Huskens, Efficient and stable silicon microwire photocathodes with a nickel silicide interlayer for operation in strongly alkaline solutions. *ACS Energy Letters* **2018**, *3 (5)*, 1086.

[87] R. Fan, C. Tang, Y. Xin, X. Su, X. Wang, M. Shen, Surface passivation and protection of Pt loaded multicrystalline pn^+ silicon photocathodes by atmospheric plasma oxidation for improved solar water splitting. *Applied Physical Letters* **2016**, *109 (23)*, 233901.

[88] C. U. Maier, M. Specht, G. Bilger, Hydrogen evolution on platinum-coated-silicon photocathodes. *International Journal of Hydrogen Energy* **1996**, *21 (10)*, 859.

[89] D. M. Andoshe, S. Choi, Y.-S. Shim, S. H. Lee, Y. Kim, C. W. Moon, D. H. Kim, S. Y. Lee, T. Kim, H. K. Park, M. G. Lee, J.-M. Jeon, K. T. Nam, M. Kim, J. K. Kim, J. Oh, H. W. Jang, A wafer-scale antireflective protection layer of

solution-processed TiO_2 nanorods for high performance silicon-based water splitting photocathodes. *Journal of Materials Chemistry A* **2016**, *4 (24)*, 9477.

[90] Z. Yin, R. Fan, G. Huang, M. Shen, 11.5% efficiency of TiO_2 protected and Pt catalyzed n^+np^+-Si photocathodes for photoelectrochemical water splitting: manipulating the Pt distribution and Pt/Si contact. *Chemical Communications (Camb.)* **2018**, *54 (5)*, 543.

[91] R. Fan, W. Dong, L. Fang, F. Zheng, M. Shen, More than 10% efficiency and one-week stability of Si photocathodes for water splitting by manipulating the loading of the Pt catalyst and TiO_2 protective layer. *Journal of Materials Chemistry A* **2017**, *5 (35)*, 18744.

[92] S. Vanka, E. Arca, S. Cheng, K. Sun, G. A. Botton, G. Teeter, Z. Mi, High efficiency Si photocathode protected by multifunctional GaN nanostructures, *Nano Letters* **2018**, *18 (10)*, 6530.

[93] H. Li, B. Liu, S. Feng, H. Li, T. Wang, J. Gong, Construction of uniform buried pn junctions on pyramid Si photocathodes using a facile and safe spin-on method for photoelectrochemical water splitting, *Journal of Materials Chemistry A* **2020**, *8*, 224.

[94] B. Seger, A. B. Laursen, P. C. Vesborg, T. Pedersen, O. Hansen, S. Dahl, I. Chorkendorff, Hydrogen production using a molybdenum sulfide catalyst on a titanium-protected n^+p-silicon photocathode. *Angewandte Chemie International Edition* **2012**, *51 (36)*, 9128.

[95] J. D. Benck, S. C. Lee, K. D. Fong, J. Kibsgaard, R. Sinclair, T. F. Jaramillo, Designing active and stable silicon photocathodes for solar hydrogen Production using molybdenum sulfide nanomaterials, *Advanced Energy Materials* **2014**, *4*, 1400739.

[96] Q. Ding, J. Zhai, M. Cabán-Acevedo, M. J. Shearer, L. Li, H. C. Chang, M. L. Tsai, D. Ma, X. Zhang, R. J. Hamers, J. H. He, S. Jin, Designing efficient solar-driven hydrogen evolution photocathodes using semitransparent MoQxCly (Q = S, Se) catalysts on Si micropyramids, *Advanced Materials* **2015**, *27 (41)*, 6511.

[97] M. Cabán-Acevedo, M. L. Stone, J. R. Schmidt, J. G. Thomas, Q. Ding, H. C. Chang, M. L. Tsai, J. H. He, S. Jin, Efficient hydrogen evolution catalysis using ternary pyrite-type cobalt phosphosulphide, *Nature Materials* **2015**, *14 (12)*, 1245.

[98] R. Fan, J. Mao, Z. Yin, J. Jie, W. Dong, L. Fang, F. Zheng, and M. Shen, Efficient

and stable silicon photocathodes coated with vertically standing nano-MoS_2 films for solar hydrogen production. *ACS Applied Materials & Interfaces* **2017**, *9 (7)*, 6123.

[99] M. R. Shaner, J. R. McKone, H. B. Gray, N. S. Lewis, Functional integration of Ni–Mo electrocatalysts with Si microwire array photocathodes to simultaneously achieve high fill factors and light-limited photocurrent densities for solar-driven hydrogen evolution. *Energy & Environmental Science* **2015**, *8 (10)*, 2977.

[100] H. Zhang, Q. Ding, D. He, H. Liu, W. Liu, Z. Li, B. Yang, X. Zhang, L. Lei, S. Jin, A p-Si/NiCoSe$_X$ core/shell nanopillar array photocathode for enhanced photoelectrochemical hydrogen production. *Energy & Environmental Science* **2016**, *9 (10)*, 3113.

[101] S. C. Warren, E. Thismen, Plasmonic solar water splitting. *Energy & Environmental Science* **2012**, *5*, 5133.

[102] T. Tatsuma, H. Nishi, T. Ishida, Plasmon-induced charge separation: chemistry and wide applications. *Chemical Sciecne* **2017**, *8*, 3325.

[103] S.-S. Yi, X.-B. Zhang, B.-R. Wulan, J.-M. Yan, Q. Jiang, Non-noble metals applied to solar water splitting. *Energy & Environmental Science* **2018**, *11*, 3128.

[104] S. Bai, J. Jiang, Q. Zhang, Y. Xiong, Steering charge kinetics in photocatalysis: intersection of materials syntheses, characterization techniques and theoretical simulations. *Chemical Society Reviews* **2015**, *44*, 2893.

[105] Z. Zhang, J. T. Yates Jr., Band bending in semiconductors: chemical and physical consequences at surfaces and interfaces. *Chemical Reviews* **2012**, *112*, 5520.

[106] C. Jia, X. Li, N. Xin, Y. Gong, J. Guan, L. Meng, S. Meng, X. Guo, Interface-engineered plasmonics in metal/semiconductor heterostructures. *Advanced Energy Materials* **2016**, *6*, 1600431.

[107] P. Zhang, T. Wang, J. Gong, Mechanistic understanding of the plasmonic enhancement for solar water splitting. *Advanced Materials* **2015**, *27*, 5328.

[108] Y.-C. Pu, G. Wang, K.-D. Chang, Y. Ling, Y.-K. Lin, B. C. Fitzmorris, C.-M. Liu, X. Lu, Y. Tong, J. Z. Zhang, Y.-J. Hsu, Y. Li, Au nanostructure-decorated TiO_2 nanowires exhibiting photoactivity across entire UV-visible region for photoelectrochemical water splitting. *Nano Letters* **2013**, *13*, 3817.

[109] M. K. Kumar, S. Krishnamoorthy, L. K. Tan, S. Y. Chiam, S. Tripathy, H. Gao, Field effects in plasmonic photocatalyst by precise SiO_2 thickness control using atomic layer deposition. *ACS Catalysis* **2011**, *1*, 300.

[110] A. P. Kulkarni, K. M. Noone, K. Munechika, S. R. Guyer, D. S. Ginger, Plasmon-enhanced charge carrier generation in organic photovoltaic films using silver nanoprisms. *Nano Letters* **2010**, *10*, 1501.

[111] T. Torimoto, H. Horibe, T. Kameyama, K.-I. Okazaki, S. Ikeda, M. Matsumura, A. Ishikawa, H. Ishihara, Plasmon-enhanced photocatalytic activity of cadmium sulfide nanoparticle immobilized on silica-coated gold particles. *the Journal of Physical Chemistry Letters* **2011**, *2*, 2057.

[112] T. K. Sau, A. L. Rogach, F. Jaeckel, T. A. Klar, J. Feldmann, Properties and applications of colloidal nonspherical noble metal nanoparticles. *Advanced Materials* **2010**, *22*, 1805.

[113] K. Oh, C. Meriadec, B. Lassalle-Kaiser, V. Dorcet, B. Fabre, S. Ababou-Girard, L. Joanny, F. Gouttefangeas, G. Loget, Elucidating the performance and unexpected stability of partially coated water-splitting silicon photoanodes. *Energy & Environmental Science* **2018**, *11*, 2590.

[114] K. Oh, L. Joanny, F. Gouttefangeas, B. Fabre, V. Dorcet, B. Lassalle-Kaiser, A. Vacher, C. Mériadec, S. Ababou-Girard, G. Loget, Black silicon photoanodes entirely prepared with abundant materials by low-cost wet methods. *ACS Applied Energy Materials* **2019**, *2*, 1006.

[115] C.-W. Tung, T.-R. Kuo, C.-S. Hsu, Y. Chuang, H.-C. Chen, C.-K. Chang, C.-Y. Chien, Y.-J. Lu, T.-S. Chan, J.-F. Lee, J.-Y. Li, H. M. Chen, Light-induced activation of adaptive junction for efficient solar-driven oxygen evolution: In situ unraveling the interfacial metal-silicon junction. *Advanced Energy Materials* **2019**, *9*, 1901308.

[116] J. C. Hill, A. T. Landers, J. A. Switzer, An electrodeposited inhomogeneous metal-insulator-semiconductor junction for efficient photoelectrochemical water oxidation, *Nature Materials* **2015**, *14*, 1150.

[117] Kiseok Oh, Vincent Dorcet, Bruno Fabre, Gabriel Loget, Dissociating water at n-Si photoanodes partially covered with Fe catalysts. *Advanced Energy Materials* **2020**, *10*, 1902963.

[118] J. Yang, D. Wang, H. Han, C. Li, Roles of cocatalysts in photocatalysis and photoelectrocatalysis. *Accounts of Chemical Research* **2013**, *46*, 1900.

[119] Timur Sh. Atabaev, Md Ashraf Hossain, Dongyun Lee, Hyung-Kook Kim, Yoon-Hwae Hwang, Pt-coated TiO_2 nanorods for photoelectrochemical water splitting applications. *Results in Physics* **2016**, *6*, 373.

[120] H. Chen, L. Shao, Q. Li and J. Wang, Gold nanorods and their plasmonic properties. *Chemical Society Reviews* **2013**, *42*, 2679.

[121] N. Tian, Z.-Y. Zhou, S.-G. Sun, Y. Ding, Z. L. Wang, Synthesis of tetrahexahedral platinum nanocrystals with high-index facets and high electro-oxidation activity. *Science* **2007**, *316*, 732.

[122] S. Chandra, R. K. Pandey, Semiconductor photoelectrochemical solar cells. *Physica Status Solidi A* **1982**, *72*, 415

[123] M. Chaplin, Water structure and science, **2008**. http://www1.lsbu.ac.uk/water/electrolysis.html

[124] P. Lianos, Review of recent trends in photoelectrocatalytic conversion of solar energy to electricity and hydrogen. *Applied Catalysis B: Environmental* **2017**, *210*, 235.

[125] H. M. Chen, C. K. Chen, R. S. Liu, L. Zhang, J. Zhang, D. P. Wilkinson, Nano-architecture and material designs for water splitting photoelectrodes. *Chemical Society Reviews* **2012**, *41*, 5654.

[126] C. Ding, X. Zhou, J. Shi, P. Yan, Z. Wang, G. Liu, C. Li, Abnormal effects of cations (Li^+, Na^+, and K^+) on photoelectrochemical and electrocatalytic water splitting. *The Journal of Physical Chemistry* B **2015**, *119*, 3560.

[127] C. Ding, J. Shi, Z. Wang, Can Li, Photoelectrocatalytic water splitting: significance of cocatalysts, electrolyte, and interfaces, *ACS Catalysis* **2017**, *7*, 675.

[128] M. Von Ardenne, Improvements in electron microscopes. GB 511204, convention date (Germany), **1937**.

[129] S. Chandrasekaran, N. Kaeffer, L. Cagnon, D. Aldakov, J. Fize, G. Nonglaton, F. Baleras, P. Mailley, V. Artero, A robust ALD-protected silicon-based hybrid photoelectrode for hydrogen evolution under aqueous conditions. *Chemical Science* **2019**, *10*, 4469.

[130] J. Goldstein, Scanning electron microscopy and X-ray microanalysis. **2003**, Springer. ISBN 978-0-306-47292-3.

[131] S. Pishgar, J. M. Strain, S. Gulati, G. Sumanasekera, G. Gupta, J. M. Spurgeon, Investigation of the photocorrosion of n-GaP photoanodes in acid with in situ UV-Vis spectroscopy. *Journal of Materials Chemistry A* **2019**, *7*, 25377.

[132] G. Zhang, H. Miao, Y. Wang, D. Zhang, J. Fan, T. Han, J. Mu, X. Hu, The fabrication and photoelectrocatalytic study of composite ZnSe/Au/TiO_2 nanotube

films. *Journal of Physics D: Applied Physics* **2017**, *50*, 185102.

[133] G. Binnig, Atomic force microscope and method for imaging surfaces with atomic resolution. U.S. Patent **1985**, US4724318.

[134] G. Binnig, C. F. Quate, C. Gerber, Atomic force microscope. *Physical Review Letters* **1986**, *56 (9)*, 930.

[135] B. Cappella, G. Dietler, Force-distance curves by atomic force microscopy. *Surface Science Reports* **1999**, *34 (1-3)*, 1.

[135] F. A. L. Laskowski, S. Z. Oener, M. R. Nellist, A. M. Gordon, D. C. Bain, J. L. Fehrs, S. W. Boettcher, Nanoscale semiconductor/catalyst interfaces in photoelectrochemistry. *Nature Materials* **2020**, *19*, 69.

[136] M. P. Murrell, M. E. Welland, S. J. O'Shea, T. M. H. Wong, J. R. Barnes, A. W. McKinnon, M. Heyns, S. Verhaverbeke, Spatially resolved electrical measurements of SiO_2 gate oxides using atomic force microscopy. *Applied Physics Letters* **1993**, *62 (7)*, 786.

[137] K. Tang, A. C. Meng, F. Hui, Y. Shi, T. Petach, C. Hitzman, A. L. Koh, D. Goldhaber-Gordon, M. Lanza, P. C. McIntyre, Distinguishing oxygen vacancy electromigration and conductive filament formation in TiO_2 resistance switching using liquid electrolyte contacts. *Nano Letters* **2017**, *17*, 4390.

[138] C. Pan, Y. Ji, N. Xiao, F. Hui, K. Tang, Y. Guo, X. Xie, F. M. Puglisi, L. Larcher, E. Miranda, L. Jiang, Y. Shi, I. Valov, P. C. McIntyre, R. Waser, M. Lanza, Coexistence of grain-boundaries-assisted Bbipolar and threshold resistive switching in multilayer hexagonal boron nitride. *Advanced Functional Materials* **2017**, 1604811.

[139] B. Scherrer, T. Li, A. Tsyganok, M. Döbeli, B. Gupta, K. D. Malviya, O. Kasian, N. Maman, B. Gault, D. A. Grave, A. Mehlman, I. Visoly-Fisher, D. Raabe, A. Rothschild, Defect segregation and its effect on the photoelectrochemical properties of Ti-doped hematite photoanodes for solar water splitting. *Chemistry of Materials* **2020**. https://dx.doi.org/10.1021/acs.chemmater.9b03704.

[140] R. Kant, C. Dwivedi, S. Pathak, V. Dutta, Fabrication of ZnO nanostructures using Al doped ZnO (AZO) templates for application in photoelectrochemical water splitting. *Applied Surface Science* **2018**, *447*, 200.

[141] E. Ruska, M. Knoll, Das Elektronenmikroskop. *Zeitschrift für Physik* **1932**, *78*, 318.

[142] N. F. Cheville, J. Stasko, Techniques in Electron Microscopy of Animal Tissue.

Veterinary Pathology **2014**, *51* (1), 28.

[143] R. Erni, M. D. Rossell, C. Kisielowski, U. Dahmen, Atomic-resolution imaging with a sub-50-pm electron probe. *Physical Review Letters* **2009**, *102* (9): 096101.

[144] M. Li, H. Liu, Y. Song, J. Gao, Design and constructing of mutually independent crystal facet exposed TiO_2 homojunction and improving synergistic effects for photoelectrochemical hydrogen generation and pollutant degradation. *International Journal of Energy Research* **2018**, *42*, 4625.

[145] J. J. Friel, C. E. Lyman, Tutorial review: X-ray mapping in electron-beam instruments. *Microscopy and Microanalysis* **2006**, *12* (1), 2.

[146] M. Alqahtani, S. Sathasivam, F. Cui, L. Sterier, X. Xia, C. Blackman, E. Kim, H. Shin, M. Benamara, Y. I. Mazur, G. J. Salamo, I. P. Parkin, H. Liu, J. Wu, Heteroepitaxy of GaP on silicon for efficient and cost-effective photoelectrochemical water splitting. *Journal of Materials Chemistry A* **2019**, *7*, 8550.

[147] R. F. Egerton, Electron energy loss spectroscopy in the electron microscope (2^{nd} ed.), **1996**. New York: Plenum. ISBN 978-0-306-45223-9.

[148] R. Fan, S. Cheng, G. Huang, Y. Wang, Y. Zhang, S. Vanka, G. A. Botton, Z. Mi, M. Shen, Unassisted solar water splitting with 9.8% efficiency and over 100 h stability based on Si solar cells and photoelectrodes catalyzed by bifunctional Ni–Mo/Ni. *Journal of Materials Chemistry A* **2019**, *7*, 2200.

[149] K. Siegbahn, K. Edvarson, β-ray spectroscopy in the precision range of 1:105. *Nuclear Physics* **1956**, *1* (3), 137.

[150] Y. Wang, Y. Zhou, M. Han, Y. Xi, H. You, X. Hao, Z. Li, J. Zhou, D. Song, D. Wang, F. Gao, Environmentally-friendly exfoliate and active site self-assembly: thin 2D/2D heterostructure amorphous Nickel–Iron alloy on 2D materials for efficient oxygen evolution reaction. *Small* **2019**, *15*, 1805435.

[151] L. Li, L. Duan, Y. Xu, M. Gorlov, A. Hagfeldt, L. Sun, A photoelectrochemical device for visible light driven water splitting by a molecular ruthenium catalyst assembled on dye-sensitized nanostructured TiO_2. *Chemical Communications* **2010**, *46*, 7307.

[152] K. Sun, F. H. Saadi, M. F. Lichterman, W. G. Hale, H. Wang, X. Zhou, N. T. Plymale, S. T. Omelchenko, J.-H. He, K. M. Papadantonakis, B. S. Brunschwig, N. S. Lewis, Stable solar-driven oxidation of water by semiconducting photoanodes

protected by transparent catalytic nickel oxide films. *Proceedings of the National Academy of Sciences of the United States of America* **2015**, *112*, 3612.

[153] J. Du, Z. Chen, S. Ye, B. J. Wiley, T. J. Meyer, Copper as a robust and transparent electrocatalyst for water oxidation. *Angewandte Chemie International Edition* **2015**, *54*, 2073.

[154] F. Yu, F. Li, B. Zhang, H. Li, L. Sun, Efficient electrocatalytic water oxidation by a copper oxide thin film in borate buffer. *ACS Cataysis* **2015**, *5*, 627.

[155] V. Artero, M. Chavarot-Kerlidou, M. Fontecave, Splitting water with cobalt. *Angewandte Chemie International Edition* **2011**, *50*, 7238.

[156]K. Sun, S. Shen, J. S. Cheung, X. Pang, N. Park, J. Zhou, Y. Hu, Z. Sun, S. Y. Noh, C. T. Riley, P. K. L. Yu, S. Jin, D. Wang, Si photoanode protected by a metal modified ITO layer with ultrathin NiO_X for solar water oxidation. *Physical Chemistry Chemical Physics* **2014**, *16*, 4612.

[157] B. Mei, A. A. Permyakova, R. Frydendal, D. Bae, T. Pedersen, P. Malacrida, O. Hansen, I. E. L. Stephens, P. C. K. Vesborg, B. Seger, I. Chorkendorff, Iron-treated NiO as a highly transparent p-type protection layer for efficient Si-based photoanodes. *The Journal of Physical Chemistry Letters* **2014**, *5*, 3456.

[158] C. Gui, M. Elwenspoek, N. Tas, J. G. E. Gardeniers, The effect of surface roughness on direct wafer bonding. *Journal of Applied Physics* **1999**, *85*, 7448.

[159] B. E. Conway, T. Liu, Experimental evaluation of adsorption behaviour of intermediates in anodic oxygen evolution at oxidized nickel surfaces. *Journal of the Chemical Society, Faraday Transactions 1* **1987**, *83*, 1063.

[160] M. Miyazaki, H. Hirayama, Thickness- and deposition temperature-dependent morphological change in electronic growth of ultra-thin Ag films on Si (111) substrates. *Surface Science* **2008**, *602*, 276.

[161] T. R. Cook, D. K. Dogutan, S. Y. Reece, Y. Surendranath, T. S. Teets, D. G. Nocera, Solar energy supply and storage for the legacy and nonlegacy worlds. *Chemical Reviews* **2010**, *110*, 6474.

[162] K. Leng, W. Mai, X. Zhang, R. Liu, X. Lin, J. Huang, H. Lou, Y. Xie, R. Fu, D. Wu, Construction of functional nanonetworkstructured carbon nitride with Au nanoparticle yolks for highly efficient photocatalytic applications. *Chemical Communications* **2018**, *54*, 7159

[163] Y. Hou, B. L. Abrams, P. C. K. Vesborg, M. E. Bjorketun, K. Herbst, L. Bech, A. M. Setti, C. D. Damsgaard, T. Pedersen, O. Hansen, J. Rossmeisl, S. Dahl, J. K.

Norskov, I. Chorkendorff, Bioinspired molecular co-catalysts bonded to a silicon photocathode for solar hydrogen evolution. *Nature Materials* **2011**, *10*, 434.

[164] R. N. Dominey, N. S. Lewis, J. A. Bruce, D. C. Bookbinder, M. S. Wrighton, Improvement of photoelectrochemical hydrogen generation by surface modification of p-type silicon semiconductor photocathodes. *Journal of the American Chemical Society* **1982**, *104*, 467.

[165] T. Han, S. Privitera, R. G. Milazzo, C. Bongiorno, S. Di Franco, F. La Via, X. Song, Y. Shi, M. Lanza, S. Lombardo, Photo-electrochemical water splitting in silicon based photocathodes enhanced by plasmonic/catalytic nanostructures. *Materials Science & Engineering B* **2017**, *225*, 128.

[166] G. Hodes, L. Thompson, J. DuBow, K. Rajeshwar, Heterojunction silicon/indium tin oxide photoelectrodes: development of stable systems in aqueous electrolytes and their applicability to solar energy conversion and storage. *Journal of the American Chemical Society* **1983**, *105*, 324.

[167] A. G. Scheuermann, J. P. Lawrence, K.W. Kemp, T. Ito, A. Walsh, C. E. D. Chidsey, P. K. Hurley, P. C. McIntyre, Design principles for maximizing photovoltage in metal-oxide-protected water-splitting photoanodes. *Nature Materials* **2016**, *15*, 99.

[168] R. Tang, S. Zhou, Z. Yuan, L. Yin, Metal–organic framework derived $Co_3O_4/TiO_2/Si$ heterostructured nanorod array photoanodes for efficient photoelectrochemical water oxidation. *Advanced Functional Materials* **2017**, 1701102.

[170] T. Han, Y. Shi, X. Song, A. Mio, L. Valenti, F. Hui, S. Privitera, S. Lombardo, M. Lanza, Ageing mechanisms of highly active and stable nickel-coated silicon photoanodes for water splitting. *Journal of Materials Chemistry A* **2016**, *4*, 8053.

[171] Y. Shi, C. Gimbert-Suriñach, T. Han, S. Berardi, M. Lanza, A. Llobet, CuO-functionalized silicon photoanodes for photoelectrochemical water splitting devices. *ACS Applied Materials & Interfaces* **2016**, *8*, 696.

[172] T. Yao, X. An, H. Han, J. Q. Chen, C. Li, Photoelectrocatalytic materials for solar water splitting. *Advanced Energy Materials* **2018**, 1800210.

[173] K. Wu, W. Quan, H. Yu, H. Zhao, S. Chen, Graphene/silicon photoelectrode with high and stable photoelectrochemical response in aqueous solution. *Applied Surface Science* **2011**, *257*, 7714.

[174] C. Tan, X. Cao, X.-J. Wu, Q. He, J. Yang, X. Zhang, J. Chen, W. Zhao, S. Han,

G.-H. Nam, M. Sindoro, H. Zhang, Recent advances in ultrathin two-dimensional nanomaterials. *Chemical Reviews* **2017**, *117*, 6225.

[175] K. C. Kwon, S. Choi, J. Lee, K. Hong, W. Sohn, D. M. Andoshe, K. S. Choi, Y. Kim, S. Han, S. Y. Kim, H. W. Jang, Drastically enhanced hydrogen evolution activity by 2D to 3D structural transition in anion-engineered molybdenum disulfide thin films for efficient Si-based water splitting photocathode. *Journal of Materials Chemistry A* **2017**, *5*, 15534.

[176] M. Gong, D.-Y. Wang, C.-C. Chen, B.-J. Hwang, H. Dai, A mini review on nickel-based electrocatalysts for alkaline hydrogen evolution reaction. *Nano Research* 2016, *9*, 28.

[177] R. Subbaraman, D. Tripkovic, D. Strcnik, K.-C. Chang, M. Uchimucra, A. P. Paulikas, V. Stamenkovic, N. M. Markovic, Enhancing hydrogen evolution activity in water splitting by tailoring Li^+-$Ni(OH)_2$-Pt interfaces. *Science* **2011**, *334*, 1256.

[178] Y. Du, S. Khan, X. Zhang, G. Yu, R. Liu, B. Zheng, R. Nadimicherla, D. Wu, R. Fu, In-situ preparation of porous carbon nanosheets loaded with metal chalcogenides for a superior oxygen evolution reaction. *Carbon* **2019**, *149*, 144.

[179] J. G. Mavroides, J. A. Kafalas, D. F. Kolesar, Photoelectrolysis of water in cells with $SrTiO_3$ anodes. *Applied Physics Letters* **1976**, *28*, 241.

[180] A. B. Ellis, S. W. Kaiser and M. S. Wrighton, SemiconductingPotassium Tantalate Electrodes. Photoassistance Agents for the Efficient Electrolysis of Water. *The Journal of Physical Chemistry* **1976**, *80*, 1325.

[181] E. Borgarello, J. Kiwi, E. Pelizzetti, M. Visca and M. Gratzel, Photochemical cleavage of water by photocatalysis. *Nature* **1981**, *289*, 158.

[182] T. Yasuda, M. Kato, M. Ichimura and T. Hatayama, SiC photoelectrodes for a self-driven water-splitting cell. *Applied Physics Letters* **2012**, *101*, 053902.

[183] A. Kudo, Y. Miseki, Heterogeneous photocatalyst materials for water splitting. *Chemical Society Review* **2009**, *38*, 253.

[184] J. Li, S. Meng, T. Wang, Q. Xu, L. Shao, D. Jiang, M. Chen, Novel Au/$CaIn_2S_4$ nanocomposites with plasmon-enhanced photocatalytic performance under visible light irradiation. *Applied Surface Science* **2017**, *396*, 430.

[185] P. Kuang, L. Zhang, B. Cheng, J. Yu, Enhanced charge transfer kinetics of Fe_2O_3/CdS composite nanorod arrays using cobalt-phosphate as cocatalyst. *Applied Catalysis B: Environmental* **2017**, *218*, 570.

[186] Y. Chen, L. Wang, W. Wang, M. Cao, Enhanced photoelectrochemical properties of ZnO/ZnSe/CdSe/$Cu_{2-X}Se$ core–shell nanowire arrays fabricated by ion-replacement method. *Applied Catalysis B: Environmental* **2017**, *209*, 110.

[187] Y. Chen, L. Wang, W. Wang, M. Cao, Synthesis of Se-doped ZnO nanoplates with enhanced photoelectrochemical and photocatalytic properties. *Materials Chemistry and Physics* **2017**, *199*, 416.

[188] M. A. Green, K. Emery, Y. Hishikawa, W. Warta, E. D. Dunlop, Solar cell efficiency tables (version 48). *Progress in Photovoltaics: Research and Applications* 2016, *24*, 905.

[189] X. G. Zhang, Electrochemistry of silicon and its Oxide, Kluwer Academic, New York, **2001**.

[190] O. Khaselev, A. Bansal, J. A. Turner, High-efficiency integrated multijunction photovoltaic/electrolysis systems for hydrogen production. *International Journal of Hydrogen Energy* **2001**, *26*, 127.

[191] T. L. Gibson, N. A. Kelly, Photoelectrochemical device and electrode. U.S. Patent **2006**, US7052587 B2.

[192] N. A. Kelly, Thomas L. Gibson, Design and characterization of a robust photoelectrochemical device to generate hydrogen using solar water splitting. *International Journal of Hydrogen Energy* **2006**, *31*, 1658.

[193]S. Y. Reece, J. A. Hamel, K. Sung, T. D. Jarvi, A. J. Esswein, J. J. H. Pijpers, D. G. Nocera, Wireless solar water splitting using silicon-based semiconductors and earth-abundant catalysts. *Science* **2011**, *334*, 645.

[194] D. V. Esposito, I. Levin, T. P. Moffat, A. Alec, Talin, H_2 evolution at Si-based metal–insulator–semiconductor photoelectrodes enhanced by inversion channel charge collection and H spillover. *Nature Materials* **2013**, *12*, 562.

[195] C. Ros, T. Andreu, M. D. Hernandez-Alonso, G. Penelas-Perez, J. Arbiol, J. R. Morante, Charge transfer characterization of ALD-Grown TiO_2 protective layers in silicon photocathodes. *ACS Applied Materials & Interfaces* **2017**, *9*, 17932.

[196] D. Bae, T. Pedersen, B. Seger, B. Iandolo, O. Hansen, P. C. K. Vesborg, I. Chorkendorff, Carrier-selective p- and n-contacts for efficient and stable photocatalytic water reduction. *Catalysis Today* **2017**, *290*, 59.

[197] M.-J. Park, J.-Y. Jung, Y.-H. Nam, J.-W. Song, C. Jeong, J.-H. Lee, Improved photoelectrochemical hydrogen evolution using a defect-passivated Al_2O_3 thin film on p-Si. *Thin Solid Film* **2016**, *616*, 550.

[198] D. W. Redman, H. J. Kim, K. J. Stevenson, M. J. Rose, Photo-assisted electrodeposition of MoS_X from ionic liquids on organic-functionalized silicon photoelectrodes for H_2 generation. *Journal of Materials Chemistry A* **2016**, *4*, 7027.

[199] M. J. Bazack, Surface studies on SiC as related to contacts. *Physica Status Solidi B* **1997**, *202*, 549.

[200] P. A. Basore, Numerical modeling of textured silicon solar cells using PC-1D. *IEEE Transactions on Electron Devices* **1990**, *37*, 337.

[201] S. Privitera, V. Brancato, D. Spadaro, R. Anzalone, A Alberti, F. La Via, 3C-SiC polycrystalline films on Si for photovoltaic applications. *Materials Science Forum,* **2015***, 821-823,* 189.

[202] G. Zhang, H. Miao, X. Hu, J. Mu, X. Liu, T. Han, J. Fan, E. Liu, Y. Yin, J. Wan, A facile strategy to fabricate Au/TiO_2 nanotubes photoelectrode with excellent photoelectrocatalytic properties. *Applied Surface Science* **2017**, *391*, 345.

[203] Y. Wang, J. Yu, W. Xiao, Q. Li, Microwave-assisted hydrothermal synthesis of graphene based Au-TiO_2 photocatalysts for efficient visible-light hydrogen production. *Journal of Materials Chemistry A* **2014**, *2*, 3847.

[204] J. E. Lee, S. Bera, Y. S. Choi, W. I. Lee, Size-dependent plasmonic effects of M and M@SiO_2 (M = Au or Ag) deposited on TiO_2 in photocatalytic oxidation reactions. *Applied Catalysis B: Environmental* **2017**, *214*, 15.

[205] S. Kamimura, S. Yamashita, S. Abe, T. Tsubota, T. Ohno, Effect of core@shell (Au@Ag) nanostructure on surface plasmon-induced photocatalytic activity under visible light irradiation. *Applied Catalysis B: Environmental* **2017**, *211*, 11.

[206]C. W. Moon, S. Y. Lee, W. Sohn, D. M. Andoshe, D. H. Kim, K. Hong, H. W. Jang, Plasmonic octahedral gold nanoparticles of maximized near electromagnetic fields for enhancing catalytic hole transfer in solar water splitting. *Particle & Particle Systems Characterization* **2017**, *34*, 1600340.

[207] R. Anzalone, A. Severino, G. D'Arrigo, C. Bongiorno, G. Abbondanza, G. Foti, S. Saddow, F. La Via, Heteroepitaxy of 3C-SiC on different on-axis oriented silicon substrates. *Journal of Applied Physics* **2009**, *105 (8)*, 084910.

[208] R. G. Milazzo, S. Privitera, G. Litrico, S. Scalese, S. Mirabella, F. La Via, S. Lombardo, E. Rimini, Formation, morphology, and optical properties of electroless deposited gold nanoparticles on 3C-SiC. *The Journal of Physical Chemistry C* **2017**, *121*, 4304.

[209] H.-H. Liu, Y. Liang, H.-J. Liu, Regular microarray of Au flower-like structure formed by template-assisted electrodeposition: Influence factors and their electrochemical behavior. *Electrochimica Acta* **2009**, *54*, 7514.

[210] G. Mie, Beiträge zur Optik trüber Medien, speziell kolloidaler Metallösungen. *Annalen Der Physik* **1908**, *330 (3)*, 377.

[211] K. Kolwas, A. Derkachova, Plasmonic abilities of gold and silver spherical nanoantennas in terms of size dependent multipolar resonance frequencies and plasmon damping rates. *Opto-Electronics Review* **2010**, *18*, 429.

[212] C. Sönnichsen, T. Franzl, T. Wilk, G. von Plessen, J. Feldmann, Plasmon resonances in large noble-metal clusters. *New Journal of Physics* **2002**, *4*, 93.1.

[213] X. Huang, M. A. El-Sayed, Gold nanoparticles: Optical properties and implementations in cancer diagnosis and photothermal therapy. *Journal of Advanced Research* **2010**, *1*, 13.

[214] C. Langhammer, Z. Yuan, I. Zoric, B. Kasemo, Plasmonic properties of supported Pt and Pd nanostructures. *Nano Letters* **2006**, *6 (4)*, 833.

[215] J. A. Creighton, D. G. Eadon, Ultraviolet-visible absorption spectra of the colloidal metallic elements. *Journal of the Chemical Society, Faraday Transactions* **1991**, *87 (24)*, 3881.

Appendix A: Scientific curriculum vitae

PERSONAL INFORMATION

Name: Tingting Han
Gender: Female
Date of birth: December 1st, 1990
Nationality: China
Languages: Chinese (native), English
Phone/Email: +34 604199239 / hantingting15@126.com
Google Scholar: https://scholar.google.com/citations?user=ac5f6b8AAAAJ&hl=zh-CN

EDUCATION BACKGROUND

Jun. 2020	PhD in Nanoscience (nanostructured materials) Electronic Engineering Department, University of Barcelona
	Dec. 2018 - May 2020 Visiting PhD student Professor Antoni Llobet's research group Institute of Chemical Research of Catalonia
Sep. 2014 - Jun. 2017	Master in Materials Science & Engineering Professor Mario Lanza's research group Institute of Functional Nano & Soft Materials Soochow University
	Feb. 2016 - Feb. 2017 Visiting PhD Student Professor Salvatore Lombardo's research group Institute for Microelectronics and Microsystems National Research Council of Italy
Sep. 2010 - Jun. 2014	Bachelor in Materials Chemistry Professor Hui Xu's research group, Ludong University

RESEARCH EXPERIENCE

- Topic 1 (Since September 2014): Water splitting solar cells:

1. Fabrication of nickel and titanium based metal-insulator-semiconductor photoanodes using electron beam evaporator and reactive sputtering.
2. Fabrication of noble metal nanoparticles covered silicon on silicon carbide photocathodes using magnetron sputtering and chemical deposition.

3. Fabrication of molecular based photoanodes by doctor blade method.
4. Characterization of electrochemical properties of the photoelectrodes using a Newport lamp and the electrochemical workstation.
5. Characterization of the morphology and topography of the samples with SEM, AFM and TEM, studying their chemical composition with XPS and EDX, and their electrical property with probe station and PVE300 Bentham System combined with a 450 W Xenon lamp and 300 mm focal length monochromator.
6. Water oxidation characterization by Generator-Collector measurement

❖ Topic 2 (Since November 2017): Ionic liquids for the study of resistive switching devices

1. Fabricate the devices with small circular windows using electron beam evaporator, photolithography, atomic layer deposition and magnetron sputtering.
2. Analyze the conductivity of some devices using a probe station by dropping ionic liquid on the window area before and after applying bias using Conductive AFM.
3. Evaporate silver nanoparticles on dielectric insulator to improve the electrical performance.
4. Characterization of the dielectric insulator with SEM, AFM and TEM.

❖ Topic 3 (Sept. 2011 to March 2014): Synthesis and characterization of silver nanoparticles:

1. Prepare the extracts and synthesize silver nanoparticles.
2. Characterization of the nanoparticles with Ultraviolet-Visible Spectroscopy.
3. Trainings in nanofabrication and nanocharacterization tools: Atomic Force Microscope, Electron-Beam Evaporation, Magnetron Sputtering, Scanning Electron Microscope, Energy Dispersive X-ray Analysis, X-ray Photoelectron Spectroscopy, Ultraviolet-Visible Spectroscopy, Fluorescence Spectrophotometer.

❖ Software:

1. Familiar with the software of Origin, NanoScope Analysis to process the data.
2. Familiar with Power Point presentations and Excel data processing.
3. Familiar with the software of layout for designing the electrode masks.

JOURNAL PAPERS

❖ **Tingting Han**, Yuanyuan Shi, Xiaoxue Song, Antonio Mio, Luca Valenti, Fei Hui, Stefania Privitera, Salvatore Lombardo, Mario Lanza*. Ageing mechanisms of

highly active and stable nickel-coated silicon photoanodes for water splitting. ***Journal of Materials Chemistry A***. 2016, 4 (21): 8053-8060. Selected as back cover article.

- **Tingting Han**, Stefania Privitera*, Gabriela Milazzo, Corrado Bongiorno, Salvatore Di Franco, Francesco La Via, Xiaoxue Song, Yuanyuan Shi, Mario Lanza, Savatore Lombardo. Photo-electrochemical water splitting in silicon based photocathodes enhanced by plasmonic/catalytic nanostructures. ***Materials Science and Engineering: B***. 2017, 225: 128-133.

- **Tingting Han**, Yuanyuan Shi*, Zhouchangwan Yu, Byungha Shin, and Mario Lanza*. Potassium hydroxide mixed with lithium hydroxide: an advanced electrolyte for oxygen evolution reaction. ***Solar RRL.*** 2019, 1900195.

- Yuanyuan Shi, **Tingting Han**, Carolina Gimbert-Suriñach, Xiaoxue Song, Mario Lanza*, Antoni Llobet*. Substitution of native silicon oxide by titanium in Ni-coated silicon photoanodes for water splitting solar cells. ***Journal of Materials Chemistry A***. 2016, 5 (5): 1996-2003.

- Yuanyuan Shi, Carolina Gimbert-Suriñach, **Tingting Han**, Serena Berardi, Mario Lanza*, Antoni Llobet*. CuO-Functionalized Silicon Photoanodes for Photoelectrochemical Water Splitting Devices. ***ACS Applied Materials & Interfaces***. 2015, 8 (1): 696-702.

- Yanfeng Ji, Fei Hui, Yuanyuan Shi, **Tingting Han**, Xiaoxue Song, Chengbin Pan, Mario Lanza*. Fabrication of a fast-response and user-friendly environmental chamber for atomic force microscopes. ***Review of Scientific Instruments***. 2015, 86 (10), 106105.

- Mario Lanza*, H.-S. Philip Wong, Eric Pop, Daniele Ielmini, Dimitri Strukov, Brian C. Regan, Luca Larcher, Marco A. Villena, J. Joshua Yang, Ludovic Goux, Attilio Belmonte, Yuchao Yang, Francesco M. Puglisi, Jinfeng Kang, Blanka Magyari-Köpe, Eilam Yalon, Anthony Kenyon, Mark Buckwell, Adnan Mehonic, Alexander Shluger, Haitong Li, Tuo-Hung Hou, Boris Hudec, Deji Akinwande, Ruijing Ge, Stefano Ambrogio, Juan B. Roldan, Enrique Miranda, Jordi Suñe, Kin Leong Pey, Xing Wu, Nagarajan Raghavan, Ernest Wu, Wei D. Lu, Gabriele Navarro, Weidong Zhang, Huaqiang Wu, Runwei Li, Alexander Holleitner, Ursula Wurstbauer, Max C. Lemme, Ming Liu, Shibing Long, Qi Liu, Hangbing Lv, Andrea Padovani, Paolo Pavan, Ilia Valov, Xu Jing, **Tingting Han**, Kaichen Zhu, Shaochuan Chen, Fei Hui, and Yuanyuan Shi. Recommended methods to study resistive switching devices. ***Advanced Electronic Materials***. 2018, 1800143.

- Shaochuan Chen, Seyedreza Noori, Marco Villena, Yuanyuan Shi, **Tingting Han**, Ying Zuo, Mariapia Pedeferri, Dmitri Strukov, Mario Lanza*, Maria Vittoria Diamanti. Memristive electronic synapses made by anodic oxidation. ***Chemistry of Materials***. 2019. ***DOI: 10.1021/acs.chemmater.9b02245***.

- Tao Wang, Yuanyuan Shi, Francesco Puglisi, Shaochuan Chen, Kaichen Zhu, Ying Zuo, Xuehua Li, Xu Jing, **Tingting Han**, Biyu Guo, Kristýna Bukvišová, Lukáš Kachtík, Miroslav Kolíbal, Chao Wen, Mario Lanza*. Electroforming in metal-oxide memristive synapses, ***ACS Applied Materials and Interfaces,*** 2020. ***https://doi.org/10.1021/acsami.9b19362***.

- Biyu Guo, Ying Zuo, Yuanyuan Shi, **Tingting Han**, Mario Lanza*. Transmission electron microscopy based quality analysis of commercially available graphene oxide quantum dots, ***Crystal Research and Technology*** 2020, ***Accepted***.

- Hui Xu, Lei Wang*, Hongyan Su, Liang Gu, **Tingting Han**, Fanbin Meng, Chongchong Liu. Making good use of food wastes: green synthesis of highly stabilized silver nanoparticles from grape seed extract and their antimicrobial activity. ***Food Biophysics***. 2015, 10 (1): 12-18.

- Lei Wang, Hui Xu*, Liang Gu, **Tingting Han**, Shuai Wang, Fanbin Meng. Bioinspired synthesis, characterization and antibacterial activity of plant-mediated silver nanoparticles using purple sweet potato (Ipomoea batatas L.) root extract. ***Materials Technology: Advanced Performance Materials***. 2016, 31 (8): 437-442.

CONFERENCE PAPERS

- Mario Lanza*, Kechao Tang, Kechao Tang, Fei Hui, Yuanyuan Shi, **Tingting Han**, Trevor Petach,Charles Hitzman, Ai Leen Koh, David Goldhaber-Gordon, Paul C. McIntyre. Using Liquid Electrolytes in Dielectric Reliability Studies, 2018 IEEE International Symposium on the Physical and Failure Analysis of Integrated Circuits (IPFA), Singapore, 2018, pp. 1-6. DOI: 10.1109/IPFA.2018.8452552.

CONFERENCE

- Yuanyuan Shi, **Tingting Han**, Xiaoxue Song, Antonio Mio, Luca Valenti, Stefania Privitera, Salvatore Lombardo, Mario Lanza, Metal-oxide-semiconductor (MOS) photoanodes for photoeletrochemical water splitting devices, International Conference on Materials for Energy Applications, January 3rd - 6th 2017, City University of Hong Kong, Hong Kong.

- **Tingting Han**, Yuanyuan Shi, Xiaoxue Song, Antonio Mio, Luca Valenti, Fei Hui,

Stefania Privitera, Salvatore Lombardo, Mario Lanza, Ageing mechanisms of nickel based n-type silicon photoanodes for photoelectrochemical water splitting, the 1st Italian National Conference on Materials Science and Technology, December 12th - 16th 2016, Catania, Italy.

- Yuanyuan Shi, **Tingting Han**, Xiaoxue Song, Mario Lanza, Reliability and ageing mechanisms of ultrathin nickel coated silicon photoanodes for water splitting, The 8th International Conference On Technological Advances Of Thin Films and Surface Coatings, July 12th - 15th 2016, Singapore.

- Yuanyuan Shi, **Tingting Han**, Xiaoxue Song, Antonio Mio, Luca Valenti, Stefania Privitera, Salvatore Lombardo, Mario Lanza, Metal-oxide-semiconductor (MOS) photoanodes for photoeletrochemical water splitting devices, 19th Workshop on Dielectrics in Microelectronics, June 27th - 30th 2016, Catania, Italy.

- ChinaRRAM 2017, June 12th – 13th 2017, Soochow University, Suzhou, China.

INTERNSHIP

- 2011-09 - 2014-06 Internship in Professor Hui Xu's laboratory

1. Help the professor do the experiments about biological chemistry.
2. Help the graduates do plan and redact their thesis.
3. I also study about the development of the experiments and configuration of equipment.

AWARDS AND REVIEWER

- Reviewer of Scientific Reports (Since December 2018): Review 1 paper
- Postgraduate International Exchange Scholarship of Soochow University in 2016
- Fellowship of the ICTP programme for Trainning and Research in Italian Laborotaries
- Outstanding students first-class scholarship of Ludong University for twice
- Learning model of Ludong University
- Outstanding Youth League of Ludong University
- Outstanding graduation thesis for Bachelor
- Outstanding graduates of Ludong University

Appendix B: Summary in official language

Durante esta tesis doctoral, he aprendido a crecer películas delgadas de metal y/o óxido metálico de alta calidad a través de métodos físicos de deposición de vapor, incluyendo pulverización catódica, evaporación de haz electrónico, evaporación térmica y deposición por capas atómicas, así como la deposición electroquímica utilizando un potenciostato. En mi investigación, el análisis fotoelectroquímico es uno de los métodos de caracterización más importantes. Aprendí a construir / ensamblar varios dispositivos de división de agua impulsados por energía solar, y realicé multiples análisis para comprender mejor los óxidos metálicos / metálicos de los fotoelectrodos. Además, también aprendí a analizar las muestras mediante una serie de caracterizaciones morfológicas, topográficas, eléctricas, mecánicas y químicas a escala nano- y micro-métricas, a través de AFM, SEM, EDX, TEM y XPS, e incluso analicé las propiedades eléctricas a nivel de dispositivo mediante una taba de puntas y un sistema Bentham PVE300.

En la primera parte de mi tesis, he investigado (a escala sub-nanométrica) los mecanismos de envejecimiento de los fotoanodos de n-Si varnizados con Ni, sumergidos en electrolitos de KOH 1.0 M (pH 14) para la reacción de evolución de oxígeno conducida por la luz. Mis resultados obtenidos indican que:

- Los mecanismos de envejecimiento de los fotoanodos Ni/SiO_X/n-Si/Ti dependen del grosor de las capas de Ni. Los fotoanodos con un recubrimiento de Ni más delgado dieron como resultado una mayor actividad de la célula solar, pero una estabilidad corta.
- La falla de las muestras recubiertas con una capa de níquel de 2 nm de espesor dentro de las 18 horas se debió a la formación de una película de SiO_X interfacial gruesa, que bloquea la transferencia de agujeros / electrones al electrolito / sustrato, y también a la penetración extensa de impurezas de potasio en la capa de NiO_X.
- Los fotoanodos con capas de níquel de 5 nm y 10 nm de espesor mostraron corrientes estables bajo un potencial constante durante más de 150 y 260 horas, respectivamente. La degradación de estas muestras se debió a la formación de

muchos agujeros en la capa activa de NiO_X, y el tamaño / densidad de los agujeros dependía del grosor de la capa de NiO_X.

- Al combinar las técnicas TEM y EELS, se pudo detectar la contaminación de potasio en la película NiO_X, que estaba enmascarada en los perfiles XPS, lo que indica que los informes anteriores observados por las herramientas de caracterización tradicionales (con baja resolución especial) en el campo de la división del agua pueden ignorar lo fenómenos de degradación esenciales. Estos hallazgos, que revelan información esencial, pueden ser de gran interés para los investigadores para estudiar la mejora la vida útil de las células solares que dividen el agua.

Después de comprender el proceso de degradación de los fotoanodos de n-Si basados en Ni para la división del agua fotoelectroquímica, decidí estudiar el efecto de los electrolitos para mejorar el rendimiento de los fotoanodos. Los fotoanodos de n-Si varnizados con 5 nm de Ni para la división fotoelectronquímica de agua se han analizado en cuatro electrolitos alcalinos diferentes. Mis principales logros son:

- En cuanto a la prueba de actividad, el potencial de inicio de los fotoanodes para la oxidación del agua muestra la tendencia de $V_{ON,\ pH\ 14} < V_{ON,\ pH\ 12.5} < V_{ON,\ pH\ 9.5}$. Los photoanodes a pH 9.5 con iones de Li y pH 12.5 necesitan un sobrepotencial de 0.243 V y 0.024 V para la división del agua, respectivamente. Sin embargo, el potencial de inicio del fotoanodo a pH 14 muestra ser 0.039 V más catódico que el potencial dinámico térmico para la oxidación del agua.
- En cuanto a la prueba de estabilidad, los fotoanodos se mostraron mucho más estables a pH 9.5 y 12.5 (ambos con iones de Li) que a pH 14, principalmente gracias a la presencia de iones de Li en los electrolitos, y aún se mantuvieron en un potencial estable después de 264 horas (en curvas P–t bajo una densidad de corriente constante de 10 mA/cm^2.
- Teniendo en cuenta tanto la actividad como la estabilidad, los fotoanodos de n-Si varnizados con 5 nm de Ni de muestran el mejor rendimiento de OER al usar un electrolito de pH 12.5. En general, el ajuste de la composición química del electrolito es un método económico y efectivo para mejorar el rendimiento de los fotoanodos de n-Si recubiertos de Ni para la división de agua fotoelectroquímica. Los trabajos futuros deberían explorar si este enfoque también puede ser útil para

mejorar el rendimiento de otros fotoelectrodos recubiertos de metal para la división del agua, no solo para OER sino también para HER.

Finalmente, también estudiamos fotocátodos basados en n-3C-SiC/p-Si decorados con nanopartículas de metales nobles (por ejemplo, Au, Pt) para HER en electrolito KOH 1.0 M (pH 14). Las principales conclusiones de este trabajo son:

- La capa 3C-SiC tipo *n* se utilizó como emisor y capa de silicio se usó como protectora. El fotocátodo 3C-SiC/Si mostró una fotocorriente altamente saturada de aproximadamente 30 mA/cm^2, y en 7,5 horas el fotocátodo reveló la buena estabilidad para HER.
- Las nanopartículas de metales nobles depositadas en la superficie de 3C-SiC son efectivas para reducir el potencial de inicio. Al ajustar adecuadamente el tamaño, la forma y la densidad de las nanopartículas de Au o Pt, las propiedades plasmónicas también se pueden mejorar, obteniendo una alta corriente saturada de aproximadamente 38 mA/cm^{-2}, muy cerca del límite físico para el silicio a AM 1.5G (1sun). Y el fotocatodo Pt NPs/n-3C-SiC/p-Si mostró una estabilidad fotoelectroquímica larga sin ninguna disminución apreciable durante 9 horas en electrolito KOH.

Al hacer uso de suficiente luz solar, las células solares de división de agua PEC han proporcionado una forma prometedora de producir energía de hidrógeno sostenible sin contaminación bajo combustión. Una gran cantidad de materiales nanoestructurados avanzados han sido explotados como catalizadores para fotoanodos o photocatodos. Sin embargo, para llevar a cabo OER o HER, aparte de la luz solar, generalmente se debe aplicar un potencial adicional para superar el potencial excesivo de los electrodos. Nuestro objetivo es ensamblar células en tándem con división de agua, que podrían producir H_2 y O_2 solo bajo la iluminación del sol. En este caso, es esencial considerar la absorción de luz y la coincidencia de la banda de energía de diferentes fotoelectrodos para mejorar la eficiencia de conversión. Los trabajos futuros deberían promover el rendimiento de los materiales semiconductores, encontrar nuevos materiales, desarrollar electrolitos avanzados y optimizar la configuración, entre otros. Además, la combinación de técnicas TEM y EELS de alta resolución podría proporcionar información detallada para que los investigadores entiendan los mecanismos de los

fotoelectrodos y obtengan una mejora en el rendimiento fotoelectroquímico. Además, para satisfacer las demandas de los seres humanos con un entorno amigable, se espera lograr dispositivos de división de agua escalables impulsados por el sol para la generación de H_2.

Appendix C: List of acronyms

ADP	Adenosine diphosphate
AES	Auger electron spectroscopy
AFM	Atomic force microscopy
AM	Air mass
ALD	Atomic layer deposition
AZO	Al-doped zinc oxide
BSE	Back-scattered electrons
BSF	Back surface field
CAFM	Conductive atomic force microscopy
CB	Conduction band
CO_2	Carbon dioxide
CV	Cyclic voltammetry
CVD	Chemical vapor deposition
EC	Electrochemical
EDX	Energy dispersive X-ray spectroscopy
EELS	Electron energy loss spectroscope
EQE	External quantum efficiency
FIB	Focused ion beam
fs	Femtosecond
H_2	Hydrogen
H_3BO_3	Boric acid
HAADF	High-angle annular dark-field imaging
HER	Hydrogen evolution reaction
HF	Hydrofluoric acid
IEA	International Energy Agency
IR	Infrared

IrO_2	Iridium oxide
ISTEP	Multi-current steps
I-t	Current–time
I-V	Current-voltage
KCl	Potassium chloride
KOH	Potassium hydroxide
LiOH	Lithium hydroxide
$LiOH \cdot H_2O$	Lithium hydroxide monohydrate
LSPR	Local surface plamon resonance
LSV	Linear sweep voltammetry
M/S	Metal/semiconductor
MIS	Metal-insulator-semiconductor
Nps	Nanoparticles
O_2	Oxygen
OER	Oxygen evolution reaction
PEC	Photoelectrochemical
PRET	Plasmon resonance energy transfer
P-t	Potential versus time
PTFE	Polytetrafluoroethylene
RBS	Rutherford Backscattering Spectrometry
RHE	Reversible hydrogen electrode
RMS	Root mean square
RuO_2	Ruthenium oxide
SAED	Selected area electron diffraction
SCE	Saturated calomel electrode
SE	Secondary electrons
SEI	Secondary electron imaging
SEM	Scanning electron microscopy
SiO_X	Silicon oxide

SOD	Superoxide dismutase
SPM	Scanning probe microscopy
STEM	Scanning transmission electron microscope
TCO	Transparent conductive oxide
TCS	Trichlorosilane
TEM	Transmission electron microscopy
TMDs	Transition metal dichalcogenides
UV	Ultraviolet
VB	Valence band
V_{ON}	Onset potential
V_{over}	Overpotential
V-t	Voltage-time
WHO	World Health Organization
XPS	X-ray photoelectron spectroscopy
X-TEM	Cross-sectional transmission electron microscopy